**Cometary Gas and Dust Delivered to Mars**

by

**Matteo M. J. Crismani**

B.A., University of California, Santa Cruz, 2012

A thesis submitted to the

Faculty of the Graduate School of the

University of Colorado in partial fulfillment

of the requirements for the degree of

Doctor of Philosophy

Department of Astrophysical and Planetary Science

2017

This thesis entitled:
Cometary Gas and Dust Delivered to Mars
written by Matteo M. J. Crismani
has been approved for the Department of Astrophysical and Planetary Science

Prof. Nicholas M. Schneider

Prof. Dave Brain

Dr. Ian Stewart

Prof. Fran Bagenal

Prof. Mihaly Horanyi

Date

The final copy of this thesis has been examined by the signatories, and we find that both the content and the form meet acceptable presentation standards of scholarly work in the above mentioned discipline.

Crismani, Matteo M. J. (Ph.D., Astrophysical and Planetary Science)

Cometary Gas and Dust Delivered to Mars

Thesis directed by Prof. Nicholas M. Schneider

This thesis investigates the interaction of cometary atmospheres (coma) and debris streams (meteor showers) on Mars' atmosphere. In this work, we use the close encounter of Comet Siding Spring (C/2013 A1) with Mars to investigate delivered cometary gas and dust. This serendipitous encounter occurred at a distance of 141,000 km, three times closer than distance between Earth and the Moon and was observed by the Imaging Ultraviolet Spectrograph (IUVS) on the Mars Atmosphere and Volatile EvolutioN (MAVEN) Mission. The gaseous coma enveloped the planet and Mars passed through the comet's fresh debris stream, bombarding the upper atmosphere with cometary dust particles. Dust particles are liberated from comets as gas sublimates from their surfaces, and these particles evolve according to their size to form the interplanetary dust environment. As these interplanetary dust particles sporadically enter the Martian atmosphere, they ablate and form a layer of meteoric ions, and we detail this discovery and its implications.

## Dedication

To my dogs, family and friends.

## Acknowledgements

This work represents a culmination of years of learning and support. I have been extremely fortuitous to be surrounded by mentors and role models who have shaped my philosophical outlook and great friends who helped me to maintain my sanity.

First, I must thank Nick Schneider for the opportunity to work with him on these projects, and managing an instrument whose capabilities exceeded expectations. His years of valuable advice has shaped me as a scientist, and he is my role model for a scientific leader. I must thank Michael Nauenberg, who saw a budding scientist in me, even when I did not, and was my guide and mentor in the beginning of this career. I would like to thank James "BJ" Bjorken, for demonstrating the significance of doing interesting problems, and maintaining modesty throughout your successes.

My gratitude for my mother knows no bounds, for always supporting me in this endeavor even when she did not understand why I was undertaking it. I must thank my father, for demonstrating that persistence in your passion is always worth your time. To my Oma, for uncountable conversations that encouraged outside interests (not just "shop talk") that helped make me well rounded. And to my grandmother Holly, who was the first to pique my curiosity of the world, with trips to the zoo, museum, and on two wheels of the Taurus.

There is not enough room on this page to thank my friends, but without them this work would not be possible. This endeavor does not exist in a vacuum, and love and support of my friends has carried me the trying times of my life. I consider myself among the most fortunate to have such a kind, honest, caring, and funny group of people to call my framily.

# Contents

**Chapter**

# Tables

**Table**

# Figures

**Figure**

# Chapter 1

# Introduction

## 1.1 Overview

Scientific events described by the press as "once in human history" are rarely as fantastic as promoted, but on October 19th, 2014, a comet made a close encounter with Mars, apparently creating the largest meteor shower in modern times. Through good fortune and hard work, the science community was prepared to study this fleeting event, and the coordinated observing campaign of several Mars orbiters and Earth observatories was a success. Discovered in Australia at the Siding Spring observatory, where C/2013 A1 (Siding Spring) (McNaught et al., 2013) gets its name, interest was immediately generated in this comet as the initial orbital solutions suggested a possible impact with Mars. While this prediction was soon revised with better observations of its orbital ephemeris, comet Siding Spring still captured the scientific community's attention as the orbital solution demonstrated that this comet would miss Mars by only 141,000 km, or a third of the distance between Earth and the Moon. For Mars, the frequency of an encounter this close is between 100,000 and 1,000,00 years (Stokes et al., 2003), and may represent the only such encounter in human history.

## 1.2 Comets

A comet is a small icy body defined by its orbit, whose eccentricity create a large hydrogen coma, dust and plasma tails during perihelion passages near the inner solar system. We distinguish classes of comets by their orbital characteristics and this allows us to infer

gross properties of their formation. There are three primary families of comets, the Oort Cloud Comets, the Jupiter Family Comets, and the Halley-Type Comets. Jupiter Family and Halley-Type comets are both classes of short period comets, where the former has low inclination and the latter has high inclinations, indicating a different origin for these objects.

Oort cloud comets are usually very bright in the night sky (e.g. comet Hale-Bopp) as they have made very few passages into the inner solar system, and their volatile content has not been significantly depleted. The Oort cloud is the spherical distribution of small bodies that orbit the Sun well beyond the orbit of Pluto, with aphelia between 5,000 and 100,000 astronomical units (Levison and Dones, 2014). Their orbital properties are isotropic; they have no preferred angle of orbital inclination and are likely formed with the solar system as a whole. Discovered in 1950 by Jan Hendrik Oort, he noted a few comets with these properties and made the "reasonable" assumption that such a cloud must contain billions of these objects (Oort et al., 1950). Modern observations cannot verify this supposition in its entirety, however it is generally accepted that Oort's value of billions is correct (Weissman, 1983). These objects are fairly small individually, and the total contribution of the Oort cloud is thought to be on the order of five Earth masses (Morbidelli, 2006). When these objects become perturbed by a passing star or giant molecular cloud, they enter the inner solar system on highly elliptical, and usually highly inclined, orbits. If an object is traveling to the inner solar system for the first time, it is defined as a "dynamically new" comet.

Jupiter Family comets are thought to be remnants of Kuiper Belt Objects that were perturbed by Neptune and subsequently Jupiter to alter their perihelion such that their orbits visit the inner solar system (Levison and Duncan, 1994). Jupiter Family comets mostly orbit in the same direction as the planets, have periods shorter than 20 years, and have inclinations less than 30 degrees from the ecliptic. A majority of these objects are very faint, as multiple trips to the inner solar system create a rapid depletion of their volatile content, and those that are depleted of volatiles entirely are considered "dead" (e.g. the Damocloids).

Halley Type comets have high inclinations, indicating that they are perturbed Oort cloud comets which have become trapped into short period orbits by interactions with the gas giants (Sagan and Druyan, 1997). There are subclasses within some of these groups, such as the sun-grazing comets, whose perihelions are less than the orbit of Mercury and whose lifetimes are notably shorter because of this (e.g. comet ISON).

### 1.2.1 Cometary Nuclei

Comets are small objects, usually less than 20 km in diameter, with a great variety of shapes (cigar-shaped, peanut-shaped, etc.), as they are not sufficiently large to become spherical due to self-gravity. The atmosphere of a comet is called its coma, which is primarily comprised of hydrogen due to the dissociation of liberated water ice from the surface of the nuclei. The currently accepted model for the cometary nucleus suggests that comets are dirty snowballs comprised of ice, dust, and rock (Whipple, 1950). Several space missions (Deep Impact, Rosetta, etc.) have since confirmed this, noting they are primarily comprised of water ice (75%), dust and rock (25%), and that the nuclei of these comets are very dark, with albedos of only a few percent.

Compared to freshly fallen snow (90%), or dirty snow (20%), the albedo of comets ($\sim$ 4%) suggest evolutionary information about these objects. Two proposed mechanisms are cosmic ray weathering (Johnson et al., 1988) and formation of surface mantle from large rocks (Panale and Salvail, 1984). High energy cosmic rays, coming from outside of the solar system, may irradiate the surface of these objects to form a layer of dark complex carbon compounds called an irradiation mantle. Such a layer would take millions of years to form, which may be possible for Oort cloud comets who spend a majority of their lives in the outer reaches of the solar system. The second mechanism suggests the sublimation of ice leaves behind large rocks, which cannot be carried by the escaping gas, and these rocks form a shell around the outside of the comet.

Comets are not usually spherical, and the diversity in their shapes indicates these

objects do not exist quiescently for the age of the solar system. The compositional nature of the nucleus is not necessarily known; although recent evidence suggests that comets are likely conglomerate objects. The break up of comet Shoemaker-Levy before its impact with Jupiter (Figure 1.1) and bilobate nucleus of CG 67P observed by the Rosetta mission both suggest that comets have conglomerate nuclei. Therefore, this material should be well shielded from solar insolation, and gas from the near surface should serve as a reliable indication of the formation conditions of the early solar system.

Interest in comets comes primarily from their role in illuminating the important processes in solar system formation and evolution. Comets are expected to be some of the most primitive objects in the solar system, and their composition may be the best representation of solar nebula. While they likely formed far from the Sun, the ices contained therein are particularly sensitive to the physical and thermochemical conditions of their formation region (Bockelée-Morvan et al., 2004). Because comets are such good proxies for the early conditions of the solar system, determining their chemical composition is of great scientific importance, and therefore determining the volatile content of comets is a primary goal for cometary astronomy. The extent to which cometary volatiles inherited their compositions from the young disk as opposed to subsequent processing during its time in the solar nebula is still being understood (Bockelée-Morvan et al., 2004; Irvine et al., 2000; Lunine and Gautier, 2004). While processing may occur on their surfaces, the majority of cometary nuclei are considered to be pristine, with the understanding that longer period comets are likely more pristine than those that have had many passages by the Sun.

### 1.2.2 Cometary Gas

Sublimation is the primary process by which comets convert solid ice on their surfaces into the gases we observe in their coma. A coma is the gravitationally unbound atmosphere of the comet, created by sublimation of surface and sub-surface volatiles. As illustrated in the phase diagram for water (Figure 1.2), water ice is directly converted to gas at 170K in

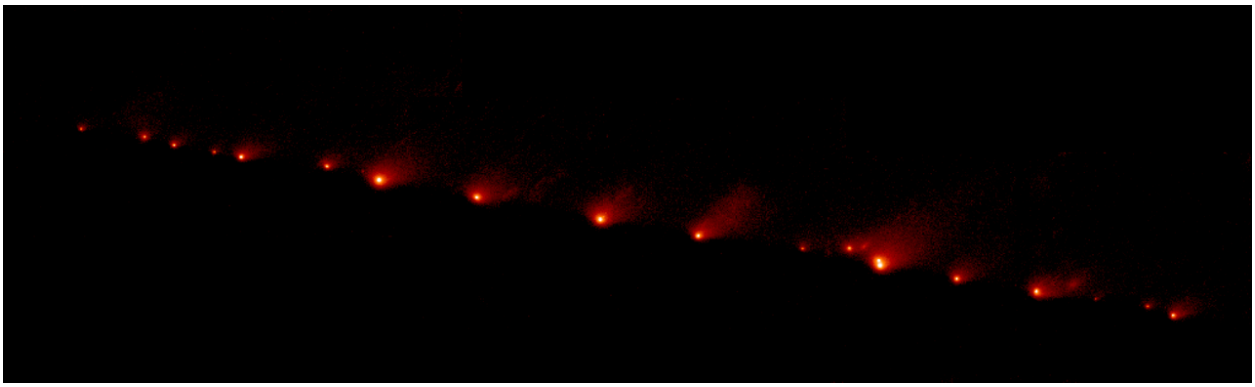

Figure 1.1: A NASA Hubble Space Telescope (HST) image of comet Shoemaker-Levy 9, taken on May 17, 1994. When the comet was observed, its train of 21 icy fragments stretched across 1.1 million km of space, or 3 times the distance between Earth and the Moon. Image Credit: NASA/ESA

the vacuum of space. Various molecules have their own phase diagrams, and the sublimation of $CO_2$ and $H_2O$ occur at different temperatures, where even at Earth's surface pressure and temperature, $CO_2$ never becomes a liquid and is instead referred to colloquially as dry ice.

Radiation from the Sun expands spherically, with its intensity decreasing as the square of the distance from the solar surface. Therefore, this intensity decrease defines the temperature profile in the vacuum of the solar system. Water ice begins to sublimate inside of the orbit of Jupiter where temperatures from solar irradiation become close to 170K (3 AU) (Kelley et al., 2013). $CO_2$ begins to sublimate at a distances consistent with insolation equivalent to 80K, and comets are said to "turn on" $CO_2$ production as they enter the inner solar system from the outside (12 AU). $CO_2$ and CO make up less than 20% of the comet's observed sublimation, therefore the activity of the comet is most strongly driven by water.

As the surface of a comet heats up, water ice is converted to gas; this process is defined as the activity, or water production rate, of the comet. Rotation of the comet causes different regions to become shaded and unshaded; Sun-facing regions become more active, sometimes resulting in the formation of jets (Figure 1.3). As cometary gas jets turn on, the water production rate is increased and when cometary dust is dragged along with this gas, the dust coma may brighten. A majority of the gaseous production is due only to the unshaded region, and the gaseous coma near the nucleus can be quite asymmetric. When this gas expands freely in space, these asymmetries diffuse leading to spherical symmetry at large distances.

Water ice is primarily liberated from the comet's surface, so the atmosphere of the comet is built up of water and its dissociation products. Water exposed to ionizing radiation from the Sun is broken up into OH, O, and H, all of which can become ionized and dragged along with the solar wind. Considering the comet's small mass, it is incapable of retaining hydrogen, allowing the coma to grow as large as large as 1 AU (comet Hale-Bopp) (Burnham, 2000). There are two main gaseous components to a comet, its neutral atmosphere, which is roughly spherical, and its ionized tail, which points away from the Sun, modulated by

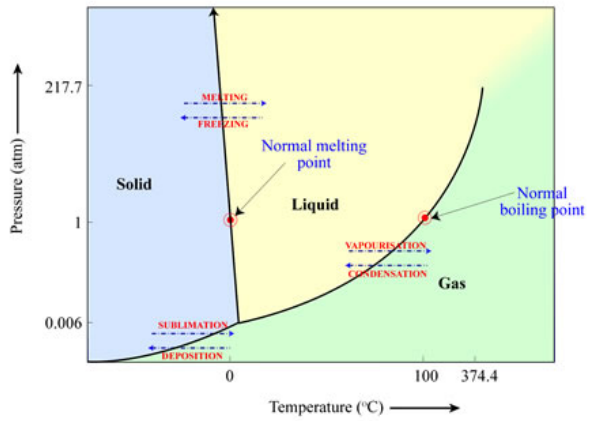


(a) Phase diagram for $H_2O$

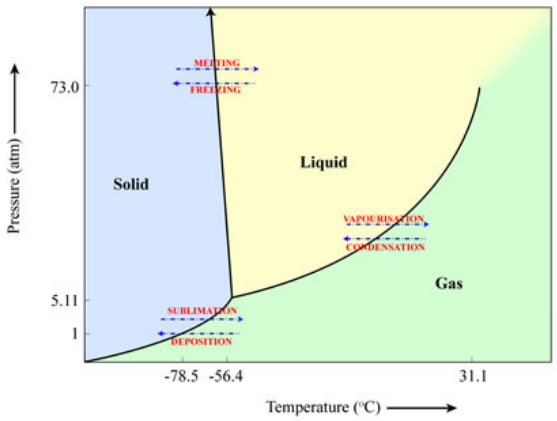


(b) Phase diagram for $CO_2$

Figure 1.2: **(Left)** Low pressures found in the vacuum of space indicate that water sublimates rather than melts. **(Right)** At the pressure of sea level on Earth, at room temperature, $CO_2$ will turn directly from a solid to a gas. Image Credit: Swinburne University of Technology

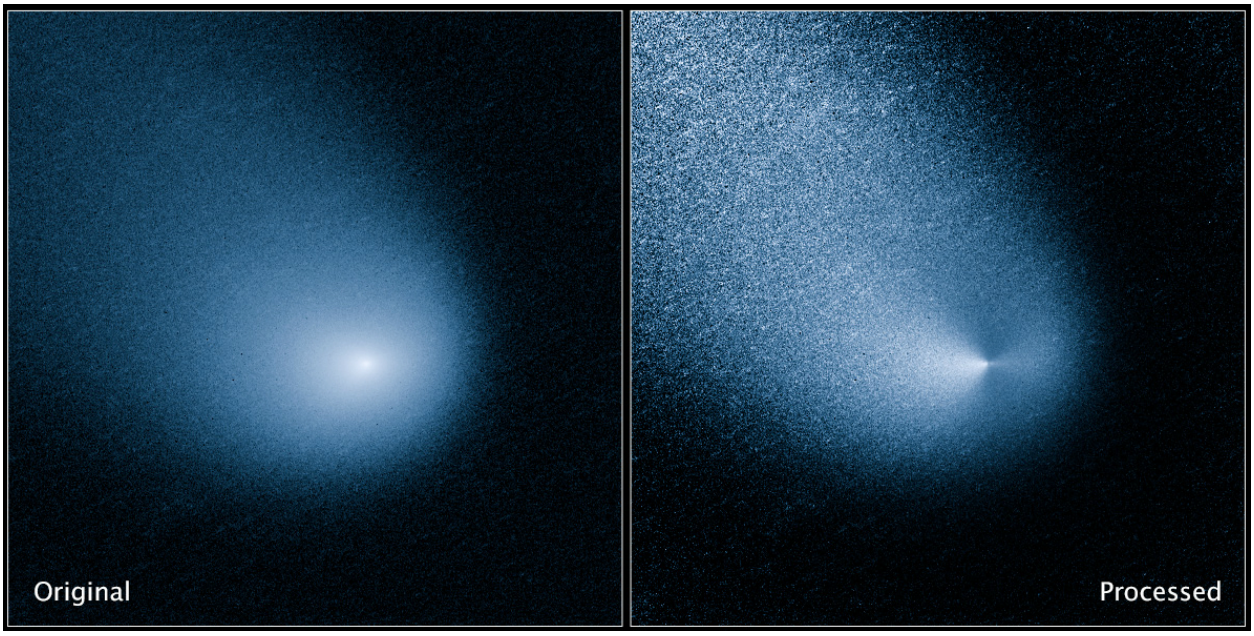


Figure 1.3: **(Left)** Captured March 11, 2014 by NASA's Hubble Space Telescope, comet Siding Spring is shown at a distance of 353 million miles from Earth. The nucleus is surrounded by a coma that measures roughly 12,000 miles across. **(Right)** The comet after image processing techniques were applied to remove the hazy glow of the coma revealing what appear to be two jets of dust coming off the location of the nucleus in opposite directions. Image Credit: NASA-GSFC

the direction of the solar wind. To a first order approximation, the neutral atmosphere of a comet is well described by the free expansion model of Eddington (1910).

### 1.2.3 Cometary Dust

Comets seen in the night sky are visible only when their surfaces heat up enough to release dust, which is an efficient scatterer of sunlight. Small solid dust grains are carried along by sublimating gas and form a dust coma, similar to the gaseous coma but with scales and densities that are quite different. Dust in space is subject to two forces, gravity and radiation pressure. Radiation pressure is a minute force that arises when a photon, which has momentum, is absorbed by an object and momentum conservation affects the object's trajectory. Radiation pressure becomes important for particles over long time periods or for those with large surface area to volume ratios, since the inertia of such an object is small comparatively.

The third major component to a comet, and arguably its most recognizable feature, is its dust tail. Cometary dust grains initially follow the trajectory of their parent body, but these orbits are modulated by radiation pressure which acts to sort particles by their size. Radiation pressure is ineffective on very large particles, and these trail behind the comet in a debris stream, or dust tail, whereas small particles are swept away and fill the solar system with dust (Figure 1.6). These small particles form the interplanetary dust environment and identifying their parent body rapidly becomes impossible. The larger particles lag behind the parent body and eventually form a torus of cometary debris, which is observed as a meteor shower each time a planet passes through it.

### 1.2.4 Comet Siding Spring

Comet Siding Spring (C/2013 A1) is a dynamically new Oort cloud comet that was discovered at 7.2 AU, with prediscovery observations out to distances of 10 AU. Siding Spring is on a retrograde inclined orbit, and has taken millions of years to move from the

Oort cloud toward the inner solar system. It is on a hyperbolic orbit and gets the description 'dynamically new', as it has not made any passages through the inner solar system, nor will it ever return. Since dynamically new comets have never been processed by the Sun, they preserve important information about the presolar nebula conditions. Typically the study of such objects is very difficult, due in part to their small number as well as their short observational opportunities.

The cratered face of the Moon is a constant reminder of the hazard of impacts from space. Because asteroid impacts are ten times more common than comets (Stokes et al., 2003), they lead the conversation about threats from near earth objects (NEOs). Unlike asteroids, comets have gaseous extended coma and long dust tails that interact with planets during close approaches or passes through one another's orbital paths. Most casual observers of the night sky are familiar with meteor showers as Earth passing through a comet's tail, where the comet likely passed the Earth years ago and by tens of millions of kilometers. Unfamiliar to any living person are the effects of close encounter with Earth, comparable to comet Siding Spring's with Mars, where the distance between them was so small that the planet became engulfed in the comet's gaseous coma and immediately passed through the comet's fresh debris stream.

On Earth, impacts with Siding Spring-size comets occur every $10^8$ years (Stokes et al., 2003). Close approaches are more likely, which may play a role in depositing water and other volatiles in the atmospheres of terrestrial planets or affecting planetary climate with meteoric clouds. The most recent close approach to Earth was comet D/1770 L1 (Lexell), which missed Earth by 365 Earth radii (2.3 x $10^6$ km). Based on information from impact cratering, it is estimated that a close approach of kilometer-sized comets within 25 Earth radii occurs once every $10^5$ years, and scaling to Mars, this is the same frequency with which comets come within 50 Mars radii (100,000 km) (Ye and Hui, 2014).

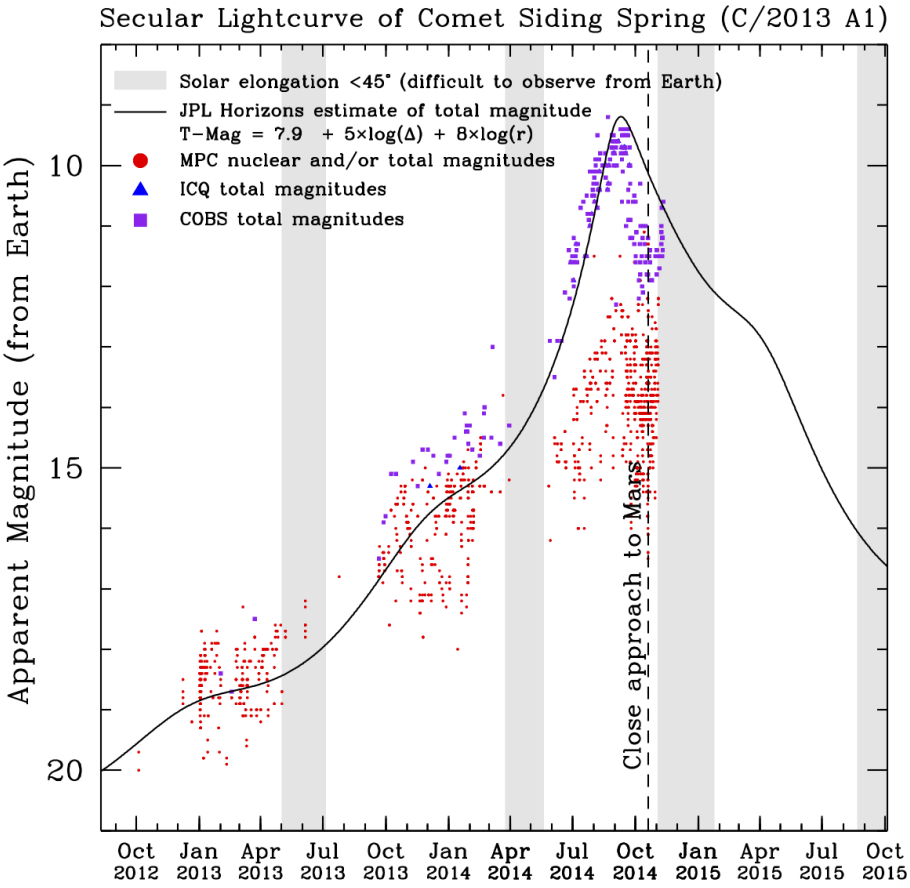


Figure 1.4: The lightcurve of comet Siding Spring prior to the encounter with Mars. This work represents the aggregate of professional (purple and blue) and amateur observers (red) with various observatories, where differences in image processing techniques is the main source of scatter in the data. The systematic difference between amateurs and professional reflects the difficulty in proper airmass subtraction associated with the comet going through perihelion. Image Credit: M. Knight

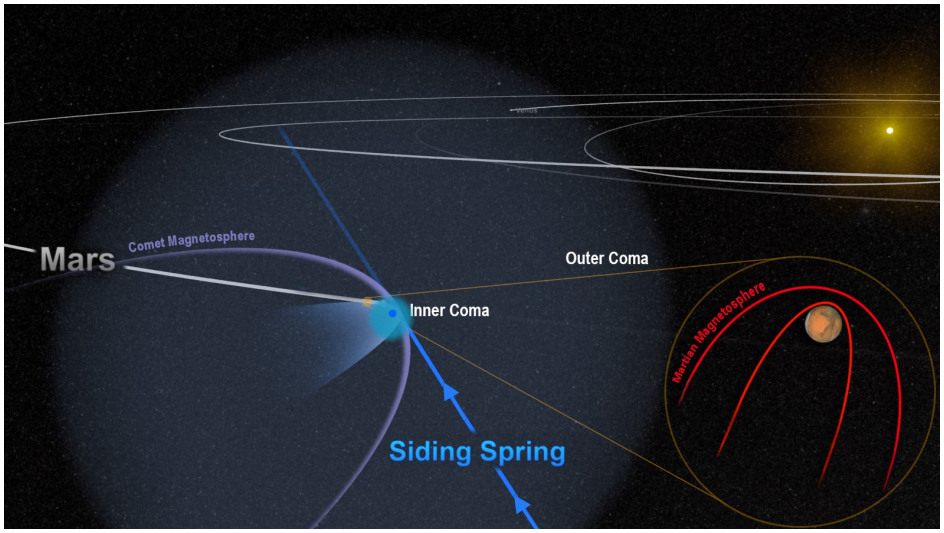


Figure 1.5: Siding Spring's Orbital Geometry. Image Credit: NASA

## 1.3 Meteors

Shootings stars are neither shooting or stars, but small dust grains entering the atmosphere at orbital velocities, and are technically called meteors. Although meteors have been observed since ancient times, they were perceived in the West as an atmospheric phenomenon, similar to lightning. In 1807, Benjamin Silliman was the first to argue that a meteorite fall in Weston, Connecticut was associated with a cosmic origin (Silliman and Kingsley, 1869). In November 1833, a spectacular meteor storm occurred where observers across the eastern United States observed thousands of meteors seeming to originate from a single point in the sky, the constellation Leo (Asher, 1999) (Figure 1.7).

Most meteors appear sporadically, without a preferred origin in the sky, as the distribution of interplanetary dust particles is roughly isotropic. Meteor showers are the exception, where dust particles can be traced to their parent body as originating from a common location on the sky, called the radiant. For example, the Leonids originate near the constellation Leo every year between November 15 through 20, when the Earth passes through the Halley-type comet 55P/Tempel-Tuttle's debris stream. The Leonids are known for generating bright meteors due to their high relative velocity relative to the Earth, 72 km/s, which increases the fraction of dust particles that are ionized. It was this meteor shower that was observed in 1833, and then predicted again for 1866, which firmly established the exogenous origin of meteor showers. However, they retain their historical atmospheric nomenclature, as their name "meteor" comes from the Greek word "$\mu\epsilon\tau\epsilon\omega\rho o\zeta$" which means "raised from the ground".

Visible meteors occur when dust grains, between the size of a sand grain and pea, enter the atmosphere at speeds of 10-70 km/s, compressing the air in front of them, which heats to more than 2000 K. The outer layers of the grain begin to vaporize, in a process called ablation, releasing atoms from the minerals found inside the grains. The heating of the atmosphere also ionizes the ambient gases, creating an ionization trail which can last up

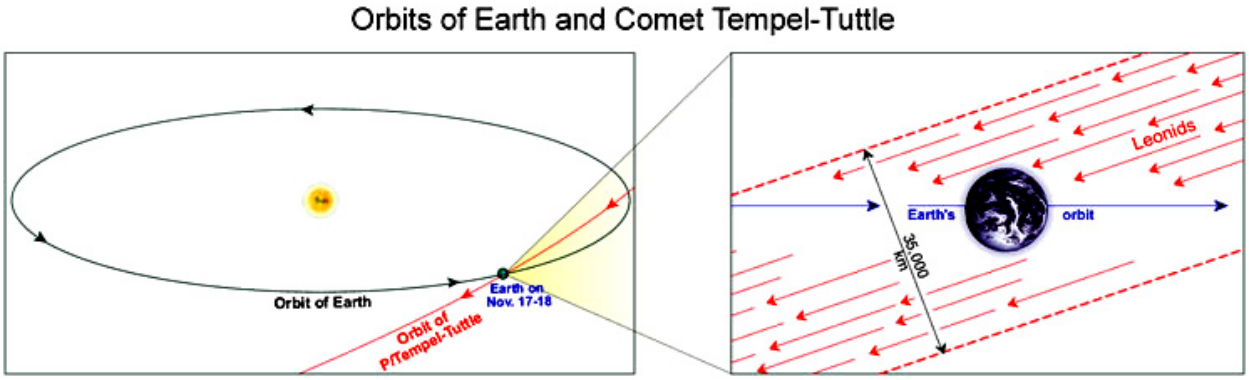


Figure 1.6: The orbit of Earth and comet 55P/Tempel-Tuttle, demonstrating the annual meteor shower of the Leonids. The retrograde motion of comet 55P/Tempet-Tuttle is shown with its correct orbital geometry; the Earth is not to scale in the left panel of this image. Image Credit: Swinburne University of Technology

to 45 minutes and which are found in the terrestrial upper atmosphere almost continuously. Light is emitted from both the ionized air and meteoroid, where the color of the latter is determined by the relative metallic content of grains (e.g. orange-yellow meteors contain sodium, whereas blue-green meteors contain magnesium) (Figure 1.7).

Metallic species are deposited in the upper atmosphere and may subsequently become ionized by charge exchange with ambient ions. Due to complex interactions with the Earth's dipole magnetic field, these metallic ions can become concentrated into strong ionization layers, which may last for up to minutes or hours. There are defined layers in the Earth's ionosphere, associated with their production mechanism (e.g. E-layer form by x-ray and FUV radiation near 100 km). Since the sporadic meteor layers appear in the E-layer of the Earth's ionosphere, they are called sporadic E-layers, despite having a different source than the E-layer itself.

Wispy cloud structures may occur directly after a meteor; these are due to the polymerization of meteoric metallic species, called meteoric smoke particles. Such particles may last for hours or days, and may have had a role on the early climate of planets where sporadic ablation was more frequent due to the increased presence of interplanetary dust. These smoke particles are the nucleation sites for noctilucent clouds, which form at very high altitudes and are seen only at twilight when illuminated from below while lower layers of the atmosphere are in shadow.

## 1.4 The Martian Ionosphere

Mars' surface shows evidence that there was at one point abundant flowing water on the surface, as evidenced by the presence of deltas (Salese et al., 2016), marble-like hematite concretions likely formed as groundwater flows through permeable rock (Grotzinger et al., 2005), and even recent evidence for ancient tsunami that shaped the Martian coastlines (Rodriguez et al., 2016), although this latter point does not yet have community consensus. However, present Mars does not evoke imagery of oceans and lakes, and instead the thin

Figure 1.7: **(Left)** The Leonid meteor shower of 1833, which lasted as long as nine hours and was visible across the continental United States. **(Right)** A meteor from the Leonid meteor shower. This photograph shows the meteor, whose color is due to both meteor composition and atmospheric ionization, as well as the atmospheric wake. Image Credit: Navicore Meteor Photos

atmosphere and desiccated planet begs the question, “Where did the water go?” This is the driving science goal for the Mars Atmosphere and Volatile EvolutioN (MAVEN) mission (Jakosky et al., 2015b) whose aim is to determine the importance of atmospheric escape to the climate history of Mars.

The Martian ionosphere is a layer composed of ions and electrons that exists in the upper atmosphere at 120 km and above, which couples the neutral atmosphere to the exosphere. The ionosphere is created by photoionization of ambient atmospheric species on the dayside, and a combination of day night transport and electron precipitation on the nightside. The ionosphere is important to understanding the Martian environment, as it couples the neutral atmosphere to effects of charged particles in the solar wind, and may be a source for significant loss of the atmosphere. The Martian ionosphere has peaks at two main layers, at 120 km and 140 km, due to soft X-rays and Extreme Ultraviolet (EUV), respectively (Figure 1.8).

### 1.4.1 Pre-MAVEN Observations

The composition and dynamics of the Mars ionosphere has been studied in two eras, pre-MAVEN and post-MAVEN observations. The first observations of Mars' ionosphere come from the Mariner 9, Mars 4/5 and Viking 1/2 missions, where they obtained electron density and total electron content measurements. After these, the Mars Reconnaissance Orbiter (MRO) (Graf et al., 2005) and Mars Express (MEx) (Chicarro et al., 2004) missions continued this legacy of radio occultations. These spacecraft determined the vertical structure of the ionosphere, and atmospheric probes determined that atomic oxygen ions ($O^+$) are most common at high altitudes, whereas molecular oxygen ions ($O_2^+$) dominate near the main layers.

MRO and MEx also determined significant variability in the ionosphere, associated with large variations in the solar wind, atmospheric dynamics and composition, and the influence of crustal magnetic fields. They were able to observe the compression of the

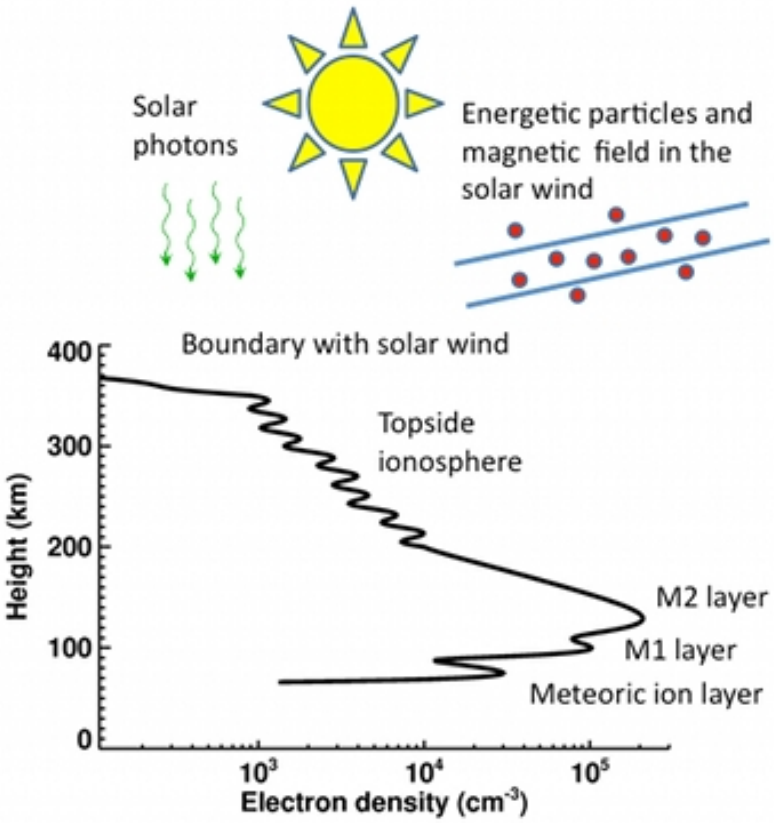


Figure 1.8: A schematic of the Martian ionosphere as understood before the MAVEN mission. Image Credit: P. Withers

dayside ionosphere, where the topside could be pushed by the solar wind down to altitudes of 250 km, or in quiescent periods extend as high as 650 km (Withers et al., 2012). The topside ionosphere was shown to be variable, with some profiles exhibiting smooth vertical extent, and some profiles showing wavelike behavior (Withers et al., 2016).

The nightside lacks sunlight necessary to ionize the atmosphere, and in the absence of any other production source, the ionosphere should disappear within minutes of becoming shaded. This is not observed, and remains an outstanding issue in Martian ionospheric science (Fowler et al., 2015). Two suggested significant processes are day-night transport and electron precipitation, the former describes ions swept from the dayside to the nightside by horizontal neutral winds and the latter describes electrons that travel down open field lines and crash into the atmosphere. Because these processes are not uniform in their effects, the nightside ionosphere can be patchy and inconsistent spatially and temporally.

### 1.4.2 Modern Observations

In an attempt to determine the effect of the ionosphere on the loss of Mars' atmosphere and its effect on habitability, the MAVEN spacecraft is equipped with a particle and fields instrument suite. The primary in situ instruments for ionospheric observations are the Neutral Gas and Ion Mass Spectrometer (NGIMS) (Mahaffy et al., 2015) and the Langmuir Probe and Waves (LPW) (Andersson et al., 2015a), which detect ions and electrons, respectively.

The primary ion in Mars' dayside ionosphere is $O_2^+$ (Figure 1.9), which is the product of a number of reactions, leading to its dominance in the main ionosphere (Figure 1.10). Neutrals, such as $N_2$, $CO_2$, O, and $O_2$, become photoionized, and in the case of $CO_2$, may become photo-dissociated to $O^+$. These ions then undergo ion-neutral reactions, such as $N_2^+$ with $O_2$, $CO_2^+$ with $O_2$, $O^+$ with $CO_2$, to all produce $O_2^+$. Moreover, $N_2^+$ may charge exchange with $CO_2$, then that new ion with O, and then that new ion with $O_2$ to also produce $O_2^+$. Electron dissociative recombination destroys $O_2^+$ and creates O+O, a process that is sensitive to the electron density and temperature. At low altitudes, $O_2^+$ lifetime to recombination is

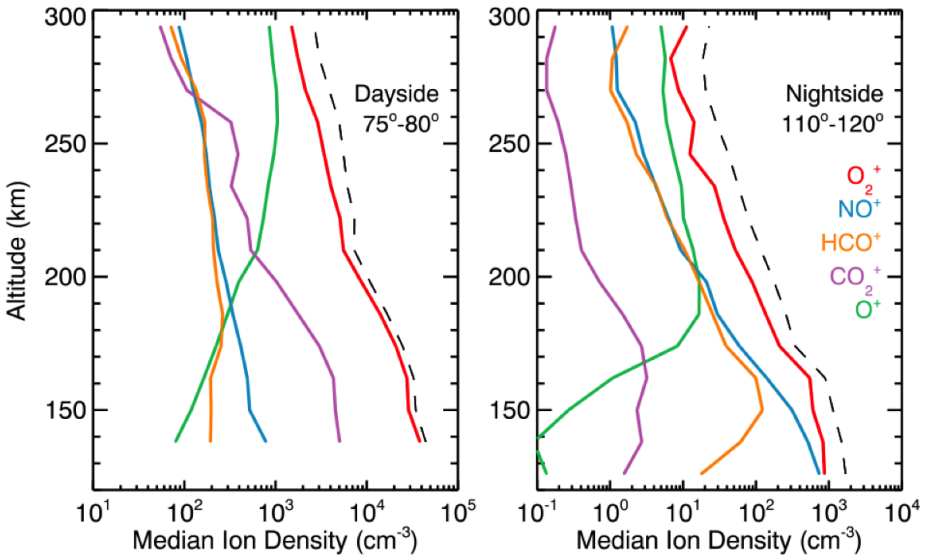


Figure 1.9: Mean observations of the Martian ionosphere from NGIMS. From: Girazian et al. (2017) **(Left)** Dayside median density profiles from near the dusk terminator at SZAs between 75 and 80. The different colors correspond to different ion species, and the dashed line is the total ion density. **(Right)** Same as left but showing nightside median density profiles from dusk SZAs between 110 and 120.

long enough that it can create $NO^+$, which is the dominant ion at low altitudes.

## 1.5 The Imaging UltraViolet Spectrograph

MAVEN's remote sensing instrument for studying Mars' upper atmosphere is the Imaging Ultraviolet Spectrograph (IUVS) (McClintock et al., 2015). This instrument observes in the far and middle UV (110-190 nm and 190-340 nm) in separate channels, and measures atmospheric emissions from $CO_2$, its dissociation and ionization products as well as atomic and molecular species such as O and $N_2$. The instrument uses a scan mirror to construct vertical profiles of emergent radiation from the atmosphere at the limb. We used IUVS to construct images of the hydrogen coma of comet C/2013 A1 (Siding Spring) days before its close encounter with Mars. We also used observations of the atmosphere from the periapse segment of each orbit, where IUVS produces limb scans over the altitude range 90-250 km. Each orbit, IUVS takes up to 12 limb scans in a 22 minute observation period spanning 45 degrees around the planet. MAVEN's elliptical orbit precesses about Mars on timescales of months to provide complete coverage of the planet. Data processing techniques are outlined in detail in previous MAVEN/IUVS papers (Crismani et al., 2015; Schneider et al., 2015b; Jain et al., 2015; Evans et al., 2015; Stevens et al., 2015; Crismani et al., 2017b) and all data used herein are available on the atmospheres node of the NASA Planetary Data System.

### 1.5.1 Instrument Characterization

For completeness and as a tool for those who use this data in the future, we will describe the important aspects of its capabilities and performance. During the cruise phase of the mission, we observed interplanetary hydrogen (IPH) and UV-bright stars to characterize the instrument performance, as well as determine our absolute calibration. The analysis of this work allowed us to create an uncertainty model for each pixel described in Section 1.5.3.

The instrument can construct images by scanning a mirror that moves the position of the slit on the sky within our fields of regard (FOR). There are two primary FOR (limb

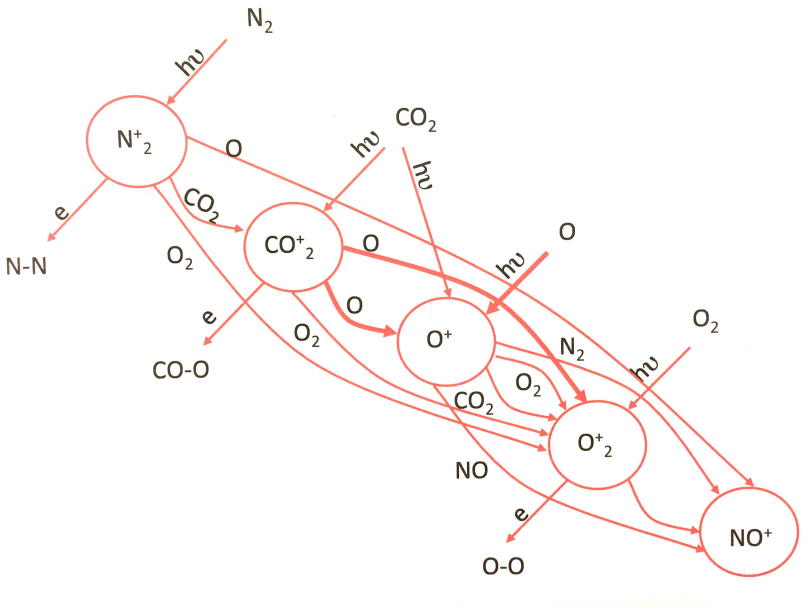


Figure 1.10: Ion chemical pathways at Mars, adapted from Barth et al. (1971b).

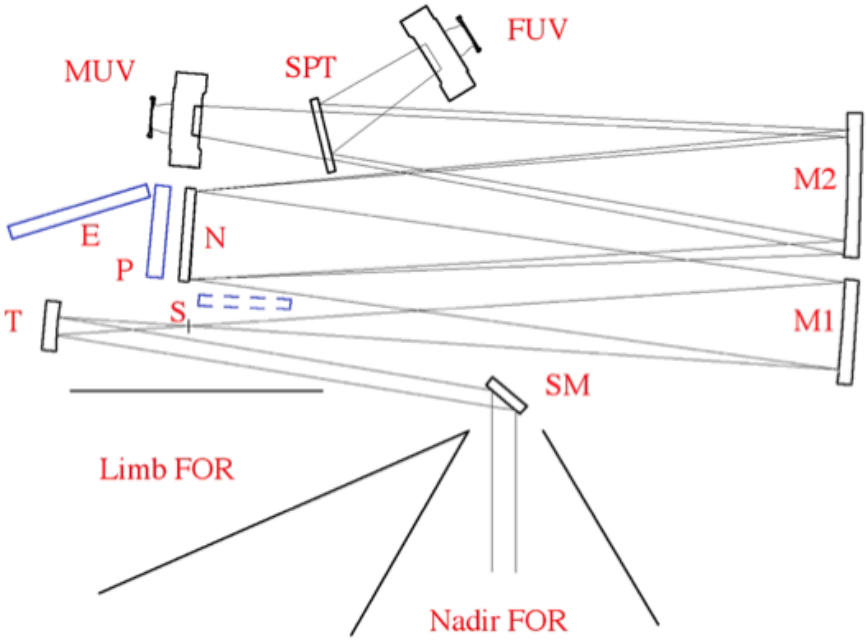


Figure 1.11: The IUVS nominal optical schematic. The relevant optical components are labeled with letters: SM—scan mirror, T—telescope mirror, S—spectrograph entrance slit, M1—spectrograph collimator mirror, N—normal incidence grating, M2—spectrograph camera mirror, SPT—beam splitter, MUV—MUV detector, and FUV—FUV detector. From (McClintock et al., 2015)

and nadir), contained by baffles, that allow IUVS to image large sections of the sky without moving the spacecraft. The slit is long and narrow, measuring 11 x 0.06 degrees, and the two FOR are 24 x 12 and 60 x 12 degrees, respectively. The data are taken in the form of two–dimensional images, with the horizontal axis corresponding to wavelength, and the vertical axis representing spatial position along the slit (Figure 1.12).

The detector is comprised of three main parts, the intensifier, the fiber optic taper and the complementary metal–oxide semiconductor (CMOS) detector. The intensifier uses a photocathode that converts UV photons into photoelectrons, which are then accelerated onto the microchannel plate where these electrons generate a burst of visible photons. The photons from the phosphor are coupled through fiber optics to the CMOS array. The CMOS detector uses 1024 amplifiers, for each row and column (1024 x 1024), to readout. Each pixel is then addressed by pixel in a row, one row at a time, such that there is no global reset for the detector.

The optical path for the observing modes used in this work are shown in Figure 1.11. Light enters either of the ports (limb or nadir) and is directed by the scan mirror (SM) to the telescope mirror (T). After hitting the collimating mirror (M1), the light is dispersed into two orders off of the normal incidence grating (N) (1st order: 180—340 nm and 2nd order: 110—190 nm). The spectrograph camera mirror (M2) then reimages the beam and then the beam is split by a fused silica, area-division beam splitter (SPT). The beam splitter transmits wavelengths greater than 180 nm and reflects first and second order light toward the FUV detector. While the MUV's image intensifier has a cesium telluride photocathode, the FUV's photocathode is cesium iodide, which is less sensitive to photons with wavelengths larger than 200nm. This allows the FUV to detect second order wavelengths and exclude most MUV radiation emitted by the atmosphere and reflected solar continuum.

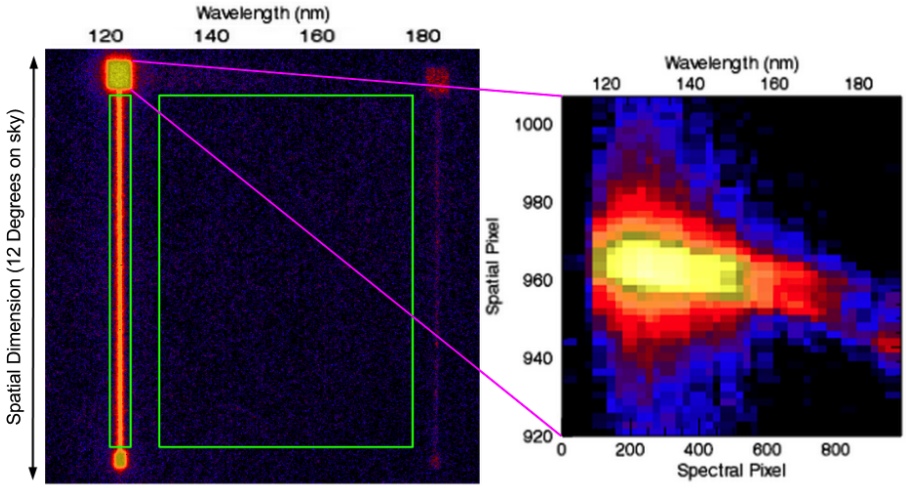


Figure 1.12: **(Left)** The FUV detector of the instrument, with second order Lyman-$\alpha$ on the left, and third order on the right. Since interplanetary hydrogen fills the slit, the image of the slit is projected on the detector, with the large keyhole at the top where the stellar observation was targeted. The thin green rectangle on the left indicates the region between the keyholes we use to analyze spectral emissions. The larger green rectangle is the region described in Figure 1.14. **(Right)** Stellar observation that determines the location of the star within the keyhole, which are distinct from the observations shown on the left. The star is spread by the instrument point spread function, and the tilt toward the right of the image is due to the fiber optic coupling. These observations are the high spatial resolution complement to those described in section 1.5.2.

### 1.5.2 Cruise Observations

To characterize the gain and noise in the instrument, we measured the instrument variance when subjected to an assumed temporally constant source. We constructed a measure of variance in stellar targets by repeated observations without changes to the observation parameters or instrument. We chose the SOLSTICE stars, Bet Cen, Alp Cru, and Bet CMa, as they are well characterized in the same wavelength region of the instrument. Throughout the majority of cruise we were able to observe IPH in order to understand the characteristics of the detector in space. These observations led to the characterization of some features in our data not seen in the lab, from cosmic ray hits, to "measles", discussed in section 1.14. Cosmic ray hits appear as large streaks on the detector, whose shape vary from circular to very elongated and have varying intensity.

In order to confirm that we were obtaining all of the light from the star, we placed the stars in the large keyhole, verifying the pointing accuracy requirements by inspection. Taking 28 subsequent images of short exposure time and low voltage, we were able to minimize the presence of cosmic ray hits, with the interpretation that the variance we observed was likely due only to the Poisson noise of our target. Given the gain inherent in the detector, the relation between signal and associated noise is modified as in McClintock et al. (2015):

$$\sigma = \sqrt{GN_{DNs}} \tag{1.1}$$

where $\sigma$ is the noise on a detector element, $G$ is the gain of the detector, $N_{DNs}$ is the intensity on that detector element given in digital numbers (DNs).

In sampling the spectral range of our observations, we are also sampling different levels of brightness, and from this, can construct a list of mean values at various brightnesses. After measuring their standard deviation from this mean, we plot the mean value at a brightness against its standard deviation, and note that there is good agreement with a square root fit as shown in Figure 1.13 and by Equation 1.1. This is valid under the assumption that the

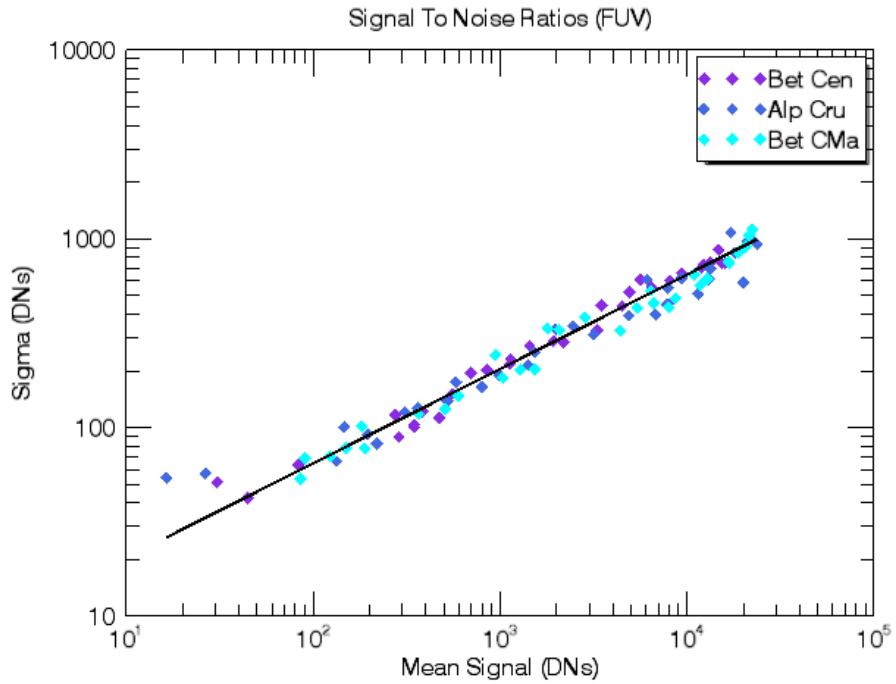


Figure 1.13: Mean signals from a given spectral index are compared with their observed standard deviation. The black line is the best fit from the Equation 1.1, where $G$ is fit by the method of least squares (Bevington and Robinson, 1969; Press, 2007).

variance of the detector is not a function of wavelength.

Immediately after analysis of the first data sets, a low–level detector background was noticed. This background looks like measles on the detector that are not constant spatially or temporally, and not attributable to individual hot pixels. They are a function of integration length, and longer images tend to have more of them than shorter ones. The instrument creates photon splashes from a single UV photon, and this is observed as correlated pixel intensity in bins smaller than eight pixels on a side.

Taking the difference of two subsequently collected dark frames, we can characterize the distribution of values that fall on the detector with the histogram found in Figure 1.14. We find the differenced dark has a mean consistent with zero DN. Unlike dark noise, data with measles have a mean above zero suggesting a low level of background light is encountering the detector. By characterizing the noise they contribute to a frame, we can account for this in our uncertainties model.

### 1.5.3 Data Statistical Uncertainties

From the cruise observations, we can construct a simple model for the uncertainties of the data. The data is already dark subtracted, and presented in units of DN, with calibration to physical units described later. There are two dominant sources of noise for this data then: Poisson noise associated with the source and background noise, a blanket term for the measles, and all the sources of noise prior to this level of processing (dark current, read noise, quantization noise, and intensifier excess noise, see McClintock et al. (2015)) These dominant sources of noise are added in quadrature, and the prescribed random uncertainty given to a pixel is described by:

$$\sigma = \sqrt{GN_{DNs} + \sigma^2_{background}} \tag{1.2}$$

where $\sigma_{background}$ is noise from measles, and with other variables defined as in Equation 1.1.

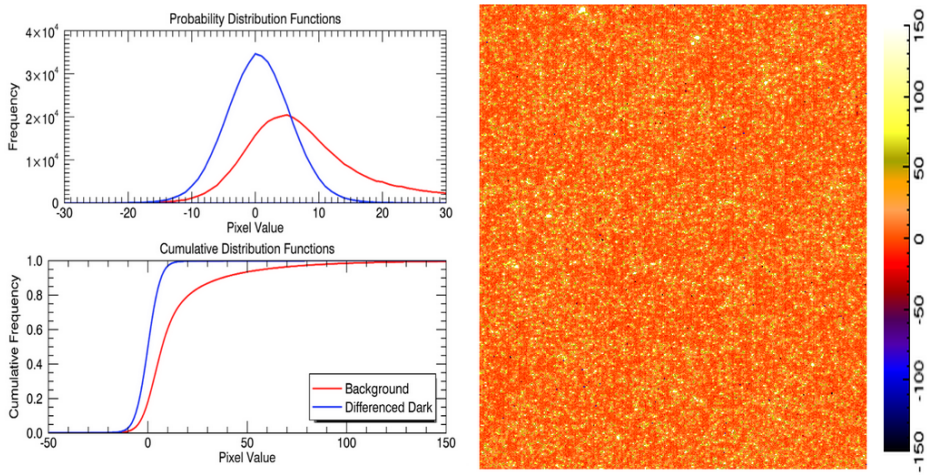


Figure 1.14: **(Left)** A comparison of the observed probability and cumulative distribution functions for the region described on the right. The red line is the measles, while the blue line is a differenced dark. Note the mean of the red line is greater than zero. **(Right)** This is the region in Figure 1.12 outlined by a large green rectangle, rescaled to demonstrate the relative lack of pixels whose values are negative or zero.

In practice, the instrument changes voltage, integration time, and the binning size of pixels so we developed a general framework to describe the uncertainty for a given data bin. We determined the gain from the data, and expect it to be solely a function of voltage, which is true to precision we require. The functional form of this relation is given by:

$$G(V) = \frac{f_0}{2^{\frac{V_0 - V}{50}}} \tag{1.3}$$

where $V$ is the voltage and $f$ is the constant derived from the data at a given voltage $V_0$.

The background noise was observed to be a function of voltage, integration time and bin size. The bin size approximation is invalid for high resolution binning, as the instrument has correlated errors between pixels due to photon "splashes" in the photo-intensifier. We describe the uncertainties generally with:

$$\sigma_{DNs}(V, t, n_{pixels}) = \sqrt{N_{DNs}\frac{f_0}{2^{\frac{V_0 - V}{50}}} + (\frac{\sigma_0}{2^{\frac{V_0 - V}{50}}}\sqrt{\frac{tn_{pixels}}{t_0 n_0}})^2} \tag{1.4}$$

where t is the integration time, n is the number of pixels, and the subscript 0 indicates the reference value from which we made and tested this model.

With the per pixel errors prescribed as above, we subsequently ask what the error over a spectral feature is by simple error propagation. Since we sum the signal spectrally, we add the uncertainties in quadrature with:

$$\sigma^2 = \Sigma_i \sigma_i^2 = G(\Sigma_i N_{DNs,i}) + N_i \sigma^2_{background}, \tag{1.5}$$

where i is the spectral bin index. This work was incorporated into the IUVS data processing pipeline and forms the basis of the random uncertainty calculation of the level1b processing step. Since the conversion from DNs to physical units is done with a calibration factor over the integration time, we can use a fractional uncertainty to convert the DN uncertainty into physical units.

### 1.5.4 Multiple Linear Regression

Spectral emissions from atomic and molecular species can be distinguished by the method of multiple linear regression (Stevens et al., 2011). Linear regression assumes that the relationship between the observation or data and spectral emitters may be considered to be linear. This requires a model of the spectral emitters, and that their line shapes do not change with intensity or time. As each emission can be modeled and compared to laboratory measurements, an observed spectrum may be described by:

$$I(\lambda) = c + \Sigma_i \alpha_i I_i(\lambda) \tag{1.6}$$

where $I$ is the intensity of the spectrum at a given wavelength $\lambda$, which is comprised by $c$, a constant offset due to the instrument, and the linear combination of the product of intensities of relevant species (denoted by $i$) and their relative contribution ($\alpha_i$).

We use the IDL "regress.pro" routine to determine these intensities, with spectral templates drawn from a library of emissions appropriate to the Martian atmosphere. These templates include $CO_2$, CO, $N_2$, O, Mg, Fe, and their appropriate ions, multiplet, or band systems (Figure 1.15). Other than the solar template, the spectral retrieval templates are created from a model spectrum for each species using their respective line positions and atomic constants for resonant scattering, which is then convolved with the line spread function of the instrument. In both channels, the line spread function has a width of close to four pixels, which can be observed in our finest resolution binning (1024 x 1024). Uncertainties from the detector are propagated through this routine, and are co-added in the standard way when binning emissions by altitude. We have verified that this propagation is commutative by comparing the signal to noise of bright and faint emissions, binned in altitude before and after using multiple linear regression. The commutation property of this error propagation suggests that the uncertainties determined by the multiple linear regression technique are uncorrelated.

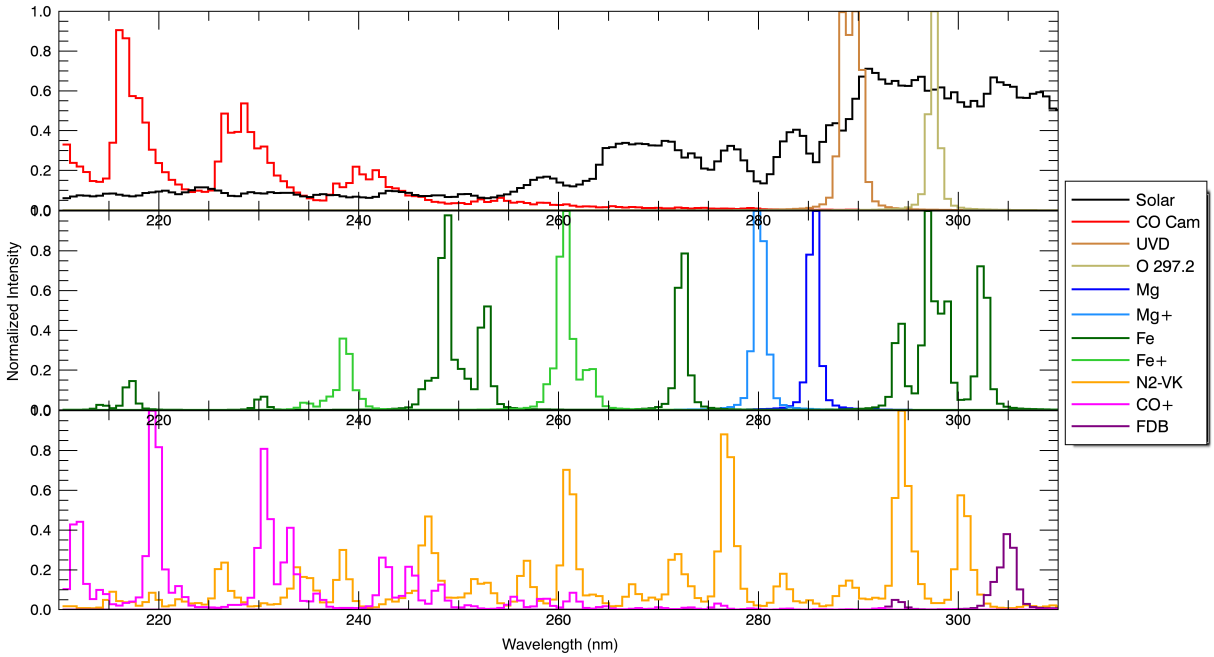


Figure 1.15: Model templates of all identified atmospheric and metallic emissions considered by this work. This figure is separated into three panels for clarity.

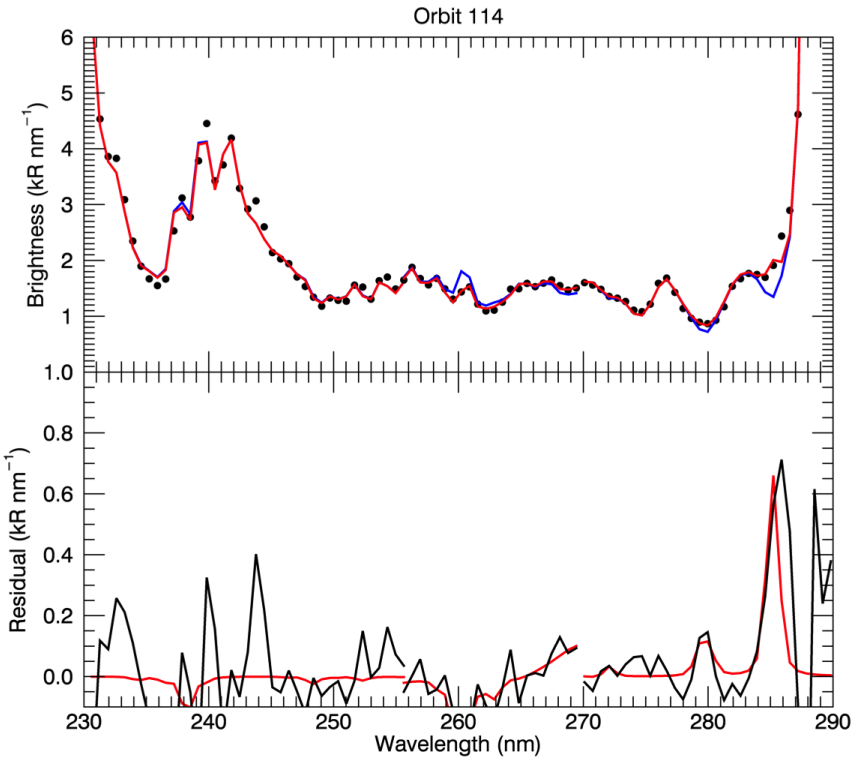


Figure 1.16: **(Top)** IUVS data (black dots) is compared to a composite fit of typical airglow emissions in the absence of metal emissions (blue), and in their presence (red). From left to right, there are four notable mismatches to these fits. See text for further discussion. **(Bottom)** The difference from the IUVS data and the blue fit above gives the residual (black), compared to a fit of metallic emissions (red). While Mg at 285 nm appears to show a positive identification, this is actually better modeled by an unknown airglow feature as in Figure 1.17.

Most spectral templates are constructed from theoretical calculations which are verified by laboratory measurements, however there are some notable discrepancies relevant to this work. There are several positive residuals in Figure 1.16, indicative the CO Cameron band model has discrepancies in the relative peaks and features which have not been captured. Specifically, there are features at 233, 240, and 244 nm which underestimate emission and a feature at 260 nm, which overestimates emission. This overestimation occurs at the location of a spectral feature of $Fe^+$, where the multiple linear regression code attempts to fit a negative emission to address this, which is clearly unphysical. These emissions are removed from the data during retrieval of metal emissions during the comet Siding Spring era by comparisons with observations taken before comet Siding Spring.

The features at 280 and 285 nm from Figure 1.16 are the "persistent layer" of $Mg^+$ (Chapter 4) and an unknown airglow feature, respectively. The $CO_2^+$ Ultraviolet Doublet demonstrates a shoulder on the short wavelength side of the emission which is well correlated with the airglow peak, but not seen in laboratory studies (Figure 1.17) and which overlaps the Mg 285 nm emission. We remove the shoulder emission by fitting the residual near the airglow peak with a double gaussian of fixed width and heights.

The location of the spectrum in wavelength space must be determined from the data, as it has been observed to move spectrally, varying by both spatial bin and scan. The reason for this is not known exactly, and we have compared detector and instrument temperature with this shift without finding a strong correlation. We observe this in the FUV and MUV, however the shifts appear to move in the opposite direction, indicating this may be a function of the beam splitter position relative to the detectors (see SPT in Figure 1.11). We determine the MUV wavelength scale by fitting the $CO_2^+$ Ultraviolet Doublet (UVD) at 290 nm, which can be observed on the dayside (at solar zenith angles less than 110) near the airglow peak.

The solar template has a significantly different spectral shape than observed in the Sun's photosphere (Rottman et al., 2006), and it is necessary to construct a template from observations of Mars' atmosphere instead (Figure 1.18). The difference in spectral shape

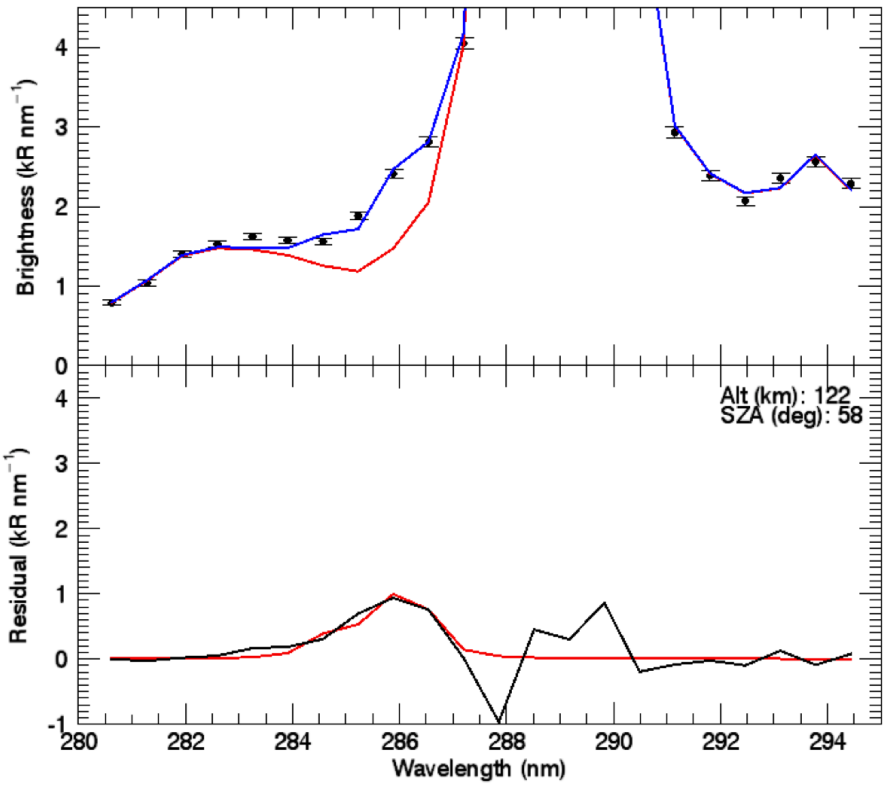


Figure 1.17: **(Top)** IUVS data (black dots) is compared to a composite fit of typical airglow emissions in the absence of this unknown airglow feature (red), and in its presence (blue). See text for further discussion. **(Bottom)** The difference from the IUVS data and the red fit above gives the residual (black), compared to a double gaussian fit of this unknown feature. This emission is well correlated with the airglow peak, and does not match the spectral shape expected for the Mg 285 nm emission.

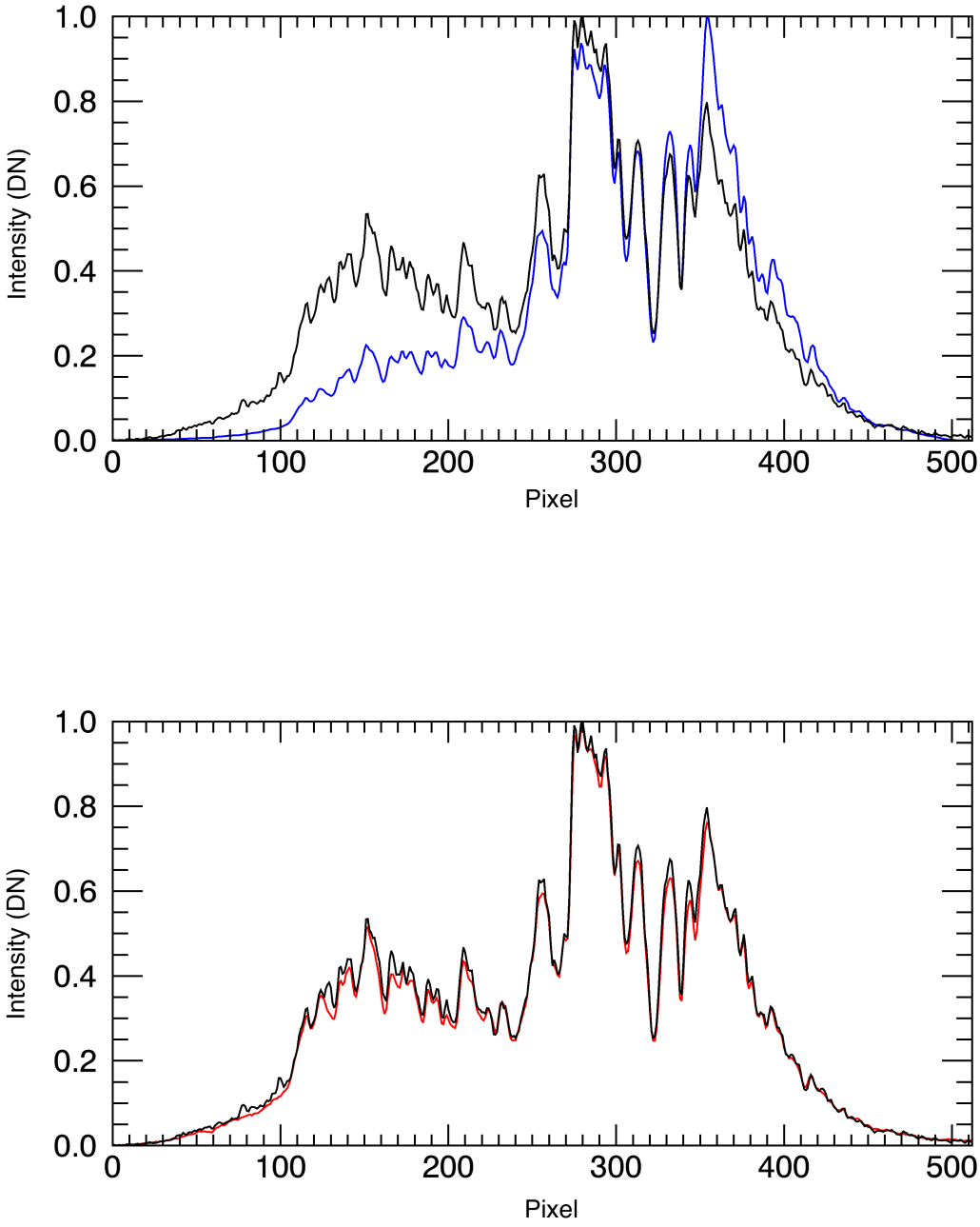


Figure 1.18: In both images the intensity is normalized to unity, and the data is represented in DNs, demonstrating that the IUVS sensitivity falls off with long wavelengths. **(Top)** Comparison of the MUV SORCE solar spectrum (blue) to that observed by IUVS (black). **(Bottom)** Comparison of the MUV data derived solar spectrum used as a template (red) to that observed by IUVS (black).

is likely due to scattering of dust in the Martian atmosphere, which appears bluer than SORCE. We construct the solar template using high resolution observations, taken in the limb observing mode with tangent points below the airglow peak, which can be compared to observations of the disk and SORCE spectrum.

### 1.5.5 Density Retrieval

Spectral emissions are co-added by altitude to create vertical profiles of atmospheric species. For optically thin emissions, it is valid to approximate the emission as occurring in a circularly symmetric fashion, where the emission represents an integrated column density along a straight line of sight tangent to the planet's surface (Figure 1.19). The Abel transform for intensity along a line of sight where solar extinction and deactivation are negligible everywhere is then described by (Chamberlain and Hunten, 1987):

$$\begin{aligned} n(y) &= \int_{-\infty}^{\infty} N(x)dx \\ &= 2N(y)ye^{y/H}K_1(y/H) \end{aligned} \tag{1.7}$$

where $N$ is the column density along the line of sight, $n$ is the density at the tangent point, $H$ is the scale height of the atmosphere, $y$ and $x$ are defined in Figure 1.19 and $K_1$ is the modified Bessel function of the first kind. To determine the column density, it is necessary to use the emission's g-factor which relates the intensity of an optically thin emission to a column density (Dymond et al., 2003):

$$4\pi I = 10^{-6} g_{J',J''} N \tag{1.8}$$

where $4\pi I$ is the column intensity (given in Rayleighs, where $10^{-6}$ converts this appropriately), $g$ is the g-factor, $N$ is the column density in cm$^{-2}$. We define the g-factor, which is a measure of the scattering efficiency of the absorber as:

$$g_{J',J''} = \frac{\pi e^2}{mc^2} \frac{A_{J',J''}}{\sum_{J''} A_{J',J''}} \sum_{J''} n_{J''} \pi F(\lambda_{J',J''}) \lambda^2_{J',J''} f_{J',J''} \tag{1.9}$$

where $\pi F(\lambda_{J',J''})$ is the solar flux at the relevant wavelength, $J''$ is the oscillator strength, $e$ is the electronic charge, $m$ is the electron mass, $c$ is the speed of light, $A_{J',J''}$ is the Einstein A coefficient, $n_{J''}$ is the population of the ground state relative to the total ground, and $J'$ and $J''$ are the total orbital angular momentum quantum numbers for the levels of the excited and ground states. These approximations are invalid in the presence of optically thick emissions, and require full radiative transfer retrievals to determine their density (Evans et al., 2015).

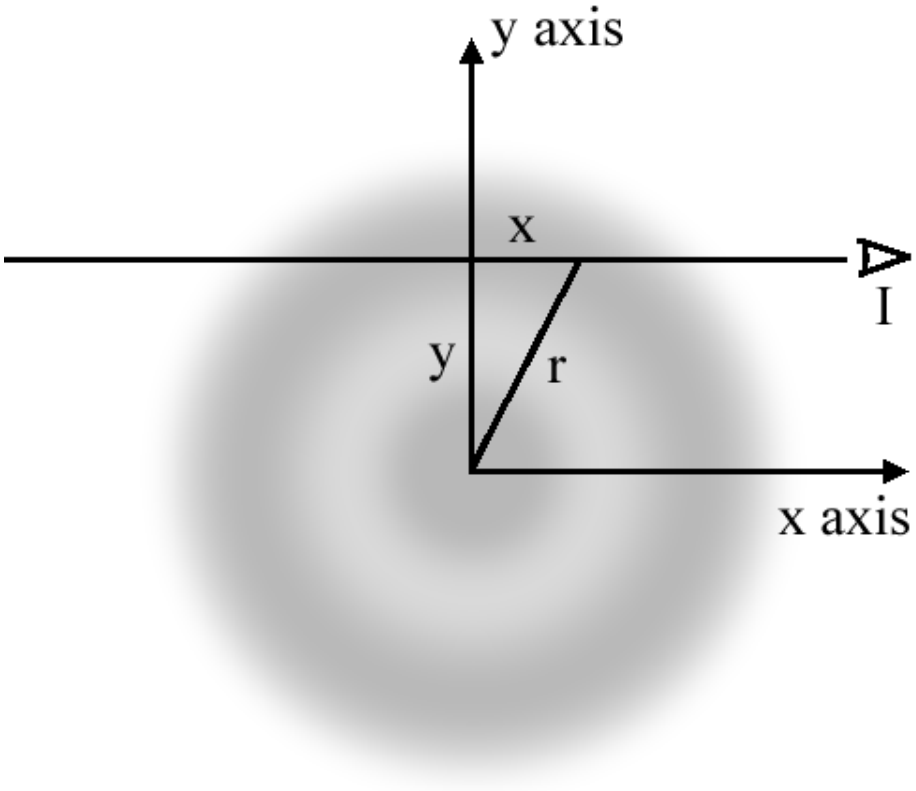


Figure 1.19: A geometrical interpretation of the Abel transform in two dimensions, where the observer views along I, and r is the distance from the planet's center to the parcel integrated along. This integration then occurs along the entirety of the x line to give the intensity at a height, y.

## 1.6 Outline of this work

In detailing the work carried out by this thesis, four manuscripts roughly shape each of the following chapters:

- Chapter 2 describes the gaseous coma of comet Siding Spring, and the cometary gases delivered to Mars as they passed one another. These observations are used to constrain the total delivered gaseous mass and the implications for observable perturbations to the upper atmosphere. This work was published as Crismani et al. (2015).

- Chapter 3 describes the metals ablated in the upper atmosphere of Mars as it passed through the debris stream of comet Siding Spring. In particular, we focus on the chemical and dynamical evolution of these ions and neutrals and use this perturbation to investigate new chemical and physical processes. This work will be published as (Crismani et al., in Prep.).

- Chapter 4 describes the ablation of sporadic interplanetary dust particles in the upper atmosphere of Mars, distinct from those due to any shower. This ablation forms a persistent layer, which we use to determine the quiescent meteoric chemistry, constraints on meteor shower fluxes, and the total flux due to the interplanetary dust environment. This work was published as Crismani et al. (2017b).

- Chapter 5 first summarizes this work and then describes its implications, from its impact on the debate of source of $CH_4$ near the Martian surface, implications for understanding previous observations of transient ionospheric layers, and improvements necessary to ionospheric, meteoric chemistry, and transport models. The impact of this work on the Martian methane debate was published as Crismani et al. (2017a). The impact of this work on transient ionospheric layers will be detailed in a paper that is currently in preparation.

# Chapter 2

# Gas from Comet Siding Spring

## 2.1 Introduction

The Mars Atmosphere and Volatile EvolutioN (MAVEN) mission is the first to study the evolution of the Martian atmosphere by determining the drivers and effects of atmospheric loss to space (Jakosky et al., 2015b). Although the interaction of Mars and the gaseous coma of a comet, an event predicted to occur only once in 100,000 years (Ye and Hui, 2014), was not expected during the MAVEN mission, on October 19, 2014, comet C/2013 A1 (Siding Spring) (McNaught et al., 2013) approached within 141,000 km with a velocity relative to Mars of 56 km/s. Because the delivery of mass and energy from impacting cometary dust and gas is in many ways analogous to impulsive solar events that MAVEN was designed to observe, the spacecraft was well positioned to investigate this rare occurrence.

While observations of comets are useful in a broader scientific sense, these observations had a more direct role on MAVEN's primary mission. While the observations were still being planned, the size and production rate of the comet were not determined and the effect on the atmosphere was not well constrained. In order to make sure the subsequent atmospheric measurements were useful and could be interpreted, it was necessary to study the perturber, as well as the state of the atmosphere before and after closest approach.

Some effects of impacting dust have been reported by Schneider et al. (2015b) and Benna et al. (2015), who detected ablated metals in the atmosphere, but the effects of

impacting gas are subtler as gaseous species abundant in comets are naturally present in the Mars atmosphere. MAVEN observations of the comet's coma obtained before the closest approach, however, can be used to determine the mass of impacting gas, which is the most critical quantity in interpreting possible impact-related atmospheric changes.

We use direct measurements of spatially resolved hydrogen brightness and a robust cometary model to determine the comet's water production rate and therefore quantify the flux of cometary gases on the upper atmosphere. Water is responsible for the majority of the mass in the gaseous coma, but there are no features in the ultraviolet (UV) or visible spectrum; we therefore use UV observations of hydrogen as an available proxy. OH is a dissociation product of water, and is observed in cometary coma, however, our observations were not sensitive enough to be able to detect the band emissions of OH near 308 nm.

Using models that describe the production and destruction of chemical species, as well as providing an accurate description of their motions, one can derive the production rate of important volatiles. As water is the most abundant species in the gas coma (Combi et al., 1998), understanding its abundance is paramount to informing comets' chemical composition.

## 2.2 Observations and Data Analysis

### 2.2.1 Observing Details

Our observations use MAVEN's Imaging Ultraviolet Spectrograph (IUVS), which derives atmospheric properties through spectroscopic measurements of UV emissions from atmospheric gases (McClintock et al., 2015). The data are taken in the form of two–dimensional spectrograms, with the horizontal axis corresponding to wavelength, and the vertical axis representing spatial position along the slit, which is 11 degrees tall and 0.06 degrees in the spectral direction. By rotating a scan mirror that moves the position of the slit on the sky, we are able to create data cubes with spatial information on two axes and spectral on the

third. We used the Far UltraViolet (FUV) channel that covers wavelengths between 115 and 190 nm, has a spatial resolution along the slit of 0.8 arcmin/pixel, a spatial resolution across the slit of 3.6 arcmin/pixel, and a spectral resolution of 0.6 nm. Using the Lyman-$\alpha$ emission from hydrogen at 121.6 nm, we construct images of the comet by summing over the spectral width of the line and arranging the measurements according to projected positions on the sky. The spectral and spatial binning is shown in Table 2.1; the projected spatial bin size is a function of the comet's distance from Mars.

IUVS observed Siding Spring once on October 14th, 2014 and three times on October 18th, 2014. Each observation was comprised of 36 scan mirror positions and an integration time of 60 seconds in each position. Between integrations the line of sight moved by single slit widths (3.6 arcmin) perpendicular to the slit's long axis, except for the observation taken on October 18th, 2014 06:00:32 UTC, where we moved it by 5 slit widths (18 arcmin) to increase coverage on the sky. The comet was moving almost directly toward Mars at the time of the observations, so despite the high relative velocity (56 km/s), the apparent motion on the sky is negligible compared to the spatial resolution of our images.

### 2.2.2 Data Processing

Dark frames taken at the beginning and end of each observation were used to subtract dark current. The data were then converted into kiloRayleighs per nanometer, a standard unit of brightness used for airglow (Barth et al., 1971b). Stellar calibration was performed using UV-bright stars (Bet CMa, Bet Cen, and Alp Cru (Snow et al., 2013)) however, there are differences in our observed brightnesses with previous measurements of the Martian hydrogen corona and interplanetary hydrogen. Comparison with Hubble Space Telescope, and other Lyman-$\alpha$ observing instruments, such as Mars Express/SPICAM (Bertaux et al., 2006), SORCE/SOLSTICE (McClintock et al., 2005b,a), and SOHO/SWAN (Bertaux et al., 1995) indicate a discrepancy of order 20%. To account for this, we reduced our intensities with a model scale factor of $\sim$1.2 as this allows appropriate comparison with other observa-

Table 2.1: Information for the four observations of comet C/2013 A1(Siding Spring). Spatial bins are constructed by binning pixels along the length of the slit, and the spatial resolution below reflects this binning. The data have been publicly archived at the Planetary Atmospheres node of the Planetary Data System (PDS); to retrieve these files use the filename from the footnote.

| Observation Date & Time (UTC) | Mars-Comet Distance ($10^6$ km) | Hours Before Closest Approach | Angular Width (deg) | Resolution Spectral (nm) | Resolution Spatial (") | Number of Spatial Bins |
|---|---|---|---|---|---|---|
| Oct 14, 2014 11:33:32[1] | 25.56 | 126.8 | 2 | 1.2 | 96 | 75 |
| Oct 18, 2014 03:02:40[2] | 7.95 | 39.4 | 2 | 1.2 | 190 | 37 |
| Oct 18, 2014 05:20:21[3] | 7.54 | 37.1 | 2 | 1.2 | 190 | 37 |
| Oct 18, 2014 06:00:32[4] | 7.34 | 36.4 | 10 | 1.8 | 190 | 200 |

[1] mvn_iuv_l1b_APP1-orbit00087-mode0821-fuv_20141014T113335_v02_r01
[2] mvn_iuv_l1b_comet-orbit00106-mode0021-fuv_20141018T030240_v02_r01
[3] mvn_iuv_l1b_comet-orbit00106-mode0022-fuv_20141018T052021_v02_r01
[4] mvn_iuv_l1b_comet-orbit00106-mode0041-fuv_20141018T060032_v02_r01

tories and assigned a 25% systematic error. This affects our retrieved water production rates and inferred masses, as these are directly proportional to the assumed model scale factor.

The cometary hydrogen signal lies on top of a background from interplanetary hydrogen plus a substantial foreground from the Martian hydrogen corona. We model and subtract these signals to find the distribution of cometary hydrogen across the sky. We use the model described by Chaffin et al. (2014, 2015), developed for IUVS to characterize the Martian hydrogen corona, the model of Lallement et al. (1985) to compute the interplanetary hydrogen background and the model of Tenishev et al. (2008) and references therein to model the cometary coma. We simultaneously fit the data to the foreground and radial cometary models by the method of minimum $\chi^2$, and find agreement with nominal coronal parameters within 5%. The foreground signal is the dominant signal in most of the images (Figure 2.1), and this subtraction leaves a majority of pixels with a uniform uncertainty of $\sim$30%.

The foreground model assumes spherical symmetry, but as described in Chaffin et al. (2015), the hydrogen corona is at least slightly asymmetric and this creates an excess of negative values, shown as darker pixels in Figure 2.1, far from the nucleus (>500,000 km). We exclude distances greater than 200,000 km in this analysis for two reasons: the foreground model is insufficiently precise to distinguish whether the source of this signal is cometary or coronal, and the cometary signal at these distances is so weak that we cannot reliably distinguish it from detector noise. This distinction does not greatly affect the fitting process as the exclusion of data >200,000 km from the nucleus changes the estimated water production rate by 1%. The location of the nucleus is determined by coincidence of the brightest pixel in the image with the ephemeris reported by JPL (2015), and from this we produce radial profiles of hydrogen by averaging the data into spatial bins detailed in Table 2.1, effectively reducing the random uncertainties for each bin to $\sim$5%.

Correcting for the Martian and interplanetary hydrogen components, the measured brightnesses were converted into column densities using the appropriate g-factor (Chamberlain and Hunten, 1987). The observed radial profile from October 14th, 2014 (Figure 2.2)

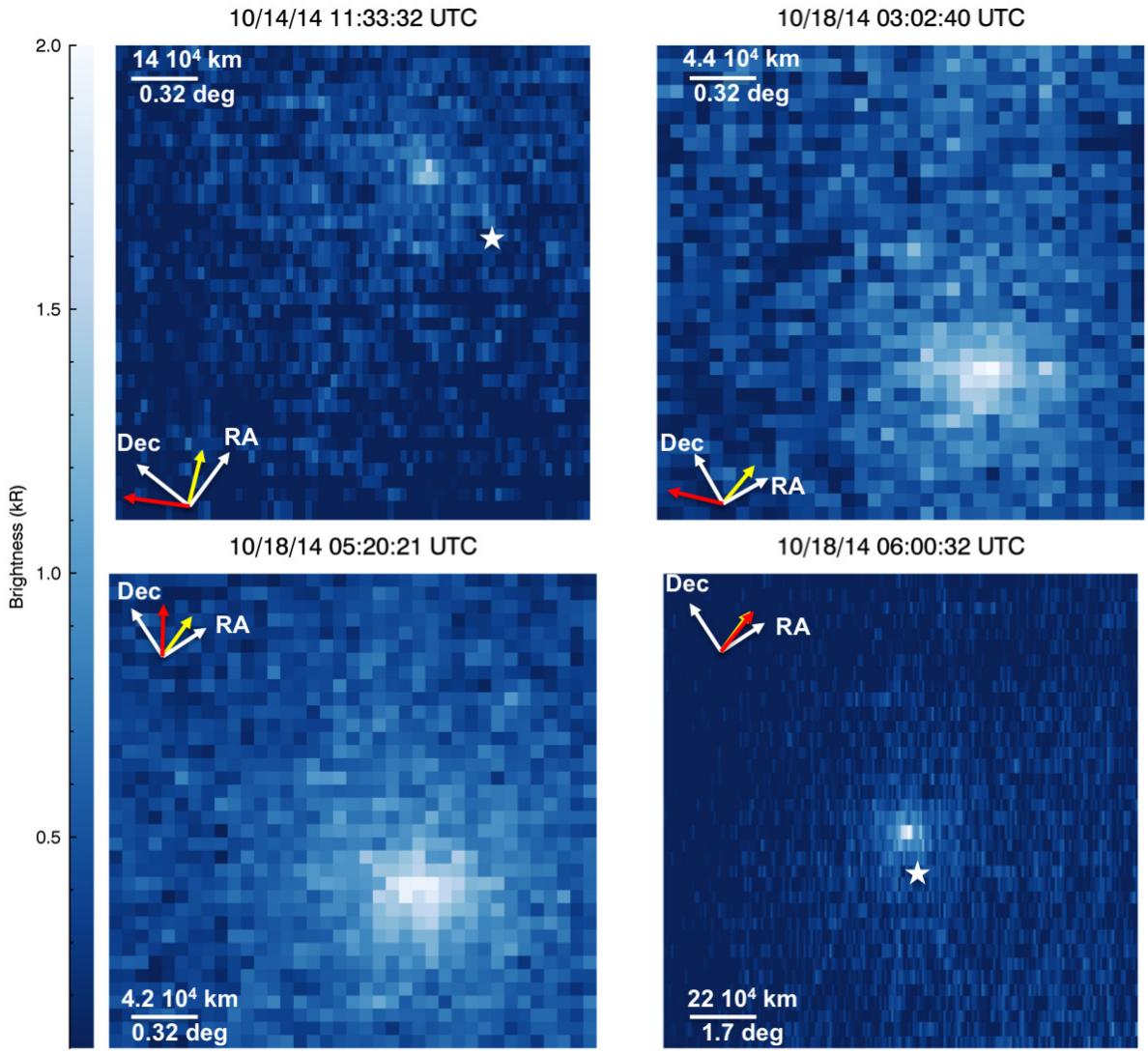


Figure 2.1: Images of comet C/2013 A1 (Siding Spring), taken on Oct 14th and 18th, corrected for dark current, foreground and background signals. A white star shows the approximate location where Mars encountered the gaseous coma. The images are oriented with increasing RA and declination aligned along the white arrows. The direction of the Sun and Mars is shown with a yellow and red arrow, respectively. The slit is aligned horizontally, and the vertical axis spans the range of mirror motion on the sky.

within 50,000 km deviates from the best-fit model, but the inferred water production rate for this observation is within 10% of the subsequent observations, and therefore we do not include this as a distinct measurement. Due to an incomplete foreground subtraction rather than any cometary effect, the radial profile from October 18th, 2014 3:02 UTC is also statistically different from the model at distances greater than 150,000 km, shown as an excess of bright pixels near the top of the second image in Figure 2.1.

## 2.3 Analysis and Results

### 2.3.1 Cometary Gaseous Production

We estimate the total mass of water and its daughter species that impacted Mars using the observations of hydrogen column density from Figure 2.2. Comparing the measured hydrogen content with a distribution derived from the model of Tenishev et al. (2008) we find a water production rate of $1.1 \pm 0.5 \times 10^{28}$ molecules/s, and from this calculate column densities swept up by Mars during the encounter (Figure 2.3). The mass from $CO_2$ delivered to Mars may be an important perturbation to gaseous species in the upper atmosphere, and as $CO_2$ radial profiles cannot be directly derived from H, we use reported $CO_2$ production rates from Stevenson et al. (2015) taken one month before the encounter.

We predict column densities of water and its daughter species using a fully kinetic Adaptive Mesh Particle Simulation model (Tenishev et al., 2008; Combi et al., 2012; Fougere et al., 2012, 2013; Fougere, 2014). This enables us to model the full coma of Siding Spring, including regions where collisions are not sufficient to maintain a fluid regime. This technique uses the gaseous production rate and heliocentric distance as inputs, and produces radial profiles that we compare against observations. Systematic differences among various measures of water production rates normally fall in the range of 25 - 50%, owing to differences in calibration, background subtraction, model assumptions and model parameter uncertainties and we adopt a conservative systematic uncertainty of 50%. Although the model used

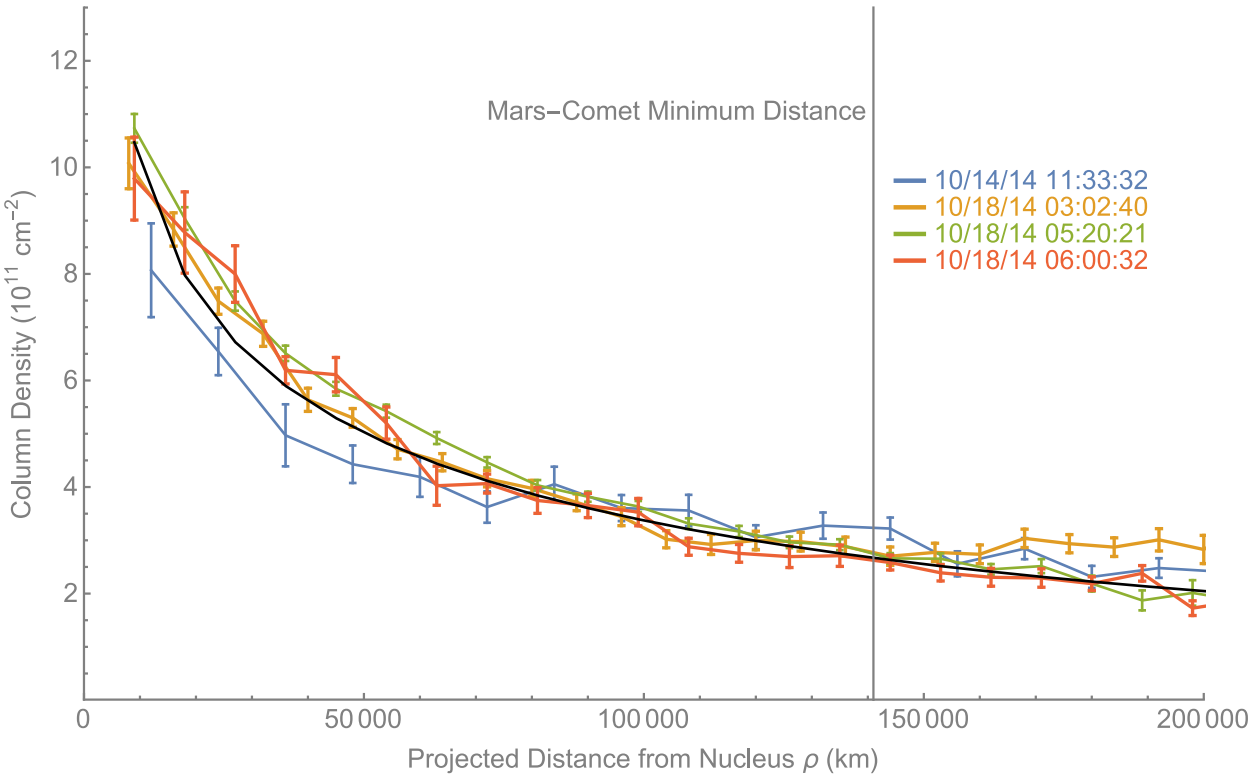


Figure 2.2: Radial distributions of the observed hydrogen column densities for each of the four observations. Constant width binning of annuli centered on the nucleus produced these azimuthally averaged radial profiles. These observations are fit to a model, described herein and shown in black. The 1-$\sigma$ error bars represent the variation derived from the photon statistics of the detector.

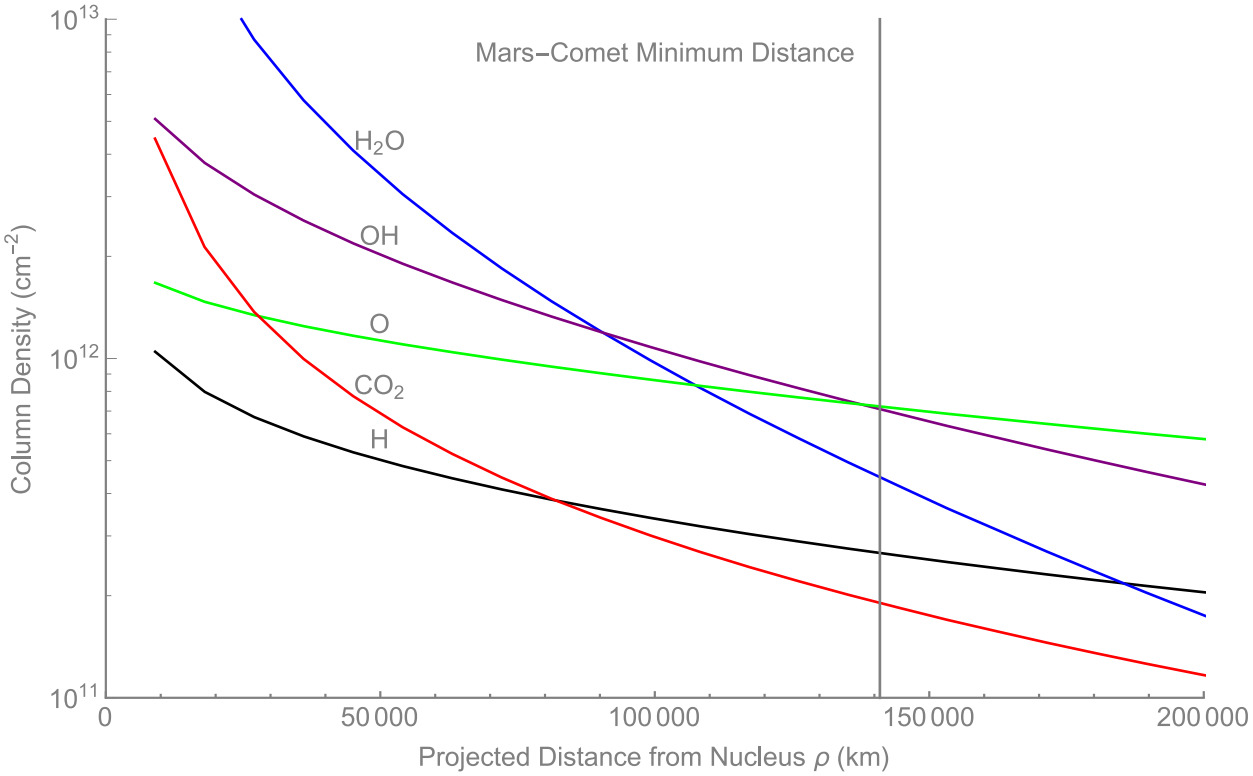


Figure 2.3: Modeled line of sight column densities the major gaseous species derived from the model of Tenishev et al. (2008). The black line shown here for hydrogen corresponds to the same line in Figure 2.2, but the vertical scale is now logarithmic.

includes the expected detailed spatial and velocity distributions of H atoms produced by photodissociation of $H_2O$ and OH, we also used a simple Haser model (Haser, 1957) with an average radial velocity – which yielded a consistent result to within the measurement uncertainty.

The sublimation of water and subsequent photodissociation into OH, O, and H described by this model infer fluxes of mass and energy as shown in Table 2.2. The H profile results from the progressive dissociation of $H_2O$ and OH into its constituent atoms which happens continuously as the gases flow outwards. Our results broadly agree with the work of Bodewits et al. (2015), with differences in relative abundance of daughter species due to a difference in modeling methods: spherically symmetric radial outflow Haser model (see Bodewits et al. (2011)) versus direct simulation modeling, presented here. As ionization and chemical processes will affect these species during deposition, this discrepancy is unlikely to be discernible in subsequent atmospheric observation.

The radial profiles we obtained days in advance of the encounter can be used to estimate the impacting gas mass at the time of closest approach, on the assumption that the profile is steady state, smoothly varying and azimuthally symmetric. The region of interest in the gaseous coma lies far enough from the comet that asymmetries due to ejection and rotational variations are smoothed, but close enough that radiation pressure does not appreciably affect the coma (Combi et al., 2000). Given the small change in heliocentric distance over this time span, no significant temporal variability of sublimation or dissociation is expected.

### 2.3.2 Martian Atmospheric Effects

The total mass of impacting gas is $2.4 \pm 1.2 \times 10^4$ kg and is larger than the total impacting dust mass, 16,000 kg, determined by (Schneider et al., 2015b). However, cometary gases shown in Table 2.2 are unlikely to cause significant mass perturbations in the upper atmosphere. Molecules are expected to dissociate upon entry into the upper atmosphere and we can compare the combined mass of O, C, and H from all parents to the ambient density

| | Particle Flux ($10^7$ cm$^{-2}$ sec$^{-1}$) | Column Energy Density (erg cm$^{-2}$) | Mass (kg) |
|---|---|---|---|
| H | 7 | 7 | 160 |
| O | 20 | 300 | 6900 |
| OH | 19 | 310 | 7000 |
| $H_2O$ | 12 | 200 | 4600 |
| $CO_2$[†] | 5 | 210 | 4900 |
| Total | | 1000 | 24,000 |

[†]Derived from $CO_2$ production rate of Stevenson et al. (2015).

Table 2.2: Impacting fluence of mass and energy for gaseous species from comet Siding Spring. The fluxes are determined using the total impacting model column densities by species averaged over the encounter, where we used a nominal encounter time of 60 minutes (see Yelle et al. (2014) for details). Values derived from water are valid within 50% (see text for discussion).

at the predicted penetration depth (∼155 km (Yelle et al., 2014)). The observed cometary oxygen column is equivalent to the amount of oxygen in a 200 m layer of Mars atmosphere at 155 km (Bougher et al., 2015b). Compared to the mass of oxygen above this altitude, we find this is a perturbation of order 1% and, so far, unobservable in the IUVS atmospheric data. As carbon dioxide and carbon monoxide are dominant species in the Martian atmosphere, cometary perturbations to these species are unlikely to be detectable. However, atomic and ionized carbon densities are extremely reduced in comparison, and analysis is underway to determine whether perturbations to carbon are observable by IUVS. The majority of cometary hydrogen delivered to Mars comes from dissociation of $H_2O$ and OH upon entry into the atmosphere, and the delivery from atomic hydrogen is ∼6 times smaller. Cometary hydrogen delivered to the planet from water and its products is $3.4 \pm 1.7 \times 10^{12}$ atoms/cm$^2$ which is comparable to, but smaller than, the abundance of hydrogen at Mars above 150 km (Krasnopolsky, 2002; Chaufray et al., 2008). However, this mass perturbation is difficult to find in subsequent atmospheric observations as the Lyman-$\alpha$ emission from hydrogen is optically thick and doubling the density does not double the observed brightness.

These observations and analysis of early atmospheric data from IUVS allow us to determine the energy delivered to the upper atmosphere and its penetration depth. Water traveling at the relative speed of 56 km/s carries a kinetic energy of 293 eV/molecule, and will deposit oxygen and hydrogen in the upper atmosphere as it is stopped by collisions with ambient species. For a water production rate of $10^{28}$ molecules/s (Yelle et al., 2014) predicted impacting water and its daughter species should increase the temperature in the upper atmosphere by 30 K. Temperatures derived from observed typical scale heights from IUVS limb scans (Jain et al., 2015) before the comet encounter indicate the atmospheric temperature may be 100 K larger than those assumed by (Yelle et al., 2014). The penetration depth is sensitive to the assumed atmospheric temperature and this disparity indicates the thermospheric effect would have occurred ∼20 km higher than predicted. Further analysis will be necessary to determine whether IUVS is able to detect this 10% perturbation as

the work by Jain et al. (2015) uses an exponential fit to derive scale heights, and ongoing analysis will be able to produce temperature that is resolved in altitude. It is unlikely that any perturbation to the thermosphere would be identified, as the Martian thermosphere exhibits variability in scale heights from orbit to orbit. Comparisons with NGIMS is not possible in this region, as the spacecraft did not go lower than 185 km for this time period.

## 2.4 Conclusions

Measurements of the hydrogen coma density allow us to infer the water production rate for comet Siding Spring before its close encounter with Mars. We find a water production rate of $1.1 \pm 0.5 \times 10^{28}$ molecules/s by fitting observed radial profiles to predictions from a robust cometary model. From this value, we are able to determine the total mass of gaseous material that impacted Mars from water and its daughter species. The addition of O, OH, and $H_2O$ at orbital velocities may contribute to an ionospheric layer at 150 km, however such a perturbation would last on the order of minutes or tens of minutes before ionospheric chemistry restored the ionospheric topside to normal.

We use inferred impacting gaseous masses to revisit and reconcile predictions, finding agreement that the oxygen perturbation is negligible, prompting further work in the analysis of carbon, and determining the hydrogen perturbation would be unobservable in the IUVS data. The prediction of a thermospheric response due to energy deposition in the upper atmosphere is unchanged by these findings, however we posit that such perturbations should exist at higher altitudes due to the difference between observed and predicted atmospheric temperatures above 150 km.

# Chapter 3

# Dust from Comet Siding Spring

## 3.1 Introduction

On October 19th 2014, the dynamically new Oort cloud comet C/2013 A1 (Siding Spring) had a close encounter with Mars, passing within 141,000 km of the planet (McNaught et al., 2013). On a retrograde hyperbolic orbit, the comet made its closest approach to Mars at 18:29 UTC with a relative velocity of 56 km/s. In addition to gaseous deposition (Crismani et al., 2015), ionospheric perturbation (Gurnett et al., 2015; Restano et al., 2015), and magnetospheric interactions (Espley et al., 2015), comet Siding Spring also deposited 16,000 kg of cometary dust (Schneider et al., 2015b; Benna et al., 2015) causing the only meteor shower observed at another planet.

Ablation occurs as interplanetary dust particles collide with ambient atmospheric gases at orbital velocities, leading to melting, vaporization, and the release of metallic atoms (e.g. Mg, Fe, Na) in the upper atmosphere (Istomin, 1963; Anderson and Barth, 1971). Terrestrial ablation occurs at an altitude where the pressure is $\sim$1 $\mu$bar, or 80-110 km, corresponding to an average entry velocity of 15 km/s (Carrillo-Sánchez et al., 2016). Terrestrial species have been well studied and a model of ablation and subsequent evolution has been validated for the Earth (Vondrak et al., 2008). This understanding can be applied to comet Siding Spring's Martian meteor shower, noting the increased relative velocity (56 km/s) and relevant atmospheric chemistry.

Meteor showers are common at the Earth, however no significant enhancements in the

terrestrial meteoric ion flux have been attributed to them (Grebowsky et al., 1998). This is not surprising given the mass deposited by a meteor shower is considered to be negligible compared to the sporadic background of ablating meteors (30-60 tonnes/day) (Plane, 2012). While visible meteors are seen to be enhanced during meteor showers, the terrestrial metallic ion layer is primarily composed of ablated particles with masses less than $10^{-3}$ g, whereas visible meteors are composed of particles of mass $10^{-3}$ to $10^{4}$ g (Flynn, 2002), and this latter population contributes a minor mass fraction overall.

Comet Siding Spring's meteor shower is the exception due to its unusually high fluence, 16 tonnes in less than a day (Schneider et al., 2015b), compared to the "persistent layer" from sporadically ablating meteors (2-3 tonnes/day) (Crismani et al., 2017b). For this reason, we observed an large enhancement to the metallic ion layer, and were able to observe species (Mg, Fe, $Fe^{+}$) not typically observable in the persistent layer ($Mg^{+}$). Although transient ionospheric layers observed in the Martian atmosphere have previously been attributed to meteor showers (Pätzold et al., 2005; Withers et al., 2008), Crismani et al. (2017b) shows these are unlikely to be formed from meteoric ablation.

Comet Siding Spring's meteor shower dust predictions ranged from meteor storm (Vaubaillon et al., 2014) to virtually nonexistent (Kelley et al., 2014), with the Schneider et al. (2015b) observations falling closer to the storm end of this spectrum. Therefore IUVS observations can resolve some characteristics of the stream from observations of the aftermath of the meteor shower. Predictions suggest that dust ejected from the comet would remain confined in a stream that lagged behind the comet in its orbit and intercept the planet about two hours after closest approach (Tricarico et al., 2014). The dust was expected to impact the hemisphere centered near the morning terminator close to the equator. Maximum dust deposition was predicted to occur between Oct 19th 19:59 and 20:09, and to last between 20 and 100 minutes.

## 3.2 Observation and Data Processing

### 3.2.1 Observing Geometry

The Mars Atmosphere and Volatile EvolutioN (MAVEN) mission entered an elliptical orbit around Mars on September 21, 2014, about a month before the comet encounter, with a primary mission intended to study the upper atmosphere and the escape of its constituent gases to space (Jakosky et al., 2015b). While designed to study the response of Mars' upper atmosphere to solar influences (Jakosky et al., 2015a), it is coincidentally well instrumented to observe this unique cometary interaction.

MAVEN's remote sensing instrument for studying Mars' upper atmosphere is the Imaging Ultraviolet Spectrograph (IUVS) (McClintock et al., 2015). This instrument observes in the far and middle UV (110-190 nm and 190-340 nm) in separate channels, and measures atmospheric emissions from $CO_2$, its dissociation and ionization products as well as atomic and molecular species such as O and $N_2$. In the periapse observing mode, the instrument uses a scan mirror to construct vertical profiles of emergent radiation from the atmosphere at the limb, over the altitude range 90 - 250 km. Each orbit, IUVS takes up to 12 limb scans in a $\sim$22 minute observation period spanning $\sim$45 degrees around the planet.

The periapse segment of the MAVEN orbit was designed to provide geographic coverage with similar observing conditions within about 5 orbits. For example, the geographical (latitude and longitude) footprint of the spacecraft in orbits 109 and 114 are not significantly different for our purposes. Periapse scans for the Siding Spring era begin at high latitudes and move toward the equator, from latitudes of 50N to 5S and from local times of 10 to 14 hours as the scans move from West to East geographic longitudes. We distinguish scans taken in the beginning or end of periapse as western or eastern, respectively.

To minimize potential risk to the spacecraft, MAVEN's orbit was phased to place the spacecraft behind Mars (relative to the dust flux) at the predicted time of maximum dust deposition. During this time, the spacecraft was commanded into a protective mode and

IUVS halted observations. The Siding Spring era is comprised of observations that were taken from orbit 109 (18 October 16:05 UT) to orbit 128 (22 October 07:49 UT), with the exception of orbit 115, which was MAVEN's hiding orbit.

### 3.2.2 Spectral Emissions and Vertical Profiles

In Figure 3.1 we use IUVS observations of the Mars atmosphere taken after the comet's closest approach to identify two multiplets of $Fe^+$ and Fe, the atomic Mg line, and the previously observed $Mg^+$ doublet. The $Mg^+$ line at 280 nm was detected in pre-encounter observations and for the remainder of the mission as a persistent layer attributable to the ablation of sporadic meteors (Crismani et al., 2017b). MAVEN's NGIMS instrument (Benna et al., 2015) also detected $Mg^+$ and $Fe^+$ during the Siding Spring encounter, as well as 10 other ions. We report no detection of these other ions during this period, however the expected brightnesses of these ions (not $Mg^+$ or $Fe^+$) would have been below IUVS' sensitivity and therefore this result is not unexpected.

All metal emissions discussed herein are due to resonant scattering of solar UV photons, rather than direct excitation during ablation. The model spectrum for each species was constructed using their respective line positions, atomic constants for resonant scattering, and the solar MUV spectrum (Smith et al., 1995; Dymond et al., 2003; Kelleher and Podobedova, 2008; McClintock et al., 2005b; Hearn et al., 1983). Metallic species brightnesses were extracted from a composite spectrum fit of ambient atmospheric gases through multiple linear regression fits of independent spectral components, and subsequently co-added by 5 km bins (Stevens et al., 2011). Data processing techniques are outlined in detail in previous MAVEN/IUVS papers [Schneider et al., 2015a, Evans et al., 2015, Stevens et al., 2015, Jain et al., 2015, Crismani et al., 2017a].

Residual brightness is found in high SNR spectra from orbits 116-118 that suggest an unresolved issue when comparing observations to expected multiplet shapes. This excess brightness appears to be correlated with the multiplet shape of $Fe^+$ at 238 nm and 260 nm

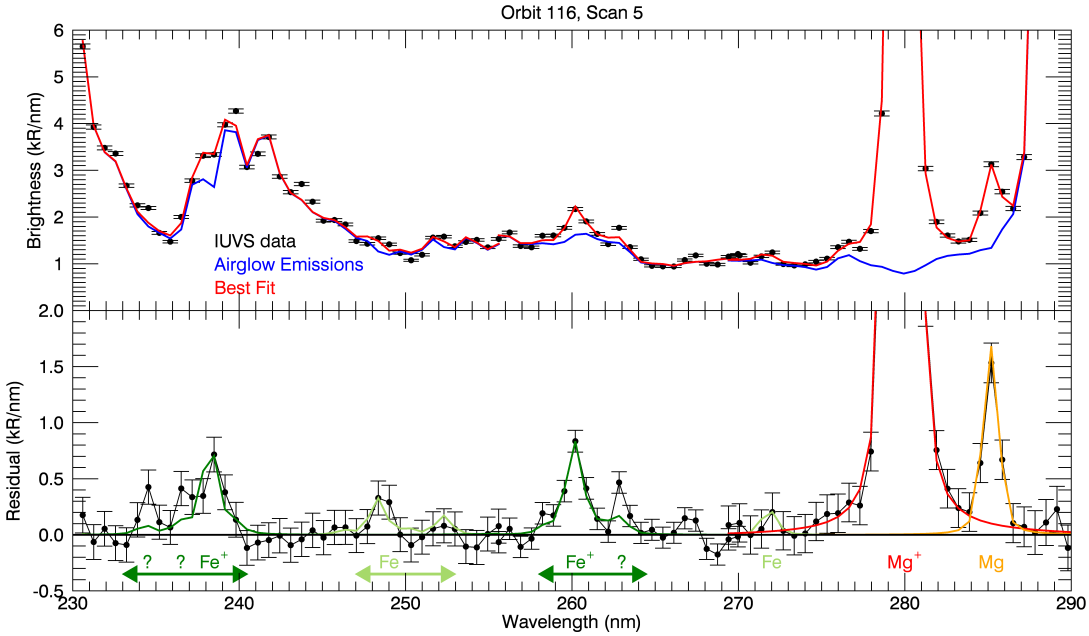


Figure 3.1: **(Top)** IUVS spectrum (black) taken after the close approach of comet Siding Spring, compared to two model spectra: (blue) ambient atmospheric species (CO, $CO_2$+, N2, etc.) with scattered solar continuum from the Martian surface, and (red) the addition of ablated metallic species ($Mg^+$, Mg, $Fe^+$, and Fe). This data is the result of a 4.4 second integration co-added over the 10 degree slit at 115 km altitude. Error bars are constructed from the Poisson noise of the detector. **(Bottom)** The difference between the IUVS data (black, top) and the ambient species (blue, top) gives the residual (black, bottom) to which the metallic species are fit.

(indicated by green ? in Figure 3.1), indicative that discrepancies may exist between measured and observed atomic constants (Ralchenko et al., 2005), or some other unexplained phenomenon. This excess brightness is seen in most scans and altitudes where $Fe^+$ can be observed, is strongest near 110 km, and does not correspond to any other reasonable metallic emission.

At their peak altitude, all observed metallic emissions after initial deposition are optically thick at line center, from $\tau = 15$ to 60 for various emissions (Table 3.1). The absorption cross section is tabulated for the strongest line in a multiplet (e.g. 238 nm for $Fe^+$, 279 nm for $Mg^+$), and compared to their respective column density derived from an inversion of IUVS' brightnesses. Emissions are expected to be optically thin well above the peak altitude, however near the peak and below, we use an Abel transform to retrieve the shape of the emission (Chamberlain and Hunten, 1987). While this is unsuitable for deriving absolute densities, for the purposes of this work, we rely only on the relative shape and presence of other species, and infer no additional information from the absolute densities. A more substantial treatment of $Mg^+$ was achieved in Schneider et al. (2015b) and a similarly rigorous treatment is applied to Mg, $Fe^+$, and Fe in Plane et al., [2018].

Careful attention has been paid to determine whether variations in emissions' vertical profiles or horizontal distributions are the result of random or systematic errors. We use the strong correlation in brightness between adjacent slit elements and from scan to scan to conclude that random noise cannot produce these observations (Figure 3.2). We have also compared these profiles to other retrieved emissions, such as the $CO_2^+$ Ultraviolet Doublet and the reflected solar continuum, which are produced by photodissociation or reflection from dust in the lower atmosphere, respectively. That these emissions demonstrate differing vertical profiles indicates a different production process, and suggests these emissions are not the result of a systematic error in data processing.

The results of Schneider et al. (2015b) used the preliminary radiometric calibration available at the time. This work uses the updated calibration made possible by more ex-

tensive stellar calibration and cross-calibration with the Mars Express SPICAM instrument (Leblanc et al., 2006). The revised calibration places observed brightnesses near the high end of the range reported previously, and removes the systematic uncertainty that was ascribed therein.

### 3.2.3 Chemical Ablation Model

The 1-D model used for this study is the 1-D Chemical ABlation MODel (CABMOD) (Whalley and Plane, 2010), which describes the ablation physics and chemistry, coupled to a 1-D atmospheric model that tracks subsequent atmospheric chemistry. The ablation code MAGMA (Fegley and Cameron, 1987) models the melting and vaporization of entrained minerals in a dust grain, and determines the relevant concentrations of metallic species by altitude. Neutrals and ions are directly deposited during ablation, the latter by hyper-thermal collisions of neutral species with ambient species due to comet Siding Spring's relative velocity (56 km/s). Ablation height is related to particle velocity, where increased speeds lead to ablation at higher altitudes for a given particle density (CarrilloSánchez et al., 2015). The model uses a Mars composition atmosphere ($CO_2$, O, $O_2$, $H_2O$, H, $O_3$, and their appropriate ions) to model the resultant chemistry and transport of metallic species (for details see [Plane et al., 2018]).

CABMOD was optimized to agree with the IUVS-measured peak of the persistent layer of $Mg^+$ near 95 km from sporadic meteors (Crismani et al., 2017b). This model is run for daytime low-latitude conditions, and does not vary local time conditions or include any magnetic field effects. The molecular diffusion coefficient is specified for a homopause region near 120 km, consistent with measurements made by the NGIMS instrument on MAVEN (Jakosky et al., 2017).

Rather than photoionization, charge transfer with the primary ambient ion, $O_2^+$, is responsible for ionizing Mg and Fe between 90 and 190 km. After these ions form, recombination with $CO_2$ is heavily favored over $O_3$ or $O_2$ and the resulting $CO_2$ cluster ions undergo

rapid switching to form $MgO_2^+$ or $MgO^+$, and Fe analogously. Mg and Fe cluster ions have different end states after this, as atomic O reduces Mg-cluster ions to $Mg^+$, whereas Fe-cluster ions are destroyed by electron dissociative recombination. Lifetimes for $Mg^+$ and $Fe^+$ are related to their altitude and inversely related to the ambient electron density, therefore at high altitudes we expect that all the metallic species should be ionized.

## 3.3 Analysis and Results

### 3.3.1 Hemispheric Dust Deposition

The spatial distribution and orbit-by-orbit evolution of $Mg^+$ reveal that ablation occurred only on one hemisphere (hereafter called the exposed hemisphere, Figure 3.2). IUVS periapse observations are separated by MAVEN's 4.5 orbital period, which we use a reference timescale in the discussion below. The tangent points of limb scan observations on orbits 116 and 117 were on this exposed hemisphere during the time of predicted deposition, with the geographic footprint of orbit 116 in the morning quadrant and orbit 117 in the predawn quadrant. By comparing the geographic distribution of $Mg^+$ between orbits 114, 116, and 117, and then to variations within orbit 116, we will progressively reduce the possible encounter time to 3.5 hours, constraining the deposition to a single hemisphere.

Consideration of the overall $Mg^+$ abundance and its vertical distribution offer increasingly tighter constraints on the duration of the meteor shower. We can constrain the timescale for the onset of deposition to less than 9 hours, as metallic emissions in observed in orbit 114 are indistinguishable from background conditions. If IUVS had made observations during orbit 115, the expected time of maximum dust deposition, we would not have expected these observations to contain significant $Mg^+$ as the observed region was on the dayside edge of the exposed hemisphere (Figure 3.2, left). Furthermore, the region observed during orbit 118 must not have been exposed to significant deposition as the total $Mg^+$ content that is less than 20% of that found in orbits 116 or 117. Furthermore, the layer of

Table 3.1: Optical properties of observed metallic emissions during orbit 116 near an altitude of 120 km.

| Species | $Fe^+$ | Fe | $Fe^+$ | Fe | $Mg^+$ | Mg |
|---|---|---|---|---|---|---|
| Wavelength | 238 | 248 | 260 | 272 | 280 | 285 |
| Line of Sight Intensity [kR] | 1.5 | 1.6 | 2 | 0.5 | 29 | 2 |
| g-Factor | 2e-3 | 2e-3 | 7e-3 | 1e-3 | 8e-2 | 3e-2 |
| Absorption Cross Section [cm2] | 6e-12 | 4e-12 | 5e-12 | 3e-12 | 9e-12 | 3e-11 |
| Column Density [cm-2] | 9e12 | 3e12 | 4e12 | 6e12 | 7e12 | 8e11 |
| Optical Depth | 60 | 30 | 20 | 15 | 60 | 20 |

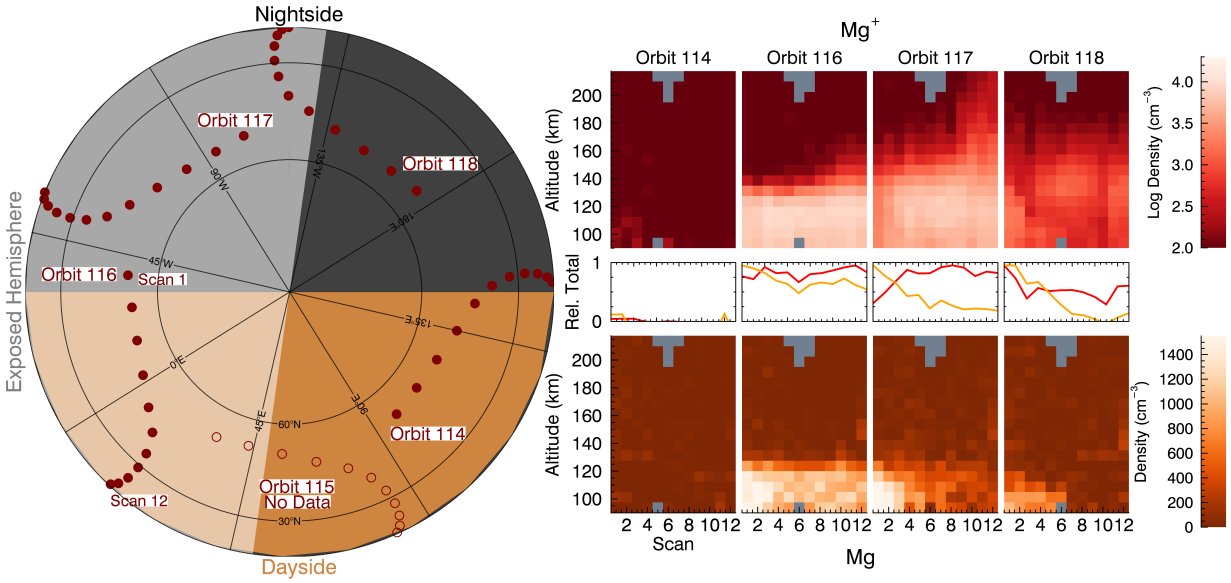


Figure 3.2: **(Left)** A geographical representation of observed regions of Mars at the predicted time of dust deposition, where the tangent points of orbits 114, 116, 117, and 118 are shown with maroon circles, with scans beginning at high latitudes and ending near the equator. In reality, MAVEN stays fixed with respect to the sun (to the bottom of this image), and the planet rotates underneath it. **(Right)** Orbit by orbit images of $Mg^+$ and Mg (top and bottom) constructed by co-adding spectra by altitude (shown on the vertical axis), and adjacent scans are shown on the horizontal axis, which spans 1000 km. Line plots ($Mg^+$ = red, Mg = orange) in the center of the images indicate the total metallic content between 90 and 180 km normalized to each orbit. Measurements before the comet's passage (orbit 114, at right) are consistent with the persistent layer of $Mg^+$ and no observable Mg in the atmosphere.

$Mg^+$ from orbit 118 lies above altitudes where deposition can occur (Section 3.3.3) and must have been transported there.

The tightest constraints on timescale come from a comparison of relevant deposition timescales and total $Mg^+$ abundances observed in orbit 116 and 117. Deposition is expected to be spatially uniform as Mars is small compared to the scales appropriate for cometary debris streams. To first order, the cumulative amount of $Mg^+$ is related to the time a region spent on the exposed hemisphere during deposition. If the duration of the shower is long compared to 4.5 hours, the geographical locations observed in orbit 117 would have experienced greater deposition and have significantly more $Mg^+$. In fact, we see the opposite, where $Mg^+$ in orbit 117 is $\sim$80% of that in orbit 116, indicative that the timescale for deposition was short ($<$ 4.5 hours).

We further constrain the deposition timescale by considering the abundance of $Mg^+$ in orbit 116 from West to East scans. If deposition lasted as much as 4.5 hours, western scans would remain in the exposed hemisphere for the entire deposition period, whereas eastern scans would become shielded in 3 hours. Therefore western scans would be expected to have 1.5 times more $Mg^+$ than eastern scans. In fact, the ratio of the 4 most western scans to the 4 most eastern scans is 0.9, indicative that the most intense deposition could have lasted no longer than $\sim$3 hours.

### 3.3.2 Deposition and Initial Evolution

Cometary deposition gives the opportunity to observe the response of the Martian ionosphere to a significant perturbation. Ions and neutrals observed in orbit 116 peak in intensity around 110 - 120 km and decrease rapidly with increasing altitude (Figure 3.3, left). The ions have a roughly exponential emission scale height of $\sim$5.5 km, compared to concurrent observations of the $CO_2$ atmosphere with an $\sim$14 km scale height. The small scale height of the metallic ions implies these species are not yet well mixed, and suggests deposition occurred in a small layer 10-20 km thick at an altitude, 115 km, consistent with

ablation speeds of 56 km/s. Dynamical transport and chemical reprocessing become entwined after initial deposition, as demonstrated when comparing orbits 116 and 117 (4.5 and 9 hours after deposition, respectively).

Comparing subsequent orbits from the exposed hemisphere provides temporal insight in the evolution of this meteoric perturbation. The region observed in orbit 117 (Figure 3.3, right panel) differs from the geographical location as orbit 116 (left panel); however these both represent the exposed hemisphere and deposition is not expected to vary on these spatial scales. In both orbits, neutral emissions show a 5 km scale height and do not extend into the upper atmosphere, which, unlike the ions, we interpret as suppression of the neutrals by rapid charge exchange with $O_2^+$.

The spatial distribution of neutral Mg in a single orbit provides constraints to its lifetime after deposition. Western scans differ from eastern scans in their dayside exposure, where eastern scans spend close to four hours longer in sunlight. In orbit 116, there is a 50% reduction of Mg from western to eastern scans, and in orbit 117 this reduction is closer to 75% (Figure 3.2, right bottom row). This rapid loss of neutral Mg is not fully captured by the newest version of CABMOD (Section 3.2.3), despite constraints inferred by the persistent layer of sporadic meteors (Crismani et al., 2017b).

### 3.3.3 Rapid Horizontal and Vertical Transport of Metallic Species

The hemispheric injection of metals into the atmosphere is analogous to dye in water, providing insight into the global motions of the atmosphere. Figure 3.4 shows the spatial distribution and temporal evolution of $Mg^+$ and $Fe^+$ over four sequential orbits. Both ions are readily observed in all scans of orbits 116-124 (more than 40 hours after closest approach) and their abundance on the unexposed hemisphere implies global redistribution.

The presence of metallic species in orbit 119, antipodal to the meteor shower radiant at the time of predicted max dust flux, constrains the horizontal wind speed to within 180 - 240 m/s. We determine these values by assuming that observations of the region of orbit

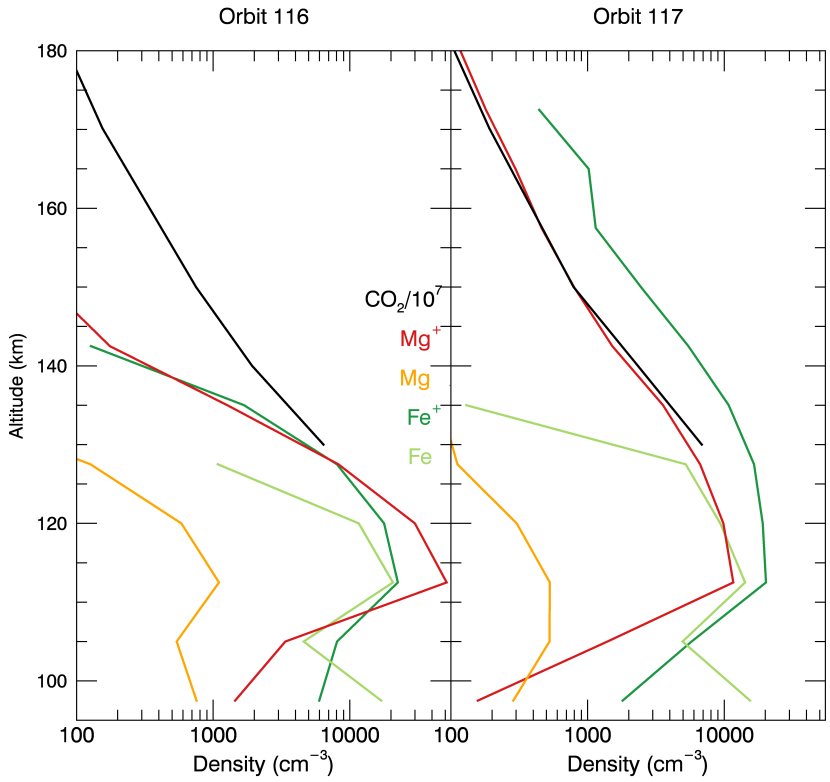


Figure 3.3: Profiles of neutral and ionized metallic species from orbits 116 and 117, averaged across each orbit. These metallic species are compared to the neutral $CO_2$ atmosphere from concurrent IUVS observations, however such retrievals are limited to altitudes above 130 km. It should be noted that scan-to-scan variations in metallic species do exist (Figure 3.5, Section 3.3.4), but are not considered for this figure.

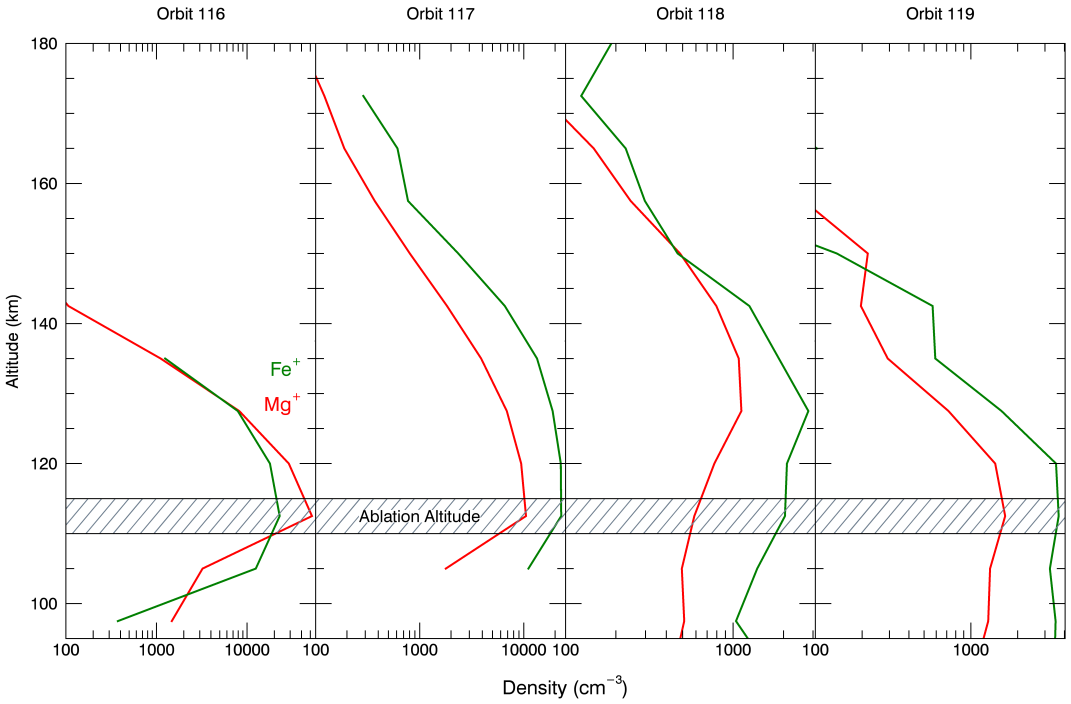


Figure 3.4: Profiles of metallic ions, averaged over the middle of the periapse segment (scans 4-9). The tangent points of each of these orbits can be found in Figure 3.2, where orbit 114 and orbit 119 have roughly the same geographical locations. Deposition occurs at an altitude consistent with entry velocity of 56 km/s (shown as shaded region). As this velocity is close to the dynamical limit for a body interacting with Mars, there is no way for deposition of $Mg^+$ to occur higher than the observed 110-120 km (Section 3.2.3).

117 are the source of ions observed in orbit 119 and that this material has flowed across the nightside. The upper value assumes deposition occurred over a three-hour period, however if deposition were shorter (∼100 minutes) the lower wind speed may be more appropriate. These values are consistent with model expectations, which predict speeds of 160 - 260 m/s at these altitudes of 100 - 120 km (Bougher et al., 1999, 2015b).

The presence of ions in orbit 118 above deposition altitudes (Figure 3.4) indicates they must have been vertically transported, by means that are not yet understood (Section 3.3.6). Orbits 117 and 118 demonstrate vertical transport that exceeds reasonable molecular diffusion rates (1 m/s), and may indicate bulk vertical motion. More perplexing is the similarity in density distribution between orbits 116 and 119, despite their geographic footprints occurring on opposite sides of Mars. If vertical motions describe the transport of orbit 117 and 118, for unknown reasons they do not appear to affect orbit 119.

Mass separation above the homopause (∼120 km) would be expected for $Fe^+$, $Mg^+$ and the $CO_2$ atmosphere as these species are in a region of the atmosphere where the mean free path of particles is large enough that molecular diffusion dominates. Therefore each species should assume a scale height according their masses such that $H_{Mg} < H_{CO_2} < H_{Fe}$. However both metallic species share a common scale height that is distinct from that of $CO_2$ (Figure 3.5). While $CO_2$ atmospheric density profiles do not strongly depend on latitude or solar zenith angle (SZA), metal ion profiles vary from scan to scan. Western scans in orbit 117 have a scale height of ∼13 km, slightly more shallow than the neutral atmosphere whose scale height is ∼14 km, while eastern scans appear to be steeper, with a scale height of 16 km. It is not clear what is causing this variation, as it is not seen in any ambient ions or neutrals, and not expected from standard atmospheric dynamics.

Lack of mass separation in metal ions has also been observed by NGIMS (Grebowsky et al., 2017), however they have not observed a uniform profile whose slope exceeds the neutral atmosphere. Metallic ions are the only species to demonstrate this behavior, and this is likely due partially to their relative lack of chemistry with the background atmosphere.

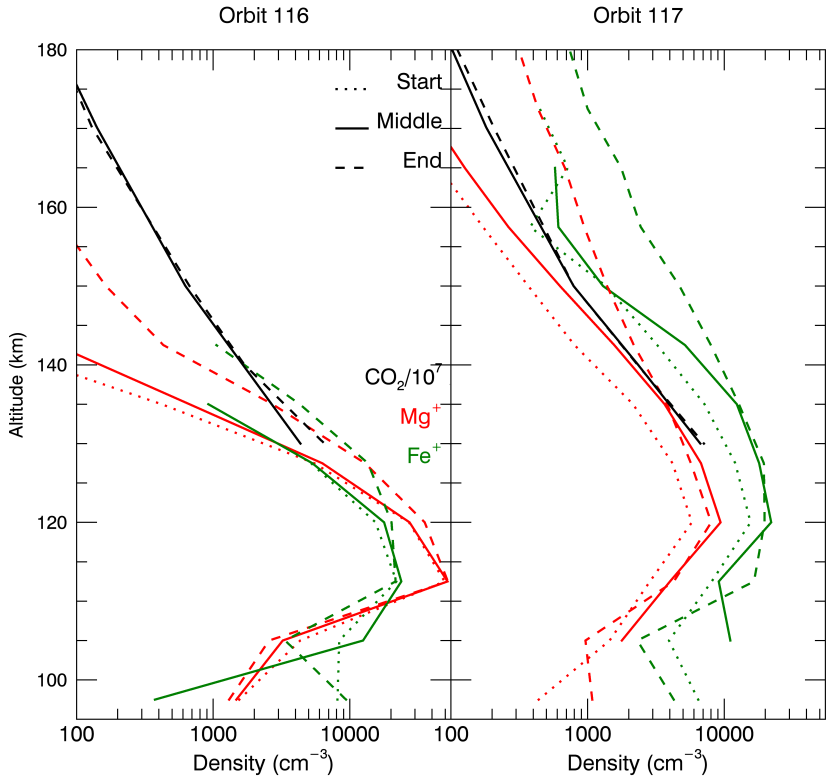


Figure 3.5: Profiles of ionized metallic species from orbits 116 and 117, averaged in sets of four scans (1-4, 5-8, 9-12) and compared to the neutral $CO_2$ atmosphere (black).

Ambient ions such as $CO_2^+$ and $O_2^+$ are strongly regulated by the neutral atmosphere, where typical ion lifetimes due to recombination or other reactions are on the order of minutes, whereas metallic ions can have recombination lifetimes in excess of hours or tens of hours.

### 3.3.4 Potential Mechanisms for Anomalous Vertical Transport

Two plausible electrodynamic mechanisms that could create the anomalous ion scale heights seen in Figure 3.5 are a Lorenz force or an ambipolar electric field. There can be strong vertical magnetic field gradients in the altitude range from 100 to 200 km depending on the ionization at these altitudes. It is possible then that these gradients and field misalignment with horizontal winds may lead to Lorenz forces acting on the metallic species. This mechanism cannot be considered promising until further modeling determines whether these forces produces vertical drift comparable to the diffusion speeds of 1 m/s.

Ambipolar electric fields at Mars have been shown to cause enhanced loss of $O_2^+$ (Ergun et al., 2016). These ions are drawn from below the exobase by the loss of electrons due to enhanced solar wind heating, creating an E-field that drags ions out of the ionosphere, and have been similarly observed at Venus (Collinson et al., 2016). Typically these ions are affected down to 160 km, so it is plausible that metallic species undergo mass separation below this, and then are mixed above. Our observations are spatially coarse, such that we cannot make a statement here about separate scale heights. While ambipolar electric fields shown by Ergun et al. (2016) should be strong enough to lift $Mg^+$, which is 75% as massive as $O_2^+$, without appropriate modeling it is not immediately clear that ambipolar electric fields would be strong enough to affect $Fe^+$ whose mass is 175% that of $O_2^+$.

### 3.3.5 Enhanced Loss of Metallic Species

Discrepancies between the observed total metallic abundance compared to those predicted by CABMOD (Section 3.2.3) highlight important physical and chemical processes that demand further investigation (Figure 3.6). We characterize the observed total metallic

abundance for each species by summing each metallic species between 90 and 180 km, and across the periapse segment to give a general metric of the abundance of metallic species while smoothing the effects of horizontally or vertically disjoint profiles (Section 3.3.6).

CABMOD is run for quiescent Mars until steady state is reached, after which a meteoric perturbation is applied and we track the relaxation of the model for comparisons with observations. It is run for daytime low-latitude conditions, and as a 1D model does not include diurnal variations. This model does not apply to the unexposed hemisphere, so we approximate horizontal transport by reducing the model after orbit 117 by a factor of two (equivalent to distributing the deposited material over the entire planet).

The total metallic abundance observed is less than predicted after orbit 117, indicating the rapid disappearance of metallic species compared to the current modeled processes. There may be a chemical process affecting both the Fe and Mg chemistry branches simultaneously, however a dynamical loss process that affects all metallic species may be more likely. As ions are sourced from neutrals near 100-120 km, if ions are being removed at the exobase at rates larger than predicted, this effectively depletes neutrals as well. The presence of ions at high altitude in orbit 117 (Figure 3.3) suggests this may be occurring.

Ions transported by either Lorenz force or ambipolar electric fields end in two populations dependent on their initial vertical motion. Ions moving downward will neutralize and undergo appropriate metallic chemistry that either re-ionizes them or removes them to a stable sink. Ions drifting upward stay ionized and have lifetimes that increase with increasing altitude, and may therefore leave the atmosphere much more rapidly than predicted by diffusion alone. While these ions would not have sufficient kinetic energy to escape thermally, they may be able to travel along open field lines into the magneto-tail as seen at Earth and Saturn (Christon et al., 2015, 2017) or through one of several ion outflow mechanisms seen at Mars (Brain et al., 2015).

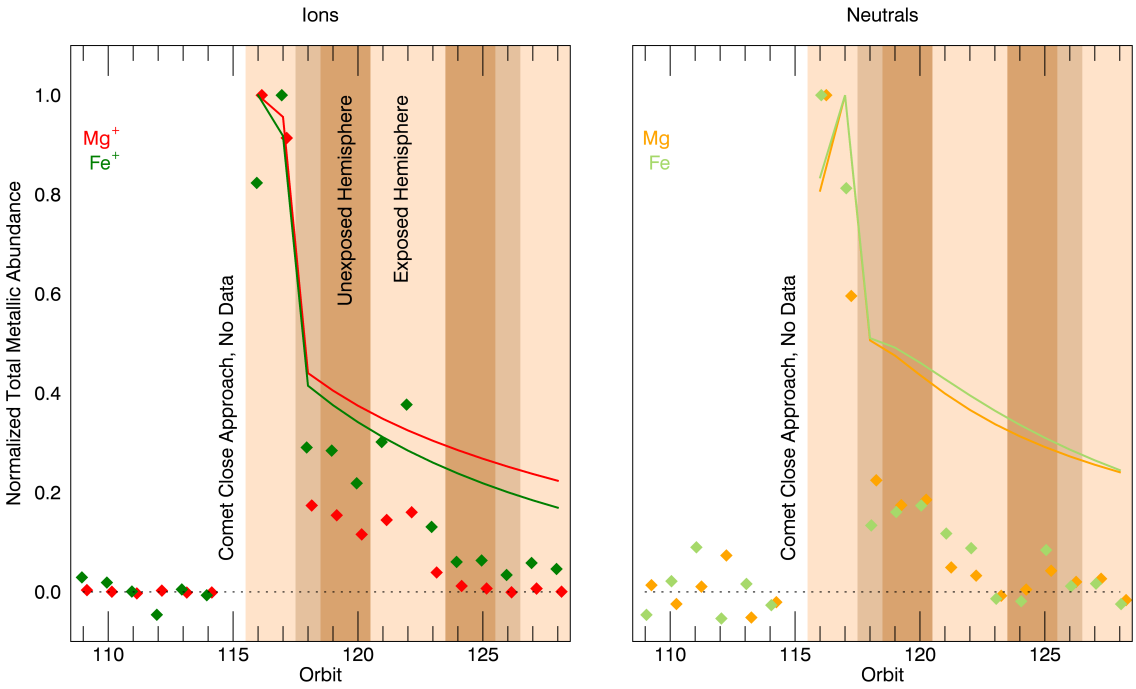


Figure 3.6: The total metallic content ($cm^{-3}$) between 90 and 180 km for each orbit is shown with diamonds, normalized to the maximum for each species (ions on the left, neutrals on the right). Orbits before the close encounter with comet Siding Spring (orbit 115) show the background level and scatter of observations, the latter is due primarily to the relative scattering efficiency of each species (see Table 3.1).

### 3.3.6 Detached Layers and Strong Gradients

Figure 3.7 shows coherent structures and gradients that require further study. Deposition is expected to occur uniformly on the exposed hemisphere, and diffusion and transport should be smoothing processes over these spatial scales. However, in orbits 118 and 120, we see $Mg^+$ forms a distinct layer in the middle scans that is not directly connected to the $Mg^+$ in the beginning of those scans. This feature appears to be evident in the $Fe^+$ as well, although clearer in orbit 118 than 120. These ion layers occur at altitudes that are higher than deposition permits, indicating this transport must be coherent on a spatial scales over 1000 km horizontally.

As noted by Schneider et al. (2015b) and visible in Figure 3.6, there is an increase in $Fe^+$, $Mg^+$, and Mg in orbits 121 and 122 compared to the observed declining trend. This is due to an unexplained set of strong enhancements in scans 1 and 6 from each orbit, respectively (Figure 3.7). Moreover, the total amount of $Mg^+$ does not change significantly between orbits 118 and 122, yet the bulk of the ions are contained in the first 6 scans of orbit 122. The horizontal gradient in $Mg^+$ by a factor of 7 within two scans of orbit 122 is not readily explained, and this strong gradient requires a mechanism not determined herein.

The geographic regions of these orbits are on the exposed hemisphere and may suggest a local phenomenon where metallic species are confined within a small geographic in a manner inconsistent with expected diffusion or standard transport. Similar confinement has been suggested for transient metallic layers above the ablation region (Grebowsky et al., 2017), however no mechanism has yet been described. Three-dimensional modeling may be necessary to determine whether these ions become trapped in circulation patterns, are influenced by remnant crustal magnetization, or some other effect.

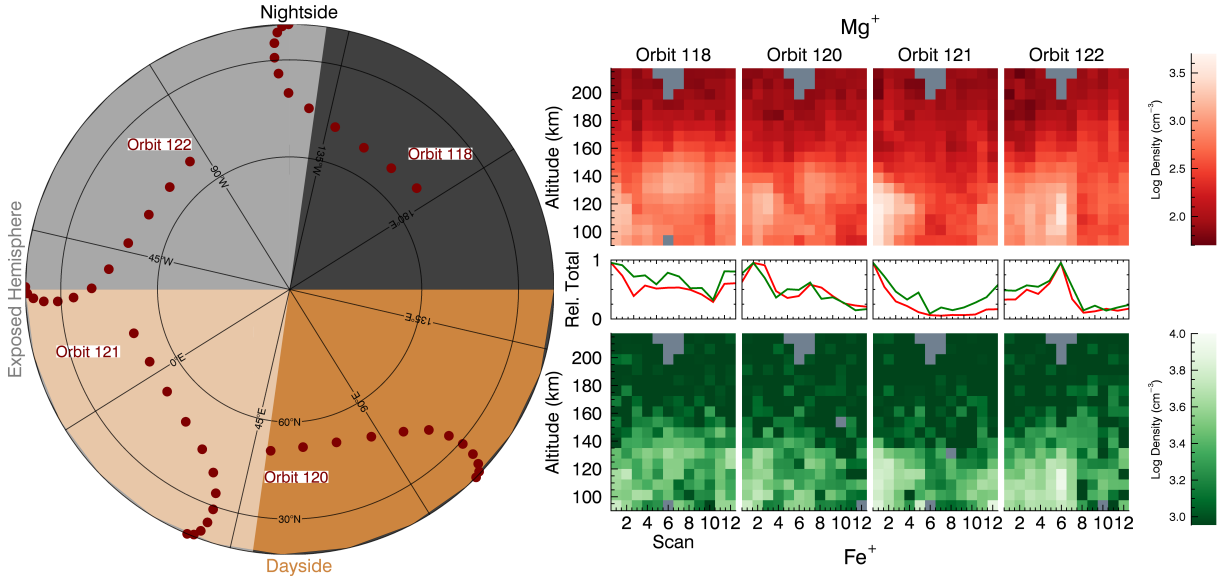


Figure 3.7: **(Left)** As in Figure 3.2, a geographical representation of observed regions of Mars at the predicted time of dust deposition, where the tangent points of orbits 118, 120, 121, and 122 are shown with maroon circles, with scans beginning at high latitudes and ending near the equator. **(Right)** Orbit by orbit images of $Mg^+$ and $Fe^+$ (top and bottom) constructed by co-adding spectra by altitude (shown on the vertical axis), and adjacent scans are shown on the horizontal axis, which spans 1000 km. Line plots ($Mg^+$ = red, $Fe^+$ = green) in the center of the images indicate the total metallic content between 90 and 180 km normalized to each orbit. Measurements before the comet's passage (shown for $Mg^+$ in Figure 3.2) are consistent with the persistent layer of $Mg^+$ and no observable $Fe^+$ in the atmosphere.

### 3.3.7 Revisiting Meteor Shower Predictions

The vertical profiles of Mg, $Fe^+$, and Fe complement the $Mg^+$ profiles of Schneider et al. (2015b) and this analysis allows an opportunity to reduce the uncertainty on their reported dust flux. Their work carried a range of reported $Mg^+$ densities that implied a dust deposition mass bracketed between 2700 and 16000 tonnes. The updated calibration yields a delivered mass inferred by the $Mg^+$ measurements of 16000 $\pm$ 4500 tonnes.

There is a significant discrepancy between the observed (Schneider et al., 2015b) and predicted (Kelley et al., 2014) dust deposition that may be related to dust size. The modeled dust was in the size range 0.7 - 3.6 mm, which were ejected from the comet no more than 1.5 years before the encounter. However, the shape and altitude of the observed ablation region suggest that most of the impacting particles were in the size range 1 - 100 microns. As radiation pressure rapidly sweeps away smaller particles, it is expected that the impacting grains were younger than the 1.5-year-old modeled grains and therefore would be more sensitive to cometary activity before the encounter. While the relationship between dust delivery and cometary activity is not necessarily linear, the modeled water production rate of 4 x $10^{27}$ $H_2O$/sec (Kelley et al., 2014), is smaller than the observed 1.2 x $10^{28}$ $H_2O$/sec (Crismani et al., 2015) by a factor of three. Moreover as observations were limited by the lack of multiple observation epochs (Siding Spring is a dynamically new Oort cloud comet), some cometary parameters (such as grain ejection velocity) may not be well constrained.

## 3.4 Conclusions

Observations in the aftermath of comet Siding Spring's meteor shower provide a unique opportunity to observe the response of the Martian atmosphere and ionosphere to a significant perturbation. This time period provides constraints on metallic species that would otherwise be undetectable with current instruments, and may shed light on new dynamics or the chemistry that affects them.

Using the spatial distribution of $Mg^+$ around the planet, we determine that Mars passed through the debris stream of comet Siding Spring in no more than 3 hours. Dust from comet Siding Spring was deposited in a narrow vertical layer, as seen in all metallic species observed by IUVS. Horizontal winds then distribute this material globally within 9 hours, and requires horizontal winds speeds at 120-150 km to the range of 180-240 m/s. Neutral Mg appears to be rapidly destroyed or lost on the dayside, where it becomes reduced by 75% within 8 hours, faster than current model predictions, suggesting an incomplete understanding of the processes that affect it.

Vertical transport of metallic ions is implied by the observations but unexplained by current 1D models, as inferred from presence of enhanced densities at high altitude. This transport is more rapid than diffusion, coherent over 1000 km horizontally, and may be related to electrodynamic effects. The presence of several other unexpected phenomena provides a potential case study for 3D modeling efforts to determine how these anomalous structures and features are formed, and whether the presence of crustal magnetic fields has any affect.

We use this work to revisit meteor shower dust predictions where there is significant discrepancy compared to observations. The shape and altitude of the ablated layer suggests that particles that impacted Mars were smaller than modeled, and therefore more sensitive to the water production rate before the encounter. The relationship between cometary activity and delivered dust mass is not necessarily linear, and we can therefore begin to understand this self-consistently by noting the observed water production rate was three times larger than predictions.

# Chapter 4

# Persistent Meteoric Layer

## 4.1 Introduction

High-speed collisions with air molecules cause rapid heating of interplanetary dust particles, melting and evaporating their constituent minerals (Istomin, 1963; Anderson and Barth, 1971). This ablation process deposits a variety of atomic constituents at the 1 $\mu$bar level (80-110 km on Earth). Non-volatile elements such as Mg, Fe, and Si act as direct tracers of the ablation process, as no other processes transport these species to these altitudes. These elements are in approximate equilibrium between supply through ablation and loss by chemical reactions forming oxides, hydroxides, and carbonates, which subsequently polymerize into particles called meteoric smoke (Nachbar et al., 2016). Meteoric smoke particles mostly likely provide condensation nuclei for high altitude $CO_2$ ice clouds at Mars. In addition to the quasi-steady-state supply from random (or "sporadic) meteors, the ablation of cometary dust during meteor showers can supply additional metals to the upper atmosphere.

The Mars Atmosphere and Volatile EvolutioN (MAVEN) mission (Jakosky et al., 2015b) was designed to study the response of Mars' upper atmosphere to solar influences (Jakosky et al., 2015a), however it is coincidentally well equipped to detect the influence of interplanetary dust particles (IDPs). This capability was clearly demonstrated during the exceptionally close encounter of comet C/2013 A1 (Siding Spring) with Mars and the ensuing meteor shower (Gurnett et al., 2015; Restano et al., 2015; Benna et al., 2015). Of the many elements that ablate from interplanetary dust particles, $Mg^+$ and Mg are most

readily detectable in ultraviolet (UV) remote sensing, and were observed in a transient layer for comet Siding Spring (Schneider et al., 2015b). Here we report on Imaging Ultraviolet Spectrograph (IUVS) observations of $Mg^+$ over the course of MAVENs two-year mission that are consistent with a persistent meteoric layer.

## 4.2 Observation and Data Analysis

### 4.2.1 Spectral Analysis and Vertical Profiles

Emission from $Mg^+$ was reliably detected in every periapse scan obtained over one Mars year (two Earth years; Figure 4.1 and Figure 4.3) whenever the $Mg^+$ layer was appropriately illuminated and the instrument orientation did not introduce excessive scattered solar continuum (for these purposes, stray light). The $Mg^+$ emission feature, centered on 280 nm, is due to resonant scattering of solar UV photons rather than direct excitation during ablation. $Mg^+$ brightnesses were extracted from a model spectrum fit (Figure 4.1), using line positions and atomic constants of known emitters in this spectral region plus a stray light solar spectrum (Stevens et al., 2015; Jain et al., 2015; Dymond et al., 2003).

Stray solar continuum enters the instrument in two ways, through the nadir and limb port, and their spectral characteristics are very similar (see Section 1.5.4 and Figure 1.18). When viewing in limb geometry, scans where the tangent point is at high altitude show a signature of stray light, which we believe comes from disk-reflected light through the open nadir port. As the tangent point moves toward the surface, the baffle edges of the instrument (see Figure 1.11) move toward lower altitudes as well, and scattered light from the limb is able to enter the limb port. Confidence in the spectral shape of reflected solar continuum is the primary impediment to observing $Mg^+$ low in the atmosphere, as the solar absorption feature is aligned with the Martian emission feature, and when the former becomes bright, its Poisson noise is too large to reliably extract a retrieval of the $Mg^+$ emission (whose brightest emission is not more than a few kR).

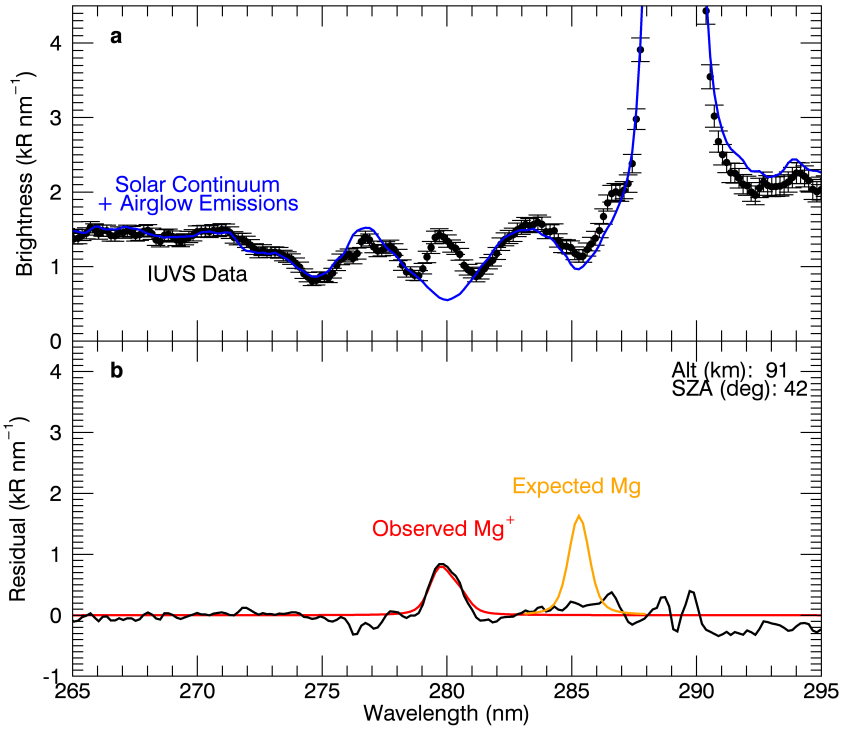


Figure 4.1: This representative scan was taken near noon (10-15 hours local time) in the Northern hemisphere (50-70 N) on 4/22/16 (orbit 3040). **a** The MUV spectrum is slit averaged and 1-sigma errorbars are propagated from the Poisson noise of the data. The data are shown as black circles, with known airglow emissions (see text) fit in blue. **b** The residual (black line) from **a**, with an emission near 280 nm consistent with $Mg^+$ (red) whose brightness is 1.81±0.13 kR. Atomic Mg has an emission feature at 285 nm whose predicted brightness (orange) is not detected.

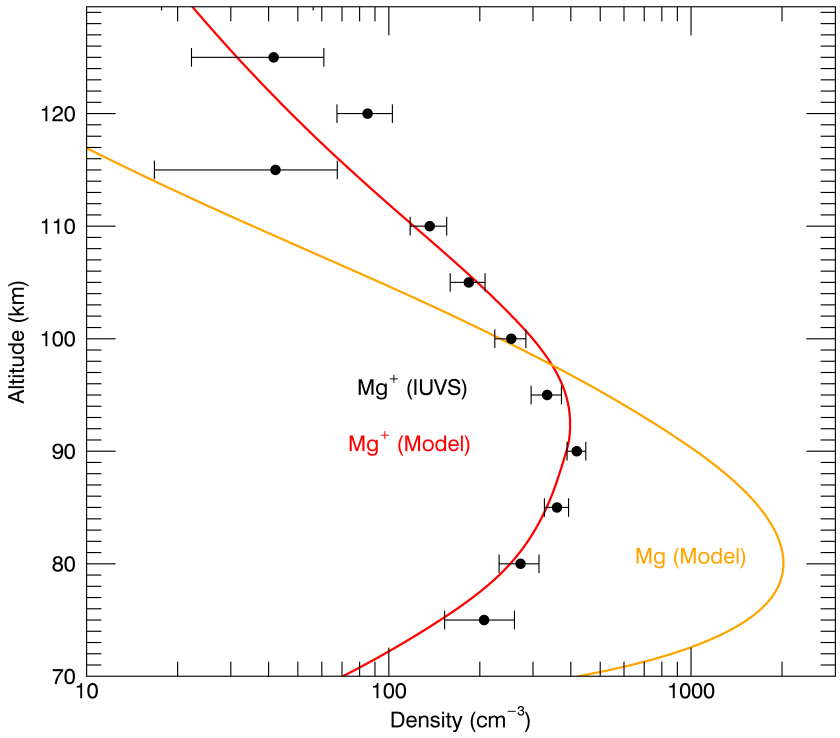


Figure 4.2: IUVS derived $Mg^+$ altitude profiles, averaged from orbit 3040, compared with the baseline CABMOD prediction. The predicted brightness is derived from the model density using the atomic Mg scattering efficiency (Barth et al., 1971b), indicating that Mg is not detected despite large predicted concentrations.

The $Mg^+$ emission brightness was converted to local ion density through an Abel transform, common in the study of optically thin airglow emissions (Chamberlain and Hunten, 1987). To determine the density at the tangent point, we used an Abel transform method (Chamberlain and Hunten, 1987), considering the emission to be optically thin and with an spherically symmetric observing geometry. Using the standard relationship for the scattering cross section, related to the oscillator strength and Doppler width (Risberg, 1955), we find the $Mg^+$ doublet (at 140 K) cross section is 8.9 and 4.4 x $10^{-12}$ $cm^2$. Therefore we do not expect self-scattering to become important until densities at the tangent point approach $10^4$ $cm^{-3}$, and the mean free path length is reduced to 100 km. As the retrieved densities are never larger than $10^3$ $cm^{-3}$, we consider this emission optically thin, thus the Abel transform is a robust approximation to the density at the tangent point.

The g-factors (Equation 1.9) for the $Mg^+$ lines at 279.5528 and 280.2705 nm used herein are 10.05 x $10^{-2}$ $s^{-1}$ and 4.64 x $10^{-2}$ $s^{-1}$ respectively. Dymond et al. (2003) calculated 8.4 x $10^{-2}$ $s^{-1}$ and 3.9 x $10^{-2}$ $s^{-1}$, while Barth et al. (1971b) calculated 9.1 x $10^{-2}$ $s^{-1}$ and 3.7 x $10^{-2}$ $s^{-1}$. Although Dymond et al. (2003) cites their use of a higher resolution solar spectrum from Ahearn et al. (1983), the spectrum found therein is actually not higher resolution, and a personally communicated spectrum from Hearn et al. (1983), which we used, may be instead what they were referencing. In this spectrum, the flux at 1 AU is 2.5 and 2.2 x $10^{12}$ for 279.6 and 280.3 nm respectively. For the Mg line, we use the g-factor of Barth et al. (1971b).

### 4.2.2 Observations of $Mg^+$

Observations of $Mg^+$ are limited at high and low altitudes by signal to noise of the emission. At high altitudes, the $Mg^+$ signal has decreased to levels that are lower than reliably retrievable from the IUVS sensitivity. At low altitudes, reflected solar spectrum dominates the signal, such that $Mg^+$ becomes comparable to the Poisson noise from the $Mg^+$ solar absorption feature.

The $Mg^+$ layer has a mean peak concentration of 250 $cm^{-3}$ and is typically found near

an altitude of 90 km (e.g. Figure 4.2). Reported altitudes carry a 2.5 km uncertainty consistent with slit averaging in 5 km bins (Stevens et al., 2017). Figure 4.3 shows the derived densities in a fixed altitude range over the course of the mission. Brightness measurements carry Poisson random uncertainties propagated through a multiple linear regression technique and Abel transform. The random uncertainties propagate linearly into densities and other derived quantities.

Observations of $Mg^+$ density demonstrate real variability (Figure 4.3) beyond the random uncertainties. Observations of $Mg^+$ are not uniform from scan to scan or at a single altitude. As demonstrated in the Siding Spring era 3.3.6, uniform deposition does not necessarily result in a spatially uniform layer. Moreover, the presence of detached layers or transport mechanisms that elude explanation suggest that the layer is not a quiescent object and statistical properties should be preferentially used. The lower atmosphere of Mars also warms and cools seasonally and in response to dust storms, moving the ablation layer up and down relative to the fixed altitude range used here (Jakosky et al., 2017).

We observe an unexpected diurnal variation in the $Mg^+$ density; decreasing by up to factor of five towards the dawn and dusk terminators. This effect is most pronounced near the equator and less noticeable near the poles where the diurnal cycle is decreased in intensity. This diurnal pattern either indicates that ablation is not geographically uniform or there is an unknown sink for $Mg^+$ near the terminators.

## 4.3 Analysis and Results

### 4.3.1 Lack of Mg

Emission from atomic Mg has only been reliably detected (Figure 4.1) during the exceptionally intense meteor shower of comet Siding Spring (Schneider et al., 2015b). Scaling $Mg^+$ by the ratio of the Mg and $Mg^+$ scattering efficiencies at our most marginal detection, we find that IUVS would have detected atomic Mg at concentrations greater than 130 $cm^{-3}$,

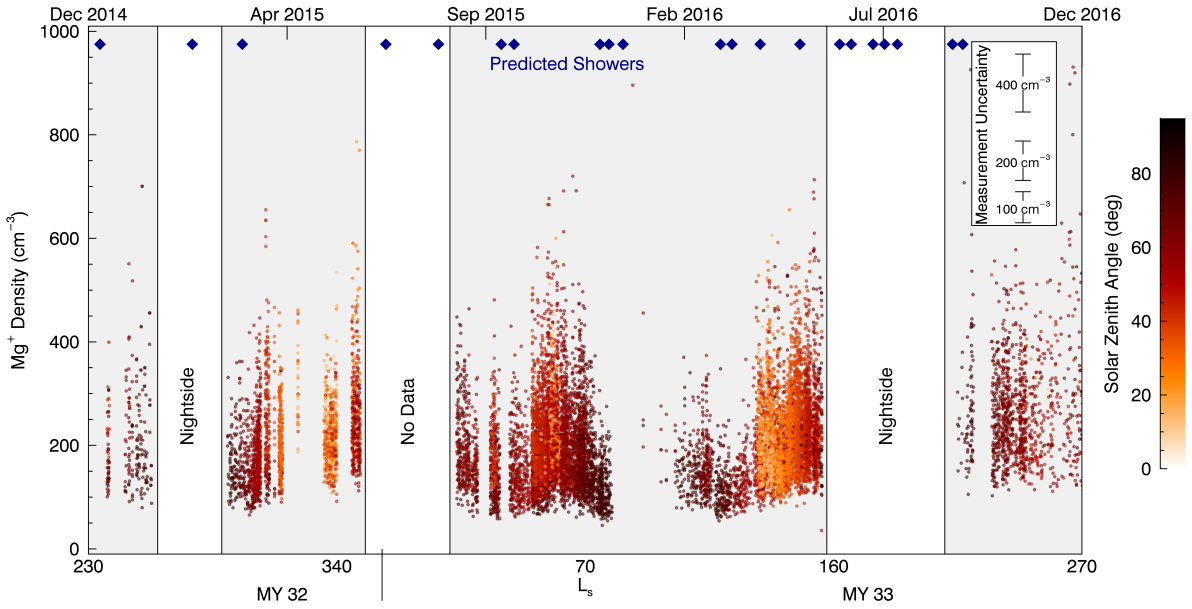


Figure 4.3: $Mg^+$ concentrations between 90-100 km over the course of two Earth years. The timeline omits the comet Siding Spring meteor shower of October 19th 2014, as the peak density of $\sim 10^5$ is off-scale. Average measurement uncertainties are given for three densities in the legend. Observations taken at high solar zenith angle (darker colors, >70 deg) demonstrate marked reduction in $Mg^+$, consistent with decreases toward the dawn and dusk terminators, especially near the equator. As observations sample a range of latitudes, these observations represent a variety of local time and latitude coverage. Blue diamonds indicate predicted meteor showers

based on our present understanding of ablation and atmospheric chemistry (Figure 4.4).

The apparent absence of neutral Mg therefore poses a significant challenge to our understanding of the chemical reactions that create and connect Mg and $Mg^+$. Laboratory studies validated by terrestrial observations (Nachbar et al., 2016) have been incorporated in the Chemical ABlation MODel (CABMOD) (Whalley and Plane, 2010; Vondrak et al., 2008) which describes the ablation physics and chemistry, and is coupled to a 1-D atmospheric model which tracks subsequent atmospheric chemistry. When adapted for conditions at Mars, CABMOD predicts that Mg atoms would be injected directly during ablation and should build a neutral Mg layer below 100 km. $Mg^+$ would then be produced through charge exchange with ambient $O_2^+$ (Molina-Cuberos et al., 2003). Atomic Mg would also undergo a series of reactions to create a steady-state population of $MgCO_3$ (Figure 4.4). Together these reactions are expected to yield an $Mg/Mg^+$ ratio of  4 at 90 km, contrary to the observed upper limit of  0.5. Furthermore, at 90 km $Mg^+$ should have a lifetime comparable to a Mars day (Whalley and Plane, 2010) and should therefore exhibit negligible diurnal variation.

Alternative chemical pathways were investigated to explore the relationship between Mg and $Mg^+$. Dissociative recombination of $MgCO_3^+$ with electrons is assumed to have two reaction channels:

$$\begin{aligned} MgCO_3^+ + e^- \rightarrow & MgO + CO_2[\alpha] \\ & Mg + O + CO_2[1-\alpha] \end{aligned} \tag{4.1}$$

where $\alpha$ is the branching ratio. If this reaction yields MgO rather than Mg, then the Mg layer would remain below the IUVS detection limit (Figure 4.5). CABMOD was altered to test the effect of varying $\alpha$ on the modeled Mg layers, with a value of $\alpha = 1$ more consistent with observations. Additional laboratory studies are needed to accurately determine the branching ratio, and whether additional unknown chemistry plays a role. None of the alternative chemical reactions we explored can yet explain the strong diurnal variation in $Mg^+$.

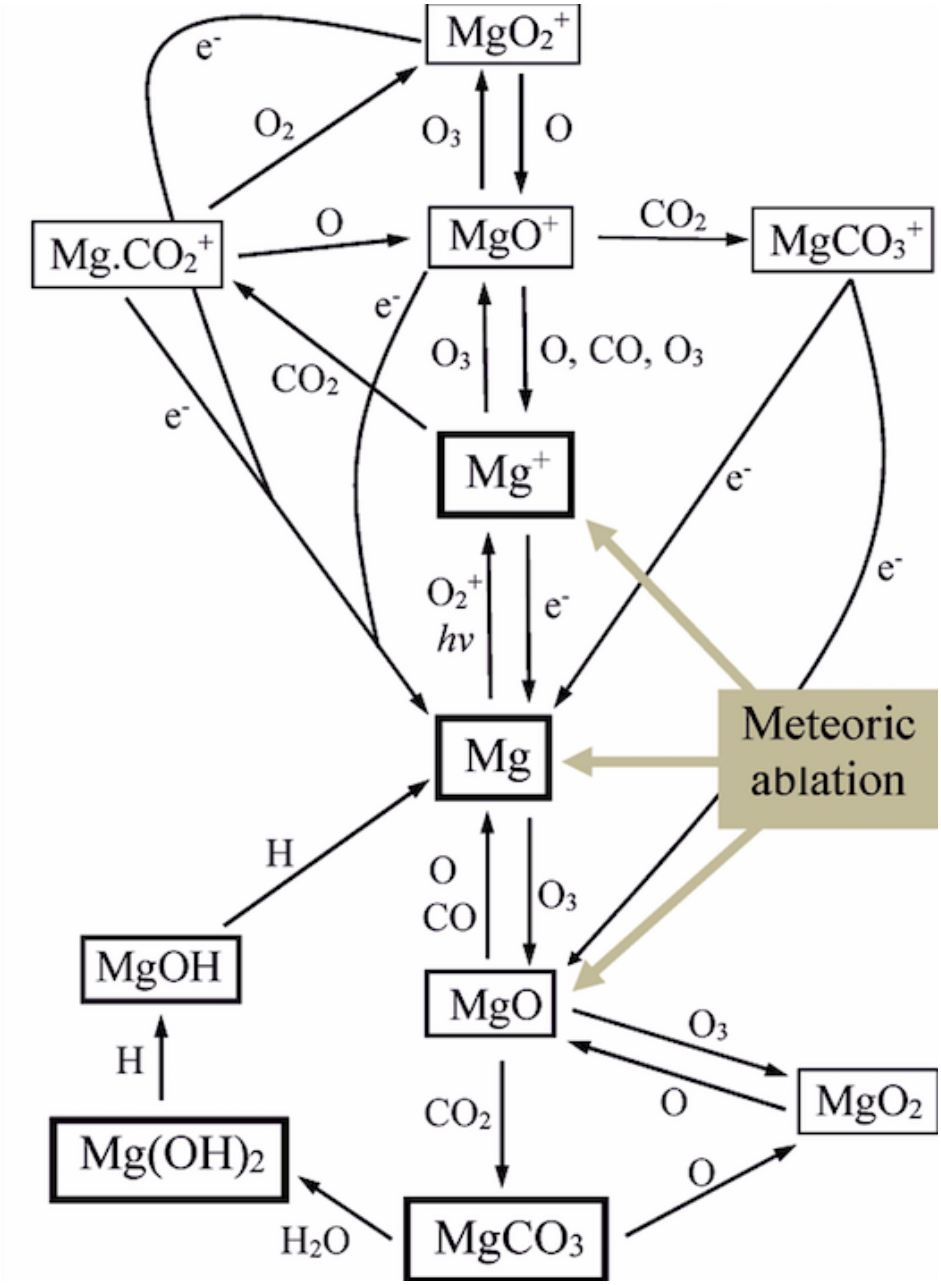


Figure 4.4: Schematic of our current understanding of meteoric Mg chemistry in the $CO_2$ dominant atmosphere of Mars. Image Credit: J. Plane

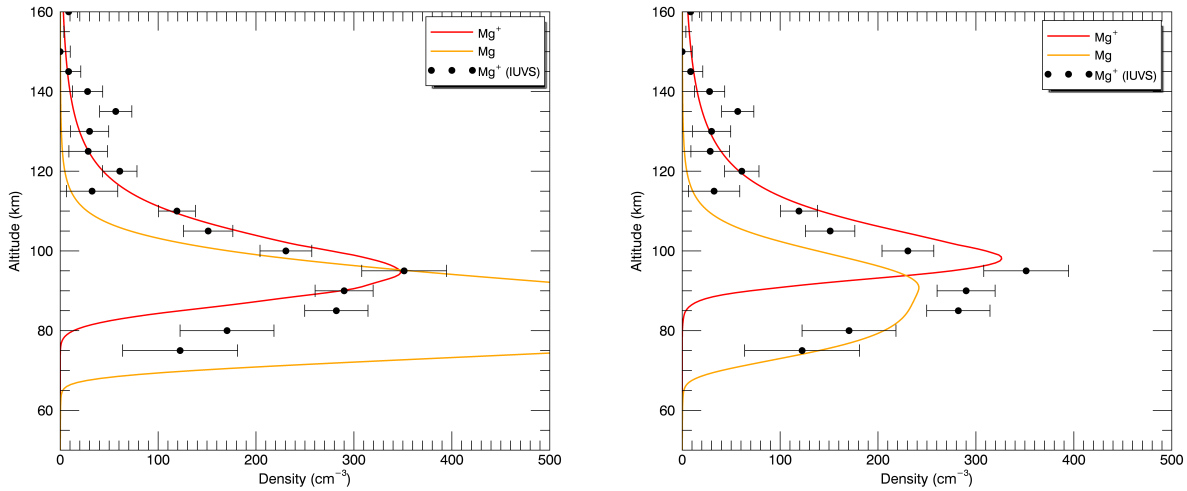


Figure 4.5: Comparison of chemical models to explain the lack of observed Mg. Vertical profiles of the modeled $Mg^+$, Mg and $Mg(OH)_2$ concentration profiles, compared to the IUVS average $Mg^+$ profile from Figure 4.2. **(Left)** For this model run the dissociative recombination of the $MgCO_3^+$ ion is assumed to produce 1% Mg and 99% MgO. **(Right)** For this model run the dissociative recombination of the $MgCO_3^+$ ion is assumed to produce MgO only.

### 4.3.2 Interplanetary Dust Flux

The IUVS measurements can be used to provide the first remote sensing estimate of interplanetary dust particle flux at a planet other than Earth. At Earth, the observed metal layer is supplied from the main IDP sources  Jupiter Family Comets, asteroids, and long-period comets (Halley Type and Oort Cloud) with particle mass ranging from $10^{-4}$ and $10^{-7}$ g, and a global input of 29 - 57 tonnes $d^{-1}$ (CarrilloSánchez et al., 2015). We do not expect Mars metal layer to be sourced from a different population, and these observations directly constrain the largest IDP population by mass (excluding surface impactors), making a direct measurement essential for an accurate estimate.

Mars' global dust input was estimated using representative profiles with local times near noon and where the peak and underside of the layer were clearly detectable. In the baseline chemical model (Whalley and Plane, 2010), which neglects the absence of observed Mg, we find a global dust input rate of  2 tonnes $sol^{-1}$; in the alternate model this value is 3 tonnes $sol^{-1}$. Note that uncertainties in the $MgCO_3^+$ chemistry render the 2 tonnes $sol^{-1}$ a lower limit, as alternative reactions to reduce the abundance of Mg also reduce the efficiency for creating $Mg^+$. The instruments systematic and observational uncertainties are small in comparison to this range in estimates, and therefore omitted from this result. Comparing the dust environment at Mars to Earth, and accounting for their difference in surface area, we find the fluence at Mars of 2 - 3 tonnes $sol^{-1}$ is at the lower end of the measurements scaled from Earth (Plane, 2012), 1.4 - 14 tonnes $d^{-1}$.

As at Earth, these Mars fluences can be compared to space-borne dust detectors. The MAVEN Langmuir Probe and Waves (LPW) instrument measured high altitude dust particles between $10^{-11}$-$10^{-7}$ g and determined a fluence of these particles to be between 85 kg $d^{-1}$ and 8.5 tonnes $d^{-1}$ (Andersson et al., 2015b). Their extrapolation to the total input is necessarily imprecise due to the small masses sampled, which is not representative of the mass of IDPs that ablate and inject metals into the atmosphere. The NGIMS instrument

on MAVEN can also sample ablated metals (Grebowsky et al., 2017), though the region sampled lies several scale heights above the main deposition layer such that global fluence may not be possible to estimate.

### 4.3.3 Lack of Transient Enhancements

Mars likely encounters regular meteor showers, analogous to Earth; however, we have been unable to detect any showers other than comet Siding Spring (Schneider et al., 2015b), which produced $Mg^+$ concentrations at 120 km of 3 x $10^4$ $cm^{-3}$. During the 24 predicted Mars meteor showers between MAVEN's arrival at Mars and December 2016, IUVS can constrain 11 of these events when it was observing in daylight and taking data. The $Mg^+$ profiles at these times show no correlated increases greater than 500 $cm^{-3}$ (twice the mean), constraining the fluence of these showers to levels lower than the nominal global input of 3 tonnes $sol^{-1}$. Thus, the two-year timeline of meteoric metal layer observations reported here demonstrate that meteor showers at Mars do not significantly perturb the metal ion abundances.

As observations of parent bodies grow, more and more meteor streams are theoretically determined, yet there is a lack of constraints on Mars' crossing streams. Specifically, there are no constraints about the fluence of particles, the size of the stream (and thus the length of the shower), or particle size (which determines ablation height and stream density). Therefore, future work will be necessary to catalog all predicted meteor events, and provide upper limits to their deposition rates. This effort requires the variability of the $Mg^+$ layer to be understood, including the diurnal variation, unusual gradients seen in comet Siding Spring's aftermath and variation from orbit to orbit.

The observation timeline (Figure 4.3) also argues strongly against a meteoric origin for transient ionospheric layers (the M3 layer) detected in radio occultation measurements (Pätzold et al., 2005; Withers et al., 2008). The M3 layer was detected in 1 - 10% of observations, with electron concentrations of $10^4$ $cm^{-3}$. Although a meteoric origin was

proposed, the nature of these electron concentrations is ambiguous because the M3 layer may be due to either an enhancement of meteoric (e.g. $Mg^+$, the dominant ion from ablation) or ambient ($O_2^+$, $CO_2^+$ etc.) ions. IUVS observations are performed in a similar geometry to radio occultations, and occur every ∼4.5 hrs. Therefore, if the source of the M3 layer was metallic ions in concentrations approaching $10^4$ $cm^{-3}$, the layer would be readily observed in 130-1300 profiles (Figure 4.3), whereas IUVS has not detected any $Mg^+$ densities larger than $10^3$ $cm^{-3}$ at any altitude outside of the comet Siding Spring epoch. Another origin, such as enhanced solar energetic particle precipitation or x-ray flux, may be responsible for the transient M3 layer.

## 4.4 Conclusions

Interplanetary dust particles sporadically enter planetary atmospheres at orbital velocities and ablate as collisions occur with ambient gases to produce a persistent layer of metallic atoms (for example, Fe, Mg, Na) in their upper atmospheres. Such layers are well studied at Earth, but have not been directly detected elsewhere in the Solar System. We have reported here on the detection of a meteoric layer consisting of $Mg^+$ ions near an altitude of 90 km in the Martian atmosphere from ultraviolet remote sensing observations by NASA's MAVEN spacecraft.

We observe temporal variability in the $Mg^+$ layer over the course of a Martian year, moving up and down in altitude seasonally and in response to dust storms, and displaying diurnal fluctuations in density. Emission from $Mg^+$ was reliably detected in every periapse scan obtained over one Mars year (two Earth years) whenever the $Mg^+$ layer was appropriately illuminated and the instrument orientation did not introduce excessive scattered solar continuum. The $Mg^+$ layer has a mean peak concentration of 250 $cm^{-3}$ and is typically found near an altitude of 90 km.

We also find that most meteor showers do not significantly perturb this layer, which constrains the fluence of eleven observed Martian meteor showers to less than our estimated

global dust flux. Mars likely encounters regular meteor showers, however, we have been unable to detect any showers other than comet Siding Spring. Future work will be necessary to constrain the dust contribution of predicted Mars meteor showers.

The persistence and variability of the $Mg^+$ layer are difficult to explain with existing models and reconcile with other transient layers of ions observed in the Martian ionosphere. Emission from atomic Mg has only been reliably detected during the exceptionally intense meteor shower of comet Siding Spring. The apparent absence of neutral Mg therefore poses a significant challenge to our understanding of the chemical reactions that create and connect Mg and $Mg^+$, therefore alternative chemical pathways were investigated to explore their relationship. We suggest that transient ionospheric layers are not sourced from the persistent $Mg^+$ layer and thus not derived from meteoric material, but are ambient ions produced by some unknown mechanism.

# Chapter 5

# Conclusions

## 5.1 Summary of Results

This thesis details the unique encounter of comet Siding Spring, and reveals the presence of a "persistent layer" from sporadic meteors at Mars. We summarize these results below, and in Section 5.2 detail how measurements of the persistent layer makes the prospect of methane generation by meteor showers unlikely, published as Crismani et al. (2017a). In Section 5.3 we expand upon the implications of Crismani et al. (2017b) to argue that previously observed transient ionospheric layers cannot be meteoric in origin. Finally, we highlight the major topics of research that should be considered in the future of meteoric science at Mars.

### 5.1.1 Cometary gas delivered to Mars

Before the encounter of comet Siding Spring with Mars, we used IUVS to image the comet's hydrogen coma, published as Crismani et al. (2015). The hydrogen coma is created by the dissociation of water liberated from its surface and subsurface, and observations of hydrogen serve as an available proxy for water (which lacks emission features in the ultraviolet). By fitting observed radial profiles to predictions from a robust cometary model we were able to infer a water production rate of $1.1 \pm 0.5 \times 10^{28}$ molecules/s. The spatial information from these hydrogen images feature the location that Mars would encounter, and represent the most temporally similar observations of the activity during the close encounter.

From this water production rate, we were able to determine the total mass of gaseous material that impacted Mars. It is necessary to infer this from coma observations, as these species are present in Mars' atmosphere as well. We use inferred impacting gaseous masses to revisit and reconcile predictions of the atmospheric response, finding agreement that the oxygen perturbation is negligible, prompting further work in the determination of a carbon perturbation, and determining the hydrogen perturbation would be unobservable in the IUVS data.

The prediction of a thermospheric response due to energy deposition in the upper atmosphere is mostly unchallenged by these findings. However we propose that such a perturbation should exist at higher altitudes due to the difference between observed and predicted atmospheric temperatures above 150 km. Determining this thermospheric response from the data will be problematic, due to the lack of in situ instruments at those altitudes and as the atmosphere has demonstrated variability on spatial and temporal scales that may exceed this thermospheric perturbation.

### 5.1.2 Cometary dust perturbed Mars atmosphere

Observations of the atmosphere of Mars in the aftermath of comet Siding Spring's meteor shower provide a unique opportunity unlikely to be duplicated in modern times. MAVEN was serendipitously positioned to observe the response of the Martian atmosphere and ionosphere to this significant perturbation, and we use this event to provide constraints on metallic species that would otherwise be undetectable with current instruments. These observations may also shed light on new ionospheric dynamics and meteoric chemistry. This work is currently in preparation for submission.

Using the spatial distribution of $Mg^+$ around Mars, we determine that it passed through the debris stream of comet Siding Spring in no more than 3 hours. The common altitude of all metallic species observed by IUVS suggest dust from comet Siding Spring was deposited in a narrow vertical layer. Horizontal winds then distribute this material globally and require

horizontal winds speeds at 120-150 km to the range of 180-240 m/s. Neutral Mg appears to be rapidly destroyed or lost on the dayside, where it becomes reduced by 75% within 8 hours, faster than current model predictions, suggesting an incomplete understanding of the processes that affect it.

Vertical transport of metallic ions as inferred from presence of enhanced densities at high altitude is unexplained by current 1D models. This transport is more rapid than diffusion, coherent over 1000 km horizontally, and may be related to electrodynamic effects. The presence of this and several other unexpected phenomena provides a potential case study for 3D modeling efforts to determine how these anomalous structures and features are formed.

We use this work to revisit meteor shower dust predictions where there is significant discrepancy compared to observations. The shape and altitude of the observed ablation layer suggests that particles that impacted Mars were smaller than modeled, and therefore younger and more sensitive to the cometary water production rate before the encounter. The relationship between cometary activity and delivered dust mass is not necessarily linear, and we can begin to understand this self-consistently by noting the observed water production rate was three times larger than predictions. Modeling of this comet's debris stream and dust coma should be undertaken to determine whether there are any outstanding issues with comet dust models.

### 5.1.3 Sporadic meteors creates a persistent layer at Mars

Meteoric ablation from comet Siding Spring prompted a deeper analysis into the presence of sporadic meteors. Emission from $Mg^+$ was reliably detected over one Mars year whenever observation conditions were favorable, suggesting that sporadic meteors create a persistent metallic ionospheric layer. It is necessary to determine mean characteristics of the $Mg^+$ layer, as it demonstrates real variability beyond the random uncertainties associated with a varying ablation altitude and unexplained diurnal variation.

Outside of the comet Siding Spring era, over more than two Earth years of observations, we have not observed neutral Mg, meteor showers, or significant enhancements to the $Mg^+$ layer. The apparent absence of neutral Mg therefore poses a significant challenge to our understanding of the chemical reactions that create and connect Mg and $Mg^+$ and alternative chemical pathways were investigated to explore their relationship.

The lack of other observed Martian meteor showers suggests that delivered mass from these showers is negligible compared to the persistent layer. Further work will be necessary to determine what upper limits may be set for the dust fluences from these events.

The lack of enhancements in the $Mg^+$ layer suggest that previously observed transient ionospheric layers cannot be meteoric in origin. We expand this point in Section 5.3 and this paper will be submitted with the inclusion of MAVEN's radio occultation results after that experiment's "first results" publication.

## 5.2 Meteoric Origin of Mars Atmospheric Methane is Implausible

Reports of transient plumes of Martian atmospheric methane ($CH_4$) (Mumma et al., 2009; Webster et al., 2015) have led to suggestions of biotic and/or abiotic surface sources. Fries et al. (2015) suggest the methane plumes are sourced from meteor showers with conversion at high altitudes (Figure 5.1). Using the lessons learned from the work herein, we are able to show that the values of meteoric deposition of Fries et al. (2015) are in excess of any observed or predicted fluences by several orders of magnitude. We additionally show these fluences would have drastic consequences for Mars' atmosphere, and not in the production of methane.

Transient plumes of Martian atmospheric methane (Mumma et al., 2009; Webster et al., 2015) have eluded explanation, and Fries et al. (2015) hypothesizes a meteor shower origin to address this. Schuerger et al. (2012), examined the production of methane near the surface from accreted interplanetary dust particles. They found this mechanism was capable of yielding the background value of methane, but could not reproduce plume densities by

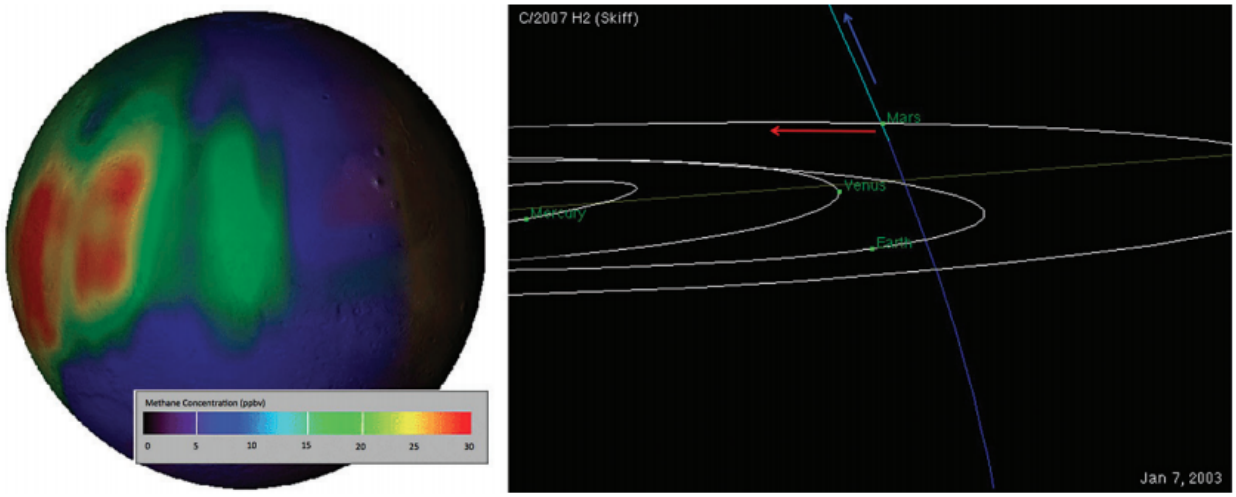


Figure 5.1: From Fries et al. (2015): **(Left)** Methane plume reported by Mumma et al. (2009) showing methane detected in the martian atmosphere on 11 Jan 2003. Image originally from NASA. **(Right)** The locations of Mars and the orbit of comet C/2007 H2 Skiff four days before the methane detection, approximately as seen from Earth. The red arrow shows Mars direction and the blue arrow shows the movement of debris along Skiffs orbit. Image: JPL Small Bodies Database.

bolide, airburst or other meteor impact process. Fries et al. (2015), draw on this work and propose the methane plumes are sourced instead from meteor showers with conversion at high altitudes.

The Fries et al. (2015) methane production mechanism creates a scaling relationship between plume mass and meteor shower deposition, giving 8 x $10^8$ and 2 x $10^8$ kg of meteoric material for the plumes of 45 and 10 ppbv of $CH_4$, respectively (Mumma et al., 2009; Webster et al., 2015). Below we show that even the lower Fries et al. (2015) value is in excess of any observed or predicted fluences by several orders of magnitude.

We first compare the required meteoric mass of Fries et al. (2015) to plausible cometary debris stream masses. A typical cometary radius is 3 km and nominal mass of $10^{13}$ kg, meaning the Fries et al. (2015) value represents 0.001% of the entire comet. While some cometary streams may include as much as $10^9$ kg (Jenniskens, 2006), Fries et al. (2015) claims that Mars could encounter a local concentration of 10% of this total, thus providing a meteoric deposition of $10^8$ kg. Fries et al. (2015) attributes the Mumma et al. (2009) plume to comet C/2007 H2 Skiff, and we can use its ephemeris to compare the volume of a plausible cometary debris stream to the volume Mars sweeps out during a meteor shower ( 1 day). Assuming the debris stream of Skiff has a comparable cross section to Mars, we find the volume swept out by this comet is $10^{18}$ $km^3$. This is more than $10^4$ times the volume that Mars sweeps out (8 x $10^{13}$ $km^3$), which makes the probability of encountering 10% of the total cometary stream mass in this volume highly improbable.

Next, we compare the Fries et al. (2015) values to the global flux of interplanetary dust particles on Earth, which is estimated between 5 x $10^3$ and 3 x $10^5$ kg/day (Plane, 2012). The fluence of meteoric material at Earth is not strongly increased by meteor showers (Grebowsky et al., 1998), which indicates that meteor showers do not deliver significantly more material than the sporadic background. As Mars has 3.5 times less surface area, Fries et al. (2015) therefore requires a normal meteor shower to deliver 2400 times more material than the upper limit of Earths fluence. Compared to observations of Mars' persistent layer, which

suggests a meteoric infall rate of 3 tonnes/day (Crismani et al., 2017b), these values seem too high to be plausible.

Third, we compare the Fries et al. (2015) values to the observed mass fluence during the close encounter of comet C/2013 A1 (Siding Spring), determined to be 1.6 x $10^4$ kg over the planet by Schneider et al. (2015b). Comet Siding Springs dust stream was likely atypically dense, as the nucleus passed within 1.4 x $10^5$ km of Mars, and Mars subsequently passed through the comets relatively fresh debris stream. (Note that Fries et al. (2015) mentions the comet Siding Spring case in the supplementary material, but does not use the observed fluence of Schneider et al. (2015b)). Therefore, the fluence of the largest observed meteor shower at Mars was still four orders of magnitude less than necessary to explain any $CH_4$ plume by the method of Fries et al. (2015).

Finally, we consider other observational consequences of a meteoric deposition of $10^8$ kg. This amount of material entering the atmosphere of Mars at relative orbital velocity (e.g. 35 km/s for comet Skiff) would carry an equivalent energy of 6 x $10^{16}$ J. During the encounter with comet Siding Spring, gas from the coma interacted with the planet and delivered 2.5 x $10^4$ kg (Crismani et al., 2015) and had an equivalent energy of 4 x $10^{13}$ J, which was predicted to raise the temperature in the thermosphere by 30 K (Yelle et al., 2014). Therefore, deposition masses of $10^5$ kg or larger would increase the thermospheric temperature and have readily observable consequences in the form of spacecraft drag (Zurek et al., 2015), thermospheric emissions (Chamberlain and Hunten, 1987), and a strong enhancement in meteoric ions (Crismani et al., 2017b). Moreover, the Fries et al. (2015) required deposition of $10^8$ kg would have a devastating impact to the upper atmosphere, with an energy greater than 1000 nuclear explosions (1 nuclear explosion = 5 x $10^{13}$ J).

### 5.3 Meteoric Origin of Transient Ionospheric Layers is Implausible

Transient ionospheric layers (M3), below Mars' main ionospheric peaks at 120 and 140 km (M1 and M2) were reported by Mars Express (Pätzold et al., 2005) and the Mars Re-

connaissance Orbiter (Withers et al., 2008), by the method of radio occultation (Figure 5.2). These layers were interpreted to be meteoric in origin, based on their altitude, temporal variation, and recombination lifetimes. However, Crismani et al. (2017b) showed these layers contained electron concentrations in excess of ion observations suggesting these layers cannot be created by ablated metals. We detail here how other aspects of the meteoric origin hypothesis are implausible for Mars. Similar layers were also observed for Venus, and we speculate on whether a meteoric origin is appropriate for these layers. This conjecture has implications for both planets, suggesting an undetermined energy source which extends the bottom of their ionospheres to lower altitudes. As the ionosphere couples the neutral atmosphere to the exosphere and solar wind, this energy source may affect atmospheric loss.

Radio occultation measurements determine the abundance of electrons at the tangent point, but are agnostic about the ions that produce such electrons. Since Mars' transient layers were found at altitudes consistent with ablation heights (70-100 km), and temporally varying, similar to meteor showers, it was assumed that this was the source of such electrons. Moreover, the presence of ambient ions at this altitude for long periods of time is problematic, since recombination is rapid below the main ionospheric peak. These layers were observed to exist on the order of hours, and attributing them to meteoric metal ions were preferred due to metallic ion's long lifetimes at high altitudes.

The M3 layer was detected in 1 - 10% of observations, with electron concentrations of $10^4$ cm$^{-3}$, however, these concentrations are problematically high. As demonstrated in Crismani et al. (2017b), $Mg^+$ ions have only been observed in excess of $10^3$ cm$^{-3}$ during the comet Siding Spring meteor shower (with values of $10^5$ cm$^{-3}$). These $Mg^+$ observations are taken in similar observing geometry to radio occultations, so it is unlikely that there is any geometric enhancement to explain the discrepancies in these values. Magnetic field interactions or enhancements are also not a likely explanation, as IUVS observations have been relatively continuous without observing such an enhancement. The lifetime of $Fe^+$ at 90 km is ten times less than $Mg^+$ (Whalley and Plane, 2010), so we do not expect it to

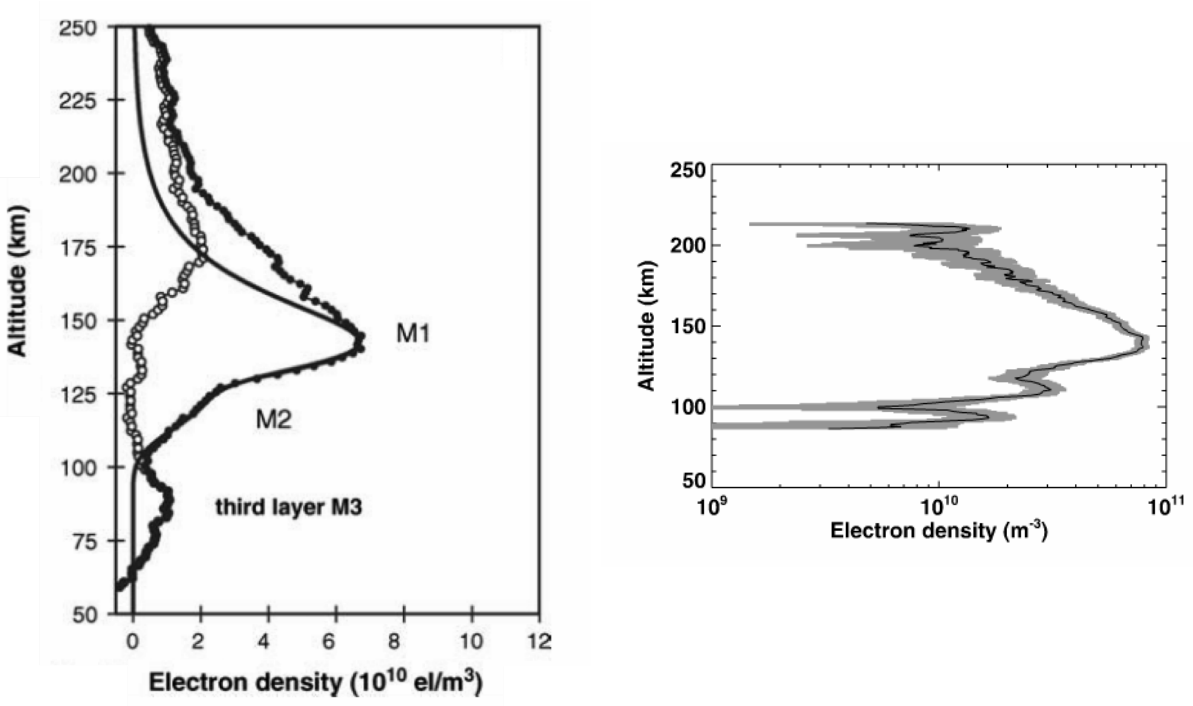


Figure 5.2: **(Left)** From Pätzold et al. (2005): Data from observations on DOY 109, orbit 314, showing layer M3 with peak ionization near 90 km. This layer was present in 10% of observed profiles in the 75 to 105 km altitude range. Altitude is with respect to the Mars Orbiter Laser Altimeter reference surface. **(Right)** From Withers et al. (2008): MGS RS profile 5045K56A.EDS has three clear layers, the M2 layer at 140 km, the M1 layer at 110 km, and the MM layer at 90 km. It was measured at latitude 79.9 N, longitude 316.0 E, 9.9 h LST, Ls = 160.1, and SZA = 73.2 on 14 February 2005. The nominal profile is the solid line, and 1-$\sigma$ uncertainties in the electron densities are marked by the grey region.

contribute significantly to the electron concentration measurement of M3. Therefore the origin of M3 is not readily explained by sporadic meteors.

The meteoric origin of M3 is supported in Pätzold et al. (2005) by noting the similarity in timing between predicted meteor showers and their observations. However, connecting meteor showers to transient events is problematic because these events lack sufficient timing constraints, such that finding a correlation with meteor shower timing is almost guaranteed. This is noted in the rebuttal of Fries et al. (2015) by Roos-Serote et al. (2016), who notes that a careful study of such timing is necessary to determine the probability that an event would occur within a given timeframe of cometary orbital crossing. Such a study has not yet been carried out for Mars meteor showers and M3, however considering the lack of observed meteor showers by IUVS, we posit that a meteor shower origin for M3 is unlikely.

A non-meteoric origin of M3 has implications for Venus, for which there are also observations of transient ionospheric layers below the main ionospheric peaks. Radio occultation measurements by Venus Express suggest that similar layers form, displaying a feature that is not seen in the Mars ionosphere: double peaked layers (Figure 5.3). These peaks are narrow enough that they are observed to be distinct, and seen on multiple occasions. This is fairly unusual with our current understanding of meteoric ablation, resultant chemistry, and dynamics. Specifically, while the altitude of ablation can move up with increasing particle speed, as seen in comet Siding Spring, the particles are rapidly diffused and observations of distinct sources on multiple occasions would be surprising. Lacking constraints on Venus' deposition rates, it is possible that such transient layers are meteoric. There is an expected enhancement in ionization efficiency from meteors at Venus due to its higher relative velocity compared to Earth or Mars, which makes a meteoric origin plausible. Additional analysis and modeling will be necessary to determine whether these layers are meteoric in origin.

If M3 is not meteoric in origin, this implies the presence of an unknown ion source, energy source, or both. This would pose a new challenge for our understanding of the Martian ionosphere, as ambient ions are unable to reproduce the lifetime seen in radio occultation

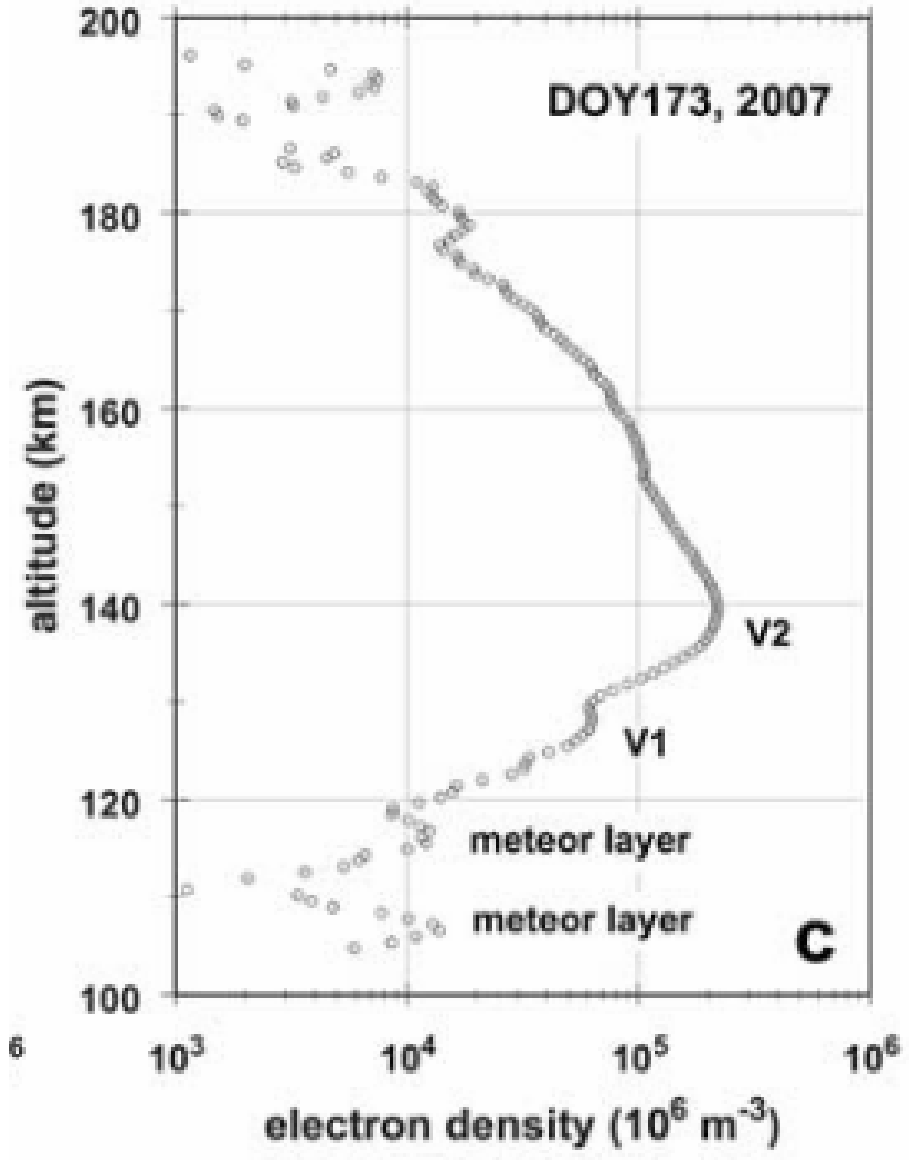


Figure 5.3: From Pätzold et al. (2009): Meteor layers from DOY 173 (Lat. = 72.4N, SZA = 76.8). These demonstrate a double layer where the upper layer merges with V1, but both are well separated from each other. Clearly visible is the bottom side of the V1 layer, which usually forms the lower boundary of the ionosphere. Additional electron density of the meteor layers are evident in all three panels.

observations (more than 10 hours). While $NO^+$ becomes the most abundant ion below 90 km, its lifetime is on the order of hours, not tens of hours. Either the known lifetime of $NO^+$ is not well constrained, which is unlikely, or there is a transient ionizing source that penetrates to low altitude. This source could be soft x-rays, as seen on Earth, however the transient nature would imply a correlation with solar events, which not investigated in the MEx or MRO analysis. As the ionosphere couples the lower atmosphere to the exosphere, a new source of ionization could influence our understanding of the ionosphere's role in atmospheric escape.

The MAVEN's Radio Occultation Science Experiment (ROSE) was recently implemented, and this experiment has not yet produced a "first results" paper, however preliminary profiles do not show these layers (P. Withers, private communication). Their observations should be most similar to previous radio occultations and it remains to be seen whether such layers will be observed. If they are, these observations will be bolstered by concurrent observations of the Martian atmosphere with IUVS and the Sun with MAVEN's Extreme Ultraviolet Monitor. We hope that ROSE will help illuminate the source of these transient layers.

## 5.4 Future Directions for Martian Meteoric Science

The discovery of meteoric species in Mars' upper atmosphere has challenged models of atmospheric chemistry, mesospheric cloud formation, ionospheric transport, and the Martian interplanetary dust environment. Meteoric chemistry in the upper atmosphere has been unable to explain the lack of neutral Mg, which should be deposited during ablation. The formation of high altitude clouds (>40 km) at Mars whose likely origin are meteoric smoke particles has been hindered by unrealistically high model nucleation rates, considering the direct measurement of meteoric dust input (Hartwick and Toon, 2017). Observations of meteoric ions have revealed unexpected dynamics, anomalous high altitude layers (Grebowsky et al., 2017), surprising diurnal variation, and a response to regional dust storms.

Earth's interplanetary dust environment has an order of magnitude uncertainty when comparing various observation techniques (Plane, 2012), and Mars represents a new experiment to constrain such models.

The discovery of $Mg^+$ at Mars immediately exposed an issue in the understanding of meteoric chemistry; electron recombination was expected to yield neutral Mg, yet has not been totally detected by IUVS outside of the encounter with comet Siding Spring. Changing the branching ratio for the recombination of $MgCO_3^+$ reduces the observed Mg to levels consistent with IUVS in the persistent layer (Crismani et al., 2017b), but rapid loss of Mg from observations of comet Siding Spring suggest this may not be the whole story. It may be the case that reactions with $CO_2$ dominate the chemical life of $Mg^+$ and Mg, and eventually convert them to $MgCO_3$ and $Mg(OH)_2$. The former is likely a nucleation site for high altitude clouds (>40 km) and the latter is sensitive to the presence of $H_2O$. While modeled meteoric clouds are able to explain the presence of high altitude clouds, the current flux of meteoric material is insufficient compared to model assumptions, indicating an issue in our understanding of the nucleation process for these clouds. Observations of meteoric molecular compounds such as MgO, $MgCO_3$, $Mg(OH)_2$, and their ions will be necessary to fully understand the Martian meteoric process, from ablation to sedimentation.

Metallic ions have been observed to have spatial distributions independent from other ambient ions, forming anomalous layers above their production region and vertical profiles inconsistent with the expectation of mass separation. Both of these phenomenon may be related to novel chemistry or transport mechanisms, or electrodynamics. The diurnal variation of $Mg^+$ seen by IUVS and NGIMS is not understood in terms of current models (Figure 5.4, left), and may suggest an inadequate modeling of $O_2^+$ in the nightside ionosphere of Mars. Variability in metal emissions from scan to scan and from orbit to orbit has also been observed, and suggests that metallic species do not follow simple diffusive transport. Three dimensional modeling that includes chemistry and self consistent ionospheric transport is necessary to determine what may be causing these varied phenomenon.

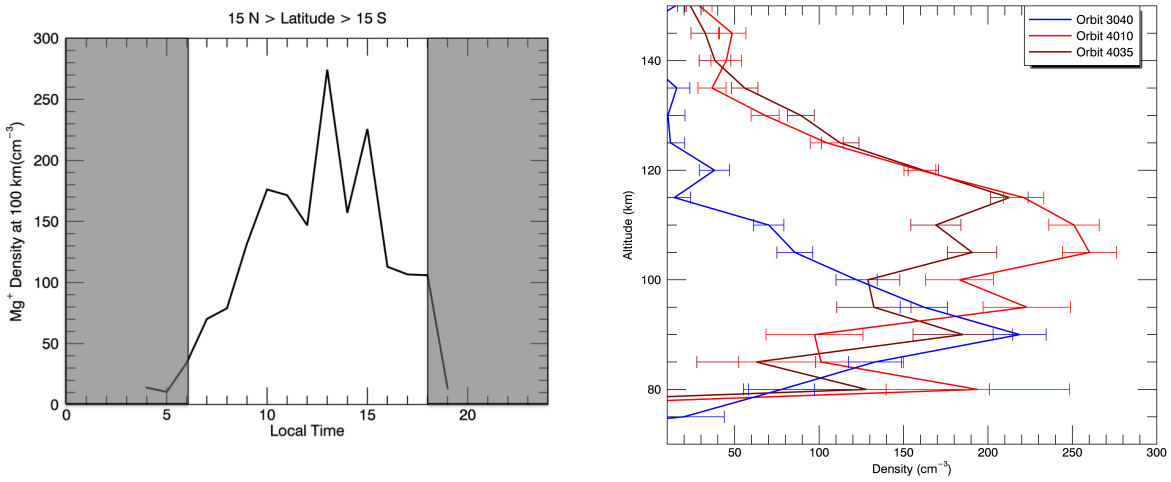


Figure 5.4: **(Left)** $Mg^+$ density at a single height for a range of latitudes is compared for various local times, demonstrating a strong diurnal variation. **(Right)** IUVS observations of $Mg^+$ density after a regional dust storm (orbits 4010-4035) are compared to those from similar observing conditions before the dust storm (orbit 3040).

Seasonal variability cannot be investigated without determining the source or sources of variability that exist on shorter timescales. In addition to the variability mentioned above, the ablation region at Mars has been observed to change in altitude, presumably in response to the changing atmosphere in which meteoric ablation takes place. This is especially evident in observations taken after a regional dust storm, where the ablation layer was seen to shift to altitudes almost as high as seen in comet Siding Spring (Figure 5.4, right). Detrending these variations, it will be possible to use Mars' elliptic orbit to measure changes in the interplanetary dust flux with heliocentric distance. Such a measurement would inform current discussion in the terrestrial meteoric community about the total delivered mass from interplanetary dust particles, which is currently unconstrained within an order of magnitude (Plane, 2012).

These new questions can be resolved by further study with the IUVS and NGIMS instruments, potentially with support of the Trace Gas Orbiter (TGO) instrument suite. Observations over the MAVEN mission are now ready to be considered as a whole. Complete coverage in local time, latitude, and season will allow us to determine whether there are geographic or heliocentric variations in the direction of sporadic meteors, the former of which is seen at Earth. During the extended aerobraking phase, observations of meteoric species by both MAVEN instruments will provide coverage of metallic ions from their production at 90 km to the top of the exobase. This complete coverage may be complemented by TGO below 90 km. If they are able to observe Na, MgO, $MgCO_3$, $Mg(OH)_2$, or their ions, it may allow us to observe more of the chemical and dynamical process of meteoric ablation.

## Bibliography


A., S., Muñoz, A., E., G., S., P., J., G., Pellier, C., Delcroix, M., M., L., F., G., Jaeschke, W., Parker, D., Phillips, J., and Peach, D. (2015). An extremely high-altitude plume seen at mars/' morning terminator. Nature, 518(7540):525–528.

Acuna, M., Connerney, J., Lin, R., Mitchell, D., Carlson, C., McFadden, J., Anderson, K., Rème, H., Mazelle, C., Vignes, D., et al. (1999). Global distribution of crustal magnetization discovered by the mars global surveyor mag/er experiment. Science, 284(5415):790–793.

Adolfsson, L. G., Gustafson, B., and Murray, C. D. (1996). The martian atmosphere as a meteoroid detector. Icarus, 119(1):144–152.

Ahearn, M., Schleicher, D., and Feldman, P. (1983). The discovery of s2 in comet iras-araki-alcock 1983d. The Astrophysical Journal, 274:L99–L103.

Anderson, J. G. and Barth, C. A. (1971). Rocket investigation of the mg i and mg II dayglow. J Geophys Res, 76(16):3723–3732.

Andersson, L., Ergun, R., Delory, G., Eriksson, A., Westfall, J., Reed, H., McCauly, J., Summers, D., and Meyers, D. (2015a). The langmuir probe and waves (lpw) instrument for maven. Space Science Reviews, 195(1-4):173–198.

Andersson, L., Weber, T., Malaspina, D., Crary, F., Ergun, R., Delory, G., Fowler, C., Morooka, M., T, M., Eriksson, A., Andrews, D., Horanyi, M., Collette, A., Yelle, R., and Jakosky, B. (2015b). Dust observations at orbital altitudes surrounding mars. Sci New York N Y, 350(6261):aad0398.

Asher, D. (1999). The leonid meteor storms of 1833 and 1966. Monthly Notices of the Royal Astronomical Society, 307(4):919–924.

Atreya, S., Mahaffy, P., and Wong, A. (2007). Methane and related trace species on mars: Origin, loss, implications for life, and habitability. Planet Space Sci, 55(3):358–369.

B, S., Lester, M., Witasse, O., Milan, S., Hall, B., Cartacci, M., Peter, K., Morgan, D., Blelly, P., Radicella, S., Cicchetti, A., Noschese, R., Orosei, R., and Pätzold, M. (2016). Solar cycle variations in the ionosphere of mars as seen by multiple mars express data sets. J Geophys Res Space Phys, 121(3):2547–2568.

Barth, C., Fastie, W., Hord, C., Pearce, J., Kelly, K., Stewart, A., Thomas, G., Anderson, G., and Raper, O. (1971a). Mariner 6: Ultraviolet spectrum of mars upper atmosphere. In Symposium-International Astronomical Union, volume 40, pages 253–256. Cambridge University Press.

Barth, C., Hord, C., Pearce, J., Kelly, K., Anderson, G., and Stewart, A. (1971b). Mariner 6 and 7 ultraviolet spectrometer experiment: Upper atmosphere data. Journal of Geophysical Research, 76(10):2213–2227.

Barth, C. A. and Hord, C. W. (1971). Mariner ultraviolet spectrometer: Topography and polar cap. Science, 173(3993):197–201.

Benna, M., Mahaffy, P., Grebowsky, J., Plane, J., Yelle, R., and Jakosky, B. (2015). Metallic ions in the upper atmosphere of mars from the passage of comet c/2013 a1 (Siding spring). Geophys Res Lett, 42(12):4670–4675.

Bertaux, J., Kyrölä, E., Quémerais, E., Pellinen, R., Lallement, R., Schmidt, W., Berthé, M., Dimarellis, E., Goutail, J., Taulemesse, C., et al. (1995). SWAN: A study of solar wind anisotropies on SOHO with Lyman alpha sky mapping. Solar physics, 162(1-2):403–439.

Bertaux, J.-L., Korablev, O., Perrier, S., Quemerais, E., Montmessin, F., Leblanc, F., Lebonnois, S., Rannou, P., Lefèvre, F., Forget, F., et al. (2006). SPICAM on Mars Express: Observing modes and overview of UV spectrometer data and scientific results. Journal of Geophysical Research: Planets (1991–2012), 111(E10).

Bevington, P. and Robinson, D. (2003). Data reduction and error analysis. McGraw–Hill.

Bevington, P. R. and Robinson, D. K. (1969). Data Reduction and Error Analysis for the Physical Sciences, volume 336. McGraw-Hill New York.

Bhattacharyya, D., Clarke, J., Bertaux, J., Chaufray, J., and Mayyasi, M. (2016). Analysis and modeling of remote observations of the martian hydrogen exosphere. Icarus.

Bhattacharyya, D., Clarke, J. T., Bertaux, J., Chaufray, J., and Mayyasi, M. (2015). A strong seasonal dependence in the martian hydrogen exosphere. Geophys Res Lett, 42(20):8678–8685.

Bockelée-Morvan, D., Crovisier, J., Mumma, M., and Weaver, H. (2004). The composition of cometary volatiles. Comets II, 391.

Bodewits, D., Farnham, T., M., A., Feaga, L., A., M., Schleicher, D., and Sunshine, J. (2014). The evolving activity of the dynamically young comet C/2009 P1 (Garradd). Astrophysical J, 786(1):48.

Bodewits, D., Kelley, M., Li, J., Farnham, T., and Michael, A. (2015). The pre-perihelion activity of dynamically new comet C/2013 A1 (siding spring) and its close encounter with mars. Astrophysical J Lett, 802(1):L6.

Bodewits, D., Villanueva, G., Mumma, M., Landsman, W., Carter, J., and Read, A. (2011). Swift-UVOT grism spectroscopy of comets: A first application to C/2007 N3 (Lulin). The Astronomical Journal, 141(1):12.

Boksenberg, A. and Gérard, J. (1973). Ultraviolet observations of equatorial dayglow above the f 2 peak. J Geophys Res, 78(22):4641–4650.

Bougher, S., Engel, S., Roble, R., and Foster, B. (1999). Comparative terrestrial planet thermospheres: 2. solar cycle variation of global structure and winds at equinox. J Geophys Res Planets 1991 2012, 104(E7):16591–16611.

Bougher, S., Jakosky, B., Halekas, J., Grebowsky, J., Luhmann, J., Mahaffy, P., Connerney, J., Eparvier, F., Ergun, R., Larson, D., J, M., Mitchell, D., Schneider, N., Zurek, R., Mazelle, C., Andersson, L., Andrews, D., Baird, D., Baker, D., Bell, J., Benna, M., Brain, D., Chaffin, M., Chamberlin, P., Chaufray, J., Clarke, J., Collinson, G., Combi, M., Crary, F., Cravens, T., Crismani, M., Curry, S., Curtis, D., Deighan, J., Delory, G., Dewey, R., G, D., Dong, C., Dong, Y., Dunn, P., Elrod, M., England, S., Eriksson, A., Espley, J., Evans, S., Fang, X., Fillingim, M., Fortier, K., Fowler, C., Fox, J., Groller, H., Guzewich, S., Hara, T., Harada, Y., Holsclaw, G., Jain, S., Jolitz, R., Leblanc, F., Lee, C., Lee, Y., Lefevre, F., Lillis, R., Livi, R., Lo, D., Ma, Y., Mayyasi, M., W, M., T, M., Modolo, R., Montmessin, F., Morooka, M., Nagy, A., Olsen, K., Peterson, W., Rahmati, A., Ruhunusiri, S., Russell, C., Sakai, S., Sauvaud, J., Seki, K., Steckiewicz, M., Stevens, M., Stewart, A., Stiepen, A., Stone, S., Tenishev, V., Thiemann, E., Tolson, R., Toublanc, D., Vogt, M., Weber, T., Withers, P., Woods, T., and Yelle, R. (2015a). Early MAVEN deep dip campaign reveals thermosphere and ionosphere variability. Science, 350(6261):aad0459–aad0459.

Bougher, S., Pawlowski, D., Bell, J., Nelli, S., M., T., Murphy, J., Chizek, M., and Ridley, A. (2015b). Mars Global Ionosphere-Thermosphere Model: Solar cycle, seasonal, and diurnal variations of the Mars upper atmosphere. Geophysical Research Letters - Planets, 120:311–342.

Bougher, S. W., Roeten, K., Olsen, K., Mahaffy, P. R., Benna, M., Elrod, M., Jain, S., Schneider, N. M., Deighan, J., Thiemann, E., Eparvier, F. G., Stiepen, A., and Jakosky, B. (2016). The structure and variability of mars dayside thermosphere from MAVEN NGIMS and IUVS measurements: Seasonal and solar activity trends in scale heights and temperatures. J Geophys Res Space Phys.

Brain, D. A., McFadden, J., Halekas, J. S., Connerney, J., Bougher, S. W., Curry, S., Dong, C., Dong, Y., Eparvier, F., Fang, X., et al. (2015). The spatial distribution of planetary ion fluxes near mars observed by maven. Geophysical Research Letters, 42(21):9142–9148.

Budzien, S., Festou, M., and Feldman, P. (1994). Solar flux variability and the lifetimes of cometary h 2 o and oh. Icarus, 107(1):164–188.

Burnham, R. (2000). Great comets. Cambridge University Press.

Bush, B. and Chakrabarti, S. (1995). A radiative transfer model using spherical geometry and partial frequency redistribution. Journal of Geophysical Research: Planets, 100(A10):19627–19642.

Campbell-Brown, Blaauw, R., and Kingery, A. (2016). Optical fluxes and meteor properties of the camelopardalid meteor shower. Icarus, 277:141–153.

Carrillo-Sánchez, J., Nesvornỳ, D., Pokornỳ, P., Janches, D., and Plane, J. (2016). Sources of cosmic dust in the earth's atmosphere. Geophysical Research Letters, 43(23).

CarrilloSánchez, J., Plane, J., Feng, W., Nesvorný, D., and Janches, D. (2015). On the size and velocity distribution of cosmic dust particles entering the atmosphere. Geophys Res Lett, 42(15):6518–6525.

Chaffin, M., Chaufray, J., Deighan, J., Schneider, N., W., M., Stewart, A., Thiemann, E., Clarke, J., Holsclaw, G., Jain, S., Crismani, M., Stiepen, A., Montmessin, F., Eparvier, F., Chamberlain, P., and Jakosky, B. (2015). Threedimensional structure in the mars h corona revealed by IUVS on MAVEN. Geophys Res Lett, 42(21):9001–9008.

Chaffin, M., Chaufray, J., and Stewart, I. (2014). Unexpected variability of martian hydrogen escape. Geophysical Research Letters, 41(2):314–320.

Chaffin, M., Deighan, J., Schneider, N., and Stewart, I. F. A. (2017). Elevated atmospheric escape of atomic hydrogen from mars induced by high-altitude water. Nat Geosci.

Chamberlain, J. and Hunten, D. (1987). Theory of planetary atmospheres. An introduction to their physics and chemistry.

Chamberlain, J. W. (1963). Planetary coronae and atmospheric evaporation. Planet Space Sci, 11(8):901–960.

Chaufray, J., Bertaux, J., Leblanc, F., and Quémerais, E. (2008). Observation of the hydrogen corona with SPICAM on mars express. Icarus, 195(2):598–613.

Chaufray, J., Deighan, J., Chaffin, M., Schneider, N., W., M., Stewart, A., Jain, S., Crismani, M., Stiepen, A., Holsclaw, G., Clarke, J., Montmessin, F., Eparvier, F., Thiemann, E., Chamberlin, P., and Jakosky, B. (2015). Study of the martian cold oxygen corona from the oi 130.4nm by IUVS/MAVEN. Geophys Res Lett, 42(21):9031–9039.

Cheng, A. F., Hibbitts, C., Espiritu, R., R, M., Fletcher, Z., Bernasconi, P., Adams, J., Lisse, C., Sitko, M., Fernandes, R., Young, E., and Kremic, T. (2016). Stratospheric balloon observations of comets c/2013 a1 (Siding spring), c/2014 e2 (Jacques), and ceres. Icarus.

Chicarro, A., Martin, P., and Trautner, R. (2004). The mars express mission: an overview. In Mars Express: The Scientific Payload, volume 1240, pages 3–13.

Christon, S., Hamilton, D., Plane, J., Mitchell, D., DiFabio, R., and Krimigis, S. (2015). Discovery of suprathermal fe+ in saturn's magnetosphere. Journal of Geophysical Research: Space Physics, 120(4):2720–2738.

Christon, S., Hamilton, D., Plane, J., Mitchell, D., Grebowsky, J., Spjeldvik, W., and Nylund, S. (2017). Discovery of suprathermal ionospheric origin fe+ in and near earth's magnetosphere. Journal of Geophysical Research: Space Physics.

Christou, A. (2010). Annual meteor showers at venus and mars: lessons from the earth. Mon Not R Astron Soc, 402(4):2759–2770.

Christou, A. and Beurle, K. (1999). Meteoroid streams at mars: possibilities and implications. Planet Space Sci, 47(12):1475–1485.

Christou, A., Oberst, J., Elgner, S., Flohrer, J., Margonis, A., J.P., M., and Koschny, D. (2012). Orbital observations of meteors in the martian atmosphere using the SPOSH camera. Planet Space Sci, 60(1):229–235.

Christou, A. and Vaubaillon, J. (2011). Numerical modeling of cometary meteoroid streams encountering mars and venus.

Christou, A., Vaubaillon, J., and Withers, P. (2007). The dust trail complex of comet 79P/du Toit-Hartley and meteor outbursts at mars. Astronomy & Astrophysics.

Christou, A. A. (2006). Predicting martian and venusian meteor shower activity. Earth Moon Planets, 95(1-4):425–431.

Christou, A. A., Vaubaillon, J., and Withers, P. (2008). The P/Halley stream: Meteor showers on earth, venus and mars. Earth Moon Planets, 102(1-4):125–131.

Clancy, R. T., Wolff, M. J., Whitney, B. A., Cantor, B. A., and Smith, M. D. (2007). Mars equatorial mesospheric clouds: Global occurrence and physical properties from mars global surveyor thermal emission spectrometer and mars orbiter camera limb observations. Journal of Geophysical Research: Planets, 112(E4).

Clarke, J., Bertaux, J., and Chaufray, J. (2014). A rapid decrease of the hydrogen corona of mars. Geophysical Research Letters, 41(22):8013–8020.

Clarke, J., Mayyasi, M., Bhattacharyya, D., Schneider, N., WE, M., Deighan, J., Stewart, A., Chaufray, J., Chaffin, M., Jain, S., Stiepen, A., Crismani, M., Holsclaw, G., Montmessin, F., and Jakosky, B. (2017). Variability of d and h in the martian upper atmosphere observed with the MAVEN IUVS echelle channel. J Geophys Res Space Phys.

Collinson, G. A., Frahm, R. A., Glocer, A., Coates, A. J., Grebowsky, J. M., Barabash, S., Domagal-Goldman, S. D., Fedorov, A., Futaana, Y., Gilbert, L. K., et al. (2016). The electric wind of venus: A global and persistent "polar wind"-like ambipolar electric field sufficient for the direct escape of heavy ionospheric ions. Geophysical Research Letters, 43(12):5926–5934.

Combi, M., Brown, M., and Feldman, P. (1998). Hubble space telescope ultraviolet imaging and high-resolution spectroscopy of water photodissociation products in comet hyakutake (C/1996 b2). The Astrophysical Journal, 494(2):816–821.

Combi, M., Mäkinen, J., Bertaux, J., and Quemérais, E. (2005). Temporal deconvolution of the hydrogen coma II. pre- and post-perihelion activity of comet hyakutake (1996 b2). Icarus, 177(1):228–245.

Combi, M., Reinard, A., Bertaux, J., Quemerais, E., and Mäkinen, T. (2000). SOHO/SWAN observations of the structure and evolution of the hydrogen lyman- coma of comet Hale–Bopp (1995 o1). Icarus, 144(1):191–202.

Combi, M., Tenishev, V., Rubin, M., Fougere, N., and Gombosi, T. I. (2012). Narrow dust jets in a diffuse gas coma: A natural product of small active regions on comets. Astrophysical J, 749(1):29.

Combi, M. R. (1996). Time-dependent gas kinetics in tenuous planetary atmospheres: The cometary coma. Icarus, 123(1):207–226.

Combi, M. R., Harris, W. M., and Smyth, W. H. (2004). Gas dynamics and kinetics in the cometary coma: Theory and observations. Icarus, 1(1):523–552.

Correira, J. (2009). Temporal and spatial distribution of metallic species in the upper atmosphere. Journal of Geophysical Research: Planets.

Correira, J., Aikin, A., Grebowsky, J., Pesnell, W., and Burrows, J. (2008). Seasonal variations of magnesium atoms in the mesospherethermosphere. Geophys Res Lett, 35(6).

Crismani, M., Schneider, N., and Plane, J. (2017a). Comment on "a cometary origin for atmospheric martian methane" by fries et al., 2016. Geochem. Perspect. Lett, 3.

Crismani, M. M., Schneider, N. M., Deighan, J. I., Stewart, A. I. F., Combi, M., Chaffin, M. S., Fougere, N., Jain, S. K., Stiepen, A., Yelle, R. V., et al. (2015). Ultraviolet observations of the hydrogen coma of comet c/2013 a1 (siding spring) by maven/iuvs. Geophysical Research Letters, 42(21):8803–8809.

Crismani, M. M., Schneider, N. M., Plane, J. M., Evans, J. S., Jain, S. K., Chaffin, M. S., Carrillo-Sanchez, J., Deighan, J. I., Yelle, R., Stewart, A. I. F., et al. (2017b). Detection of a persistent meteoric metal layer in the martian atmosphere. Nature Geoscience, 10(6):401–404.

Deighan, J., Chaffin, M., Chaufray, J., Stewart, A., Schneider, N., Jain, S., Stiepen, A., Crismani, M., W., M., Clarke, J., Holsclaw, G., Montmessin, F., Eparvier, F., Thiemann, E., Chamberlin, P., and Jakosky, B. (2015). MAVEN IUVS observation of the hot oxygen corona at mars. Geophys Res Lett, 42(21):9009–9014.

Dishoeck, E. F. and Dalgarno, A. (1984). The dissociation of OH and OD in comets by solar radiation. Icarus, 59(3):305–313.

Domokos, A., Bell, J., Brown, P., Lemmon, M., Suggs, R., Vaubaillon, J., and Cooke, W. (2007). Measurement of the meteoroid flux at mars. Icarus, 191(1):141–150.

Dymond, K., Wolfram, K., and Budzien, S. (2003). Middle ultraviolet emission from ionized iron. Geophysical Research Letters.

Eddington, A. S. (1910). The envelopes of comet morehouse (1908 c). Monthly Notices of the Royal Astronomical Society, 70(5):442–458.

Elrod, M., Bougher, S., Bell, J., Mahaffy, P., Benna, M., Stone, S., Yelle, R., and Jakosky, B. (2017). He bulge revealed: He and CO2 diurnal and seasonal variations in the upper atmosphere of mars as detected by MAVEN NGIMS. J Geophys Res Space Phys.

Ergun, R., Andersson, L., Fowler, C., Woodson, A., Weber, T., Delory, G., Andrews, D., Eriksson, A., T, M., Morooka, M., Stewart, A., Mahaffy, P., and Jakosky, B. (2016). Enhanced o2+ loss at mars due to an ambipolar electric field from electron heating. J Geophys Res Space Phys, 121(5):4668–4678.

Espley, J., Gina, D., Connerney, J., Brain, D., Gruesbeck, J., Soobiah, Y., Halekas, J., Combi, M., Luhmann, J., Ma, Y., Jia, Y., and Jakosky, B. (2015). A comet engulfs mars: MAVEN observations of comet siding spring's influence on the martian magnetosphere. Geophys Res Lett, 42(21):8810–8818.

Evans, J. S., Stevens, M. H., Lumpe, J. D., Schneider, N. M., Stewart, A. I. F., Deighan, J., Jain, S. K., Chaffin, M. S., Crismani, M., Stiepen, A., et al. (2015). Retrieval of co2 and n2 in the martian thermosphere using dayglow observations by iuvs on maven. Geophysical Research Letters, 42(21):9040–9049.

Farnocchia, D., Chesley, S., Chodas, P., Tricarico, P., Kelley, M., and Farnham, T. (2014). Trajectory analysis for the nucleus and dust of comet C/2013 A1 (Siding spring). The Astrophysical Journal Letters.

Fegley, B. and Cameron, A. (1987). A vaporization model for iron/silicate fractionation in the mercury protoplanet. Earth and Planetary Science Letters, 82(3-4):207–222.

Feldman, P. (1982). Ultraviolet spectroscopy of comae. Comets, Univ. of Arizona Press, Tucson, pages 461–479.

Feldman, P. D., Cochran, A. L., and Combi, M. R. (2004). Spectroscopic investigations of fragment species in the coma. Astrophysical J, 1:425–447.

Fesen, C. and Hays, P. B. (1982). Two-dimensional inversion technique for satellite airglow data. Appl Optics, 21(20):3784.

Flynn, G. J. (2002). NEAR-EARTH ENVIRONMENT. Cambridge University Press.

Forget, F., Montmessin, F., Bertaux, J., Francisco, G., Lebonnois, S., Quémerais, E., Reberac, A., Dimarellis, E., and Miguel, L. (2009). Density and temperatures of the upper martian atmosphere measured by stellar occultations with mars express SPICAM. J Geophys Res Planets 1991 2012, 114(E1).

Formisano, V., Atreya, S., Encrenaz, T., and Ignatiev, N. (2004). Detection of methane in the atmosphere of mars.

Fougere, N. (2014). The Complex Outgassing of Comets and the Resulting Coma, a Direct Simulation Monte-Carlo Approach. PhD thesis, University of Michigan.

Fougere, N., Combi, M., Rubin, M., and Tenishev, V. (2013). Modeling the heterogeneous ice and gas coma of comet 103P/Hartley 2. Icarus, 225(1):688–702.

Fougere, N., Combi, M., Tenishev, V., Rubin, M., Bonev, B., and Mumma, M. (2012). Understanding measured water rotational temperatures and column densities in the very innermost coma of comet 73P/SchwassmannWachmann 3 b. Icarus, 221(1):174–185.

Fowler, C., Andersson, L., Ergun, R., Morooka, M., Delory, G., Andrews, D. J., Lillis, R. J., McEnulty, T., Weber, T., Chamandy, T., et al. (2015). The first in situ electron temperature and density measurements of the martian nightside ionosphere. Geophysical Research Letters, 42(21):8854–8861.

Fox, J. (2004). Advances in the aeronomy of venus and mars. Adv Space Res-series, 33(2):132–139.

Fränz, M., Dubinin, E., Andrews, D., Barabash, S., Nilsson, H., and Fedorov, A. (2015). Cold ion escape from the martian ionosphere. Planet Space Sci, 119:92–102.

Fries, M., Christou, A., Archer, D., Conrad, P., Cooke, W., Eigenbrode, J., Kate, I., Matney, M., Niles, P., Sykes, M., Steele, A., and Treiman, A. (2015). A cometary origin for martian atmospheric methane. Geochem Perspectives Lett, 2(1):10–23.

Gardner, C., Liu, A., Marsh, D., Feng, W., and Plane, J. (2014). Inferring the global cosmic dust influx to the earth's atmosphere from lidar observations of the vertical flux of mesospheric na. J Geophys Res Space Phys, 119(9):7870–7879.

Gérard, J. and Monfils, A. (1978). The mg II equatorial airglow altitude distribution. J Geophys Res Space Phys 1978 2012, 83(A9):4389–4391.

Gérard, J., Soret, L., Libert, L., Lundin, R., Stiepen, A., Radioti, A., and Bertaux, J. (2015). Concurrent observations of ultraviolet aurora and energetic electron precipitation with mars express. J Geophys Res Space Phys, 120(8):6749–6765.

Girazian, Z., Mahaffy, P., Lillis, R., Benna, M., Elrod, M., and Jakosky, B. (2017). Nightside ionosphere of mars: Composition, vertical structure, and variability. Journal of Geophysical Research: Space Physics, 122(4):4712–4725.

Girazian, Z., Withers, P., Häusler, B., Pätzold, M., Tellmann, S., and Peter, K. (2015). Characterization of the lower layer in the dayside venus ionosphere and comparisons with mars. Planet Space Sci, 117:146–158.

G.J, M., Lammer, H., Stumptner, W., Schwingenschuh, K., Rucker, H., J.J, L., Rodrigo, R., and Tokano, T. (2001). Ionospheric layer induced by meteoric ionization in titan's atmosphere. Planetary and Space Science, pages 143–153.

Graf, J. E., Zurek, R. W., Eisen, H. J., Jai, B., Johnston, M., and DePaula, R. (2005). The mars reconnaissance orbiter mission. Acta Astronautica, 57(2):566–578.

Granvik, M., Morbidelli, A., Jedicke, R., Bolin, B., Bottke, W. F., Beshore, E., Vokrouhlický, D., Delbò, M., and Michel, P. (2016). Super-catastrophic disruption of asteroids at small perihelion distances. Nature, 530(7590):303–306.

Grebowsky, J., Benna, M., Plane, J., Collinson, G., Mahaffy, P., and Jakosky, B. (2017). Unique, non-earthlike, meteoritic ion behavior in upper atmosphere of mars. Geophysical Research Letters, 44(7):3066–3072.

Grebowsky, J., Goldberg, R., and Pesnell, W. (1998). Do meteor showers significantly perturb the ionosphere? J Atmos Sol-terr Phy, 60(6):607–615.

Grinspoon, D. and Lewis, J. (1988). Cometary water on venus: Implications of stochastic impacts. Icarus, 74(1):21–35.

Gröller, H., Yelle, R., Koskinen, T., Montmessin, F., Lacombe, G., Schneider, N., Deighan, J., Stewart, A., Jain, S., Chaffin, M., Crismani, M., Stiepen, A., Lefèvre, F., W., M., Clarke, J., Holsclaw, G., Mahaffy, P., Bougher, S., and Jakosky, B. (2015). Probing the martian atmosphere with MAVEN/IUVS stellar occultations. Geophys Res Lett, 42(21):9064–9070.

Gronoff, G., Rahmati, A., Wedlund, C., Mertens, C., Cravens, T., and Kallio, E. (2014). The precipitation of keV energetic oxygen ions at mars and their effects during the comet siding spring approach. Geophys Res Lett, 41(14):4844–4850.

Grotzinger, J. P., Arvidson, R., Bell, J., Calvin, W., Clark, B., Fike, D., Golombek, M., Greeley, R., Haldemann, A., Herkenhoff, K., et al. (2005). Stratigraphy and sedimentology of a dry to wet eolian depositional system, burns formation, meridiani planum, mars. Earth and Planetary Science Letters, 240(1):11–72.

Grün, E., Zook, H., Fechtig, H., and Giese, R. (1985). Collisional balance of the meteoritic complex. Icarus, 62(2):244–272.

Gumbel, J., Fan, Z., Waldemarsson, T., Stegman, J., Witt, G., Llewellyn, E., She, C., and Plane, J. (2007). Retrieval of global mesospheric sodium densities from the odin satellite. Geophys Res Lett, 34(4).

Gurnett, D., Morgan, D., Persoon, A., Granroth, L., Kopf, A., Plaut, J., and Green, J. (2015). An ionized layer in the upper atmosphere of mars caused by dust impacts from comet siding spring. Geophys Res Lett, 42(12):4745–4751.

Haider, S., Abdu, M., Batista, I., Sobral, J., Luan, X., Kallio, E., Maguire, W., Verigin, M., and Singh, V. (2009). D, e, and f layers in the daytime at high-latitude terminator ionosphere of mars: Comparison with earth's ionosphere using cosmic data. Journal of Geophysical Research: Space Physics, 114(A3).

Haider, S., Pandya, B., and GJ, M. (2013). Nighttime ionosphere caused by meteoroid ablation and solar wind electronprotonhydrogen impact on mars: MEX observation and modeling. J Geophys Res Space Phys, 118(10):6786–6794.

Haider, S. A. and Pandya, B. M. (2015). Probing of meteor showers at mars during the encounter of comet c/2013 a1: predictions for the arrival of maven/mangalyaan. Geoscience Letters, 2(1):1–13.

Halekas, J., Ruhunusiri, S., Harada, Y., Collinson, G., Mitchell, D., Mazelle, C., JP, M., Connerney, J., Espley, J., Eparvier, F., Luhmann, J., and Jakosky, B. (2016). Structure, dynamics, and seasonal variability of the marssolar wind interaction: MAVEN solar wind ion analyzer inflight performance and science results. J Geophys Res Space Phys.

Harris, W. M., Scherb, F., Mierkiewicz, E., Oliversen, R., and Morgenthaler, J. (2002). Production, outflow velocity, and radial distribution of H2O and OH in the coma of comet c/1995 o1 (Hale-Bopp) from wide-field imaging of OH. Astrophysical J, 578(2):996.

Hartwick, V. and Toon, O. (2017). Micrometeoric ablation biproducts as a high altitude source for ice nuclei in the present day martian atmosphere. In The Sixth International Workshop on the Mars Atmosphere, page 4103.

Haser, L. (1957). Distribution d'intensité dans la tête d'une comète. Bulletin de la Societe Royale des Sciences de Liege, 43:740–750.

Hearn, M., Ohlmacher, J., and Schleicher, D. (1983). A high resolution solar atlas for fluorescence calculations. Personal Communication.

Helmer, M., Plane, J., Qian, J., and Gardner, C. (1998). A model of meteoric iron in the upper atmosphere. J Geophys Res Atmospheres 1984 2012, 103(D9):10913–10925.

Höffner, J. and Friedman, J. (2004). The mesospheric metal layer topside: a possible connection to meteoroids. Atmos Chem Phys, 4(3):801–808.

Hu, R., Bloom, A., Gao, P., Miller, C., and Yung, Y. (2016). Hypotheses for near-surface exchange of methane on mars. arXiv preprint.

Huebner, W. F., Keady, J. J., and Lyon, S. (1992). Solar photo rates for planetary atmospheres and atmospheric pollutants. Astrophysics and Space Science, 195(1):1–294.

Irvine, W., Schloerb, F., and Crovisier, J. (2000). Comets: A link between interstellar and nebular chemistry.

Istomin, V. (1963). Ions of extra-terrestrial origin in the earth's ionosphere. Planet Space Sci, 11(2):173–174.

Jain, S., Stewart, A., Schneider, N., Deighan, J., Stiepen, A., Evans, J., Stevens, M., Chaffin, M., Crismani, M., W., M., Clarke, J., Holsclaw, G., Lo, D., Lefèvre, F., Montmessin, F., Thiemann, E., Eparvier, F., and Jakosky, B. (2015). The structure and variability of mars upper atmosphere as seen in MAVEN/IUVS dayglow observations. Geophys Res Lett, 42(21):9023–9030.

Jakosky, B., Grebowsky, J., Luhmann, J., Connerney, J., Eparvier, F., Ergun, R., Halekas, J., Larson, D., Mahaffy, P., J, M., Mitchell, D., Schneider, N., Zurek, R., Bougher, S., Brain, D., Ma, Y., Mazelle, C., Andersson, L., Andrews, D., Baird, D., Baker, D., Bell, J., Benna, M., Chaffin, M., Chamberlin, P., Chaufray, Y., Clarke, J., Collinson, G., Combi, M., Crary, F., Cravens, T., Crismani, M., Curry, S., Curtis, D., Deighan, J., Delory, G., Dewey, R., G, D., Dong, C., Dong, Y., Dunn, P., Elrod, M., England, S., Eriksson, A., Espley, J., Evans, S., Fang, X., Fillingim, M., Fortier, K., Fowler, C., Fox, J., Gröller, H., Guzewich, S., Hara, T., Harada, Y., Holsclaw, G., Jain, S., Jolitz, R., Leblanc, F., Lee, C., Lee, Y., Lefevre, F., Lillis, R., Livi, R., Lo, D., Mayyasi, M., W, M., T, M., Modolo, R., Montmessin, F., Morooka, M., Nagy, A., Olsen, K., Peterson, W., Rahmati, A., Ruhunusiri, S., Russell, C., Sakai, S., Sauvaud, J., Seki, K., Steckiewicz, M., Stevens, M., Stewart, A., Stiepen, A., Stone, S., Tenishev, V., Thiemann, E., Tolson, R., Toublanc, D., Vogt, M., Weber, T., Withers, P., Woods, T., and Yelle, R. (2015a). MAVEN observations of the response of mars to an interplanetary coronal mass ejection. Sci New York N Y, 350(6261):aad0210.

Jakosky, B., Lin, R., Grebowsky, J., and Luhmann, J. (2015b). The mars atmosphere and volatile evolution (MAVEN) mission. Space Science Reviews.

Jakosky, B. M., Slipski, M., Benna, M., Mahaffy, P., Elrod, M., Yelle, R., Stone, S., and Alsaeed, N. (2017). Mars' atmospheric history derived from upper-atmosphere measurements of 38ar/36ar. Science, 355(6332):1408–1410.

Janches, D., Palo, S., Lau, E., Avery, S., Avery, J., Peña, S., and Makarov, N. (2004). Diurnal and seasonal variability of the meteoric flux at the south pole measured with radars. Geophys Res Lett, 31(20).

Janches, D., Plane, J., Nesvorný, D., Feng, W., Vokrouhlický, D., and Nicolls, M. (2014). Radar detectability studies of slow and small zodiacal dust cloud particles. i. the case of arecibo 430 MHz meteor head echo observations. Astrophysical J, 796(1):41.

JB, M., Feldman, P., and SR, M. (1999). Rocket-borne long-slit ultraviolet spectroscopy of comet Hale-Bopp. The Astrophysical Journal, 521(2):920–927.

Jeans, J. H. (1921). The dynamical theory of gases. University Press.

Jenniskens, P. (2006). Meteor showers and their parent comets. Cambridge University Press.

Jenniskens, P. (2017). Meteor showers in review. Planet Space Sci.

JG, M., JJ, L., and Arnold, F. (2008). Meteoric layers in planetary atmospheres. Space Sci Rev, 137(1-4):175–191.

Johnson, R., Cooper, J., Lanzerotti, L., and Strazzulla, G. (1988). Radiation formation of a non-volatile comet crust. In Exploration of Halley's Comet, pages 889–892. Springer.

Joiner, J. and Aikin, A. (1996). Temporal and spatial variations in upper atmospheric mg+. J Geophys Res Space Phys 1978 2012, 101(A3):5239–5249.

Jones, J., Brown, P., Ellis, K., Webster, A., M., C., Krzemenski, Z., and Weryk, R. (2005). The canadian meteor orbit radar: system overview and preliminary results. Planet Space Sci, 53(4):413–421.

JP, M. and Christou, A. (2006). Simulating meteor showers in the martian atmosphere.

JPL (2015). Horizons database, http://ssd.jpl.nasa.gov/horizons.cgi.

Kasting, J. and Pollack, J. (1983). Loss of water from venus. i. hydrodynamic escape of hydrogen. Icarus, 53(3):479–508.

Kelleher, D. E. and Podobedova, L. (2008). Atomic transition probabilities of sodium and magnesium. a critical compilation. Journal of Physical and Chemical Reference Data, 37(1):267–706.

Kelley, M. S., Farnham, T. L., Bodewits, D., Tricarico, P., and Farnocchia, D. (2014). A study of dust and gas at mars from comet C/2013 A1 (siding spring). Astrophysical J Lett, 792(1):L16.

Kelley, M. S., Fernández, Y. R., Licandro, J., Lisse, C. M., Reach, W. T., A'Hearn, M. F., Bauer, J., Campins, H., Fitzsimmons, A., Groussin, O., et al. (2013). The persistent activity of jupiter-family comets at 3–7au. Icarus, 225(1):475–494.

Krasnopolsky, V. (2002). Mars' upper atmosphere and ionosphere at low, medium, and high solar activities: Implications for evolution of water. Journal of Geophysical Research: Planets, 107(E12):11–1–11–11.

Krasnopolsky, V. (2005). A sensitive search for SO2 in the martian atmosphere: Implications for seepage and origin of methane. Icarus, 178(2):487–492.

Krasnopolsky, V. (2006). Some problems related to the origin of methane on mars. Icarus, 180(2):359–367.

Krasnopolsky, V. (2012). Search for methane and upper limits to ethane and SO2 on mars. Icarus, 217(1):144–152.

Krasnopolsky, V., Bjoraker, G., Mumma, M., and Jennings, D. (1997). Highresolution spectroscopy of mars at 3.7 and 8 m: A sensitive search for H2O2, H2CO, HCl, and CH4, and detection of HDO. J Geophys Res Planets 1991 2012, 102(E3):6525–6534.

Krasnopolsky, V., Maillard, J., and Owen, T. (2004). Detection of methane in the martian atmosphere: evidence for life? Icarus, 172(2):537–547.

Kwon, Y., Ishiguro, M., Hanayama, H., Kuroda, D., Honda, S., Takahashi, J., Kim, Y., Lee, M., Choi, Y., Kim, M., Vaubaillon, J., Miyaji, T., Yanagisawa, K., Yoshida, M., Ohta, K., Kawai, N., Fukushima, H., and Watanabe, J.-i. (2015). Monitoring observations of the Jupiter-Family comet 17P/Holmes during 2014 perihelion passage. arXiv preprint.

Lallement, R., Bertaux, J., and Dalaudier, F. (1985). Interplanetary lyman-alpha spectral profiles and intensities for both repulsive and attractive solar force fields predicted absorption pattern by a hydrogen cell. Astronomy and Astrophysics, 150:21–32.

Langlais, B., Civet, F., and Thébault, E. (2017). In situ and remote characterization of the external field temporal variations at mars. Journal of Geophysical Research: Planets, 122(1):110–123.

Langlais, B., Purucker, M., and Mandea, M. (2004). Crustal magnetic field of mars. Journal of Geophysical Research: Planets, 109(E2).

Langowski, M., Sinnhuber, M., Aikin, A., von Savigny, C., and Burrows, J. (2014). Retrieval algorithm for densities of mesospheric and lower thermospheric metal atom and ion species from satellite-borne limb emission signals. Atmospheric Meas Techniques, 7(1):29–48.

Leblanc, F., Chaufray, J.-Y., Lilensten, J., Witasse, O., and Bertaux, J.-L. (2006). Martian dayglow as seen by the spicam uv spectrograph on mars express. Journal of Geophysical Research: Planets, 111(E9).

Lebonnois, S., Quémerais, E., Montmessin, F., Lefèvre, F., Perrier, S., Bertaux, J., and Forget, F. (2006). Vertical distribution of ozone on mars as measured by SPICAM/Mars express using stellar occultations. J Geophys Res Planets 1991 2012, 111(E9).

Lefèvre, F. and Forget, F. (2009). Observed variations of methane on mars unexplained by known atmospheric chemistry and physics. Nature, 460(7256):720–3.

León, J., Campins, H., Tsiganis, K., Morbidelli, A., and Licandro, J. (2010). Origin of the near-Earth asteroid phaethon and the geminids meteor shower. Astron Astrophys, 513:A26.

Levison, H. F. and Dones, L. (2014). Comet populations and cometary dynamics. In Encyclopedia of the Solar System (Third Edition), pages 705–719. Elsevier.

Levison, H. F. and Duncan, M. J. (1994). The long-term dynamical behavior of short-period comets. Icarus, 108(1):18–36.

Li, J., Samarasinha, N., Kelley, M., Farnham, T., Michael, A., Mutchler, M., Lisse, C., and Delamere, W. (2014). Constraining the dust coma properties of comet C/SIDING SPRING (2013 A1) at large heliocentric distances. Astrophysical J Lett, 797(1):L8.

Lillis, R. J., Fillingim, M. O., and Brain, D. A. (2011). Three-dimensional structure of the martian nightside ionosphere: Predicted rates of impact ionization from mars global surveyor magnetometer and electron reflectometer measurements of precipitating electrons. Journal of Geophysical Research: Space Physics, 116(A12).

Lo, D., Yelle, R., Schneider, N., Jain, S., Stewart, A., England, S., Deighan, J., Stiepen, A., Evans, J., Stevens, M., Chaffin, M., Crismani, M., William, M., Clarke, J., Holsclaw, G., Lefèvre, F., and Jakosky, B. (2015). Nonmigrating tides in the martian atmosphere as observed by MAVEN IUVS. Geophys Res Lett, 42(21):9057–9063.

Lunine, J. I. and Gautier, D. (2004). Coupled physical and chemical evolution of volatiles in the protoplanetary disk: A tale of three elements. Comets II, pages 105–113.

Lyytinen, E. and Jenniskens, P. (2003). Meteor outbursts from long-period comet dust trails. Icarus, 162(2):443–452.

M., C. and Jones, J. (2006). Annual variation of sporadic radar meteor rates. Mon Not R Astron Soc, 367(2):709–716.

M, R., Atreya, S., Webster, C., and Mahaffy, P. (2016). Cometary origin of atmospheric methane variations on mars unlikely. J Geophys Res Planets.

Ma, Y., Nagy, A., Sokolov, I., and Hansen, K. (2004). Threedimensional, multispecies, high spatial resolution MHD studies of the solar wind interaction with mars. J Geophys Res Space Phys 1978 2012, 109(A7).

Mahaffy, P. R., Benna, M., King, T., Harpold, D. N., Arvey, R., Barciniak, M., Bendt, M., Carrigan, D., Errigo, T., Holmes, V., et al. (2015). The neutral gas and ion mass spectrometer on the mars atmosphere and volatile evolution mission. Space Science Reviews, 195(1-4):49–73.

Maltagliati, L., Montmessin, F., Fedorova, A., Korablev, O., Forget, F., and Bertaux, J. (2011). Evidence of water vapor in excess of saturation in the atmosphere of mars. Science, 333(6051):1868–1871.

Maltagliati, L., Montmessin, F., Korablev, O., Fedorova, A., Forget, F., Määttänen, A., Lefèvre, F., and Bertaux, J. (2013). Annual survey of water vapor vertical distribution and water–aerosol coupling in the martian atmosphere observed by SPICAM/MEx solar occultations. Icarus, 223(2):942–962.

McClintock, W. E., Rottman, G. J., and Woods, T. N. (2005a). Solar-stellar irradiance comparison experiment II (SOLSTICE II): instrument concept and design. Solar Physics, 230(225-258).

McClintock, W. E., Schneider, N. M., Holsclaw, G. M., Clarke, J. T., Hoskins, A. C., Stewart, I., Montmessin, F., Yelle, R. V., and Deighan, J. (2015). The imaging ultraviolet spectrograph (iuvs) for the maven mission. Space Science Reviews, 195(1-4):75–124.

McClintock, W. E., Snow, M., and Woods, T. N. (2005b). Solar–Stellar Irradiance Comparison Experiment II (SOLSTICE II): Pre-Launch and On-Orbit Calibrations. Solar Physics, 230(1-2):259–294.

McNaught, R., Sato, H., and Williams, G. (2013). Comet C/2013 A1 (Siding Spring). Central Bureau Electronic Telegrams, 3368:1.

Medvedev, A., Nakagawa, H., Mockel, C., Yiğit, E., Kuroda, T., Hartogh, P., Terada, K., Terada, N., Seki, K., Schneider, N., Jain, S., Evans, J., Deighan, J., William, M., Lo, D., and Jakosky, B. (2016). Comparison of the martian thermospheric density and temperature from IUVS/MAVEN data and general circulation modeling. Geophys Res Lett, 43(7):3095–3104.

Medvedev, A. S., Francisco, G., Yiğit, E., Feofilov, A. G., Forget, F., and Hartogh, P. (2015). Cooling of the martian thermosphere by CO2 radiation and gravity waves: An intercomparison study with two general circulation models. J Geophys Res Planets, 120(5):913–927.

Mendillo, M., Narvaez, C., Matta, M., Vogt, M., Mahaffy, P., Benna, M., and Jakosky, B. (2015). MAVEN and the mars initial reference ionosphere model. Geophys Res Lett, 42(21):9080–9086.

Mendillo, M., Trovato, J., Narvaez, C., Mayyasi, M., Moore, L., Vogt, M. F., Fallows, K., Withers, P., and Martinis, C. (2016). Comparative aeronomy: Molecular ionospheres at earth and mars. J Geophys Res Space Phys.

Minschwaner, K., Herceg, D., Budzien, S., Dymond, K., Fortna, C., and RP, M. (2007). Observations of middle ultraviolet emissions in the middle and lower thermosphere: NO, o2, o, and mg+. J Geophys Res Space Phys 1978 2012, 112(A10):n/a–n/a.

Mocknatsche, D. (1938). Leningrad state univ. Annals, Astron. Series Issue, 4.

Molina-Cuberos, G., Witasse, O., Lebreton, J., Rodrigo, R., and J, L. J. (2003). Meteoric ions in the atmosphere of mars. Planet Space Sci, 51(3):239–249.

Montmessin, F., Bertaux, J., Quémerais, E., Korablev, O., Rannou, P., Forget, F., Perrier, S., Fussen, D., Lebonnois, S., Rébérac, A., and Dimarellis, E. (2006). Subvisible CO2 ice clouds detected in the mesosphere of mars. Icarus, 183(2):403–410.

Moores, J. and Schuerger, A. (2012). UV degradation of accreted organics on mars: IDP longevity, surface reservoir of organics, and relevance to the detection of methane in the atmosphere. J Geophys Res Planets 1991 2012, 117(E8).

Moores, J., Timothy, M., Ming, D., Archer, P., and Schuerger, A. (2014). The siding spring cometary encounter with mars: A natural experiment for the martian atmosphere? Geophys Res Lett, 41(12):4109–4117.

Moorhead, A. V., Wiegert, P. A., and Cooke, W. J. (2014). The meteoroid fluence at mars due to comet c/2013 a1 (Siding spring). Icarus, 231:13–21.

Morbidelli, A. (2006). Origin and dynamical evolution of comets and their reservoirs of water ammonia and methane. arXiv preprint astro-ph/0512256.

Morgenthaler, J. and Harris, W. (2007). Large aperture OI 6300 å observations of comet hyakutake: Implications for the photochemistry of OH and OI production in comet Hale-Bopp. The Astrophysical Journal, 657(2):1162.

Mueller-Wodarg, I., Strobel, D., Moses, J., Waite, J., Crovisier, J., Yelle, R., Bougher, S., and Roble, R. (2008). Neutral atmospheres. Space science reviews, 139(1-4):191–234.

Mumma, M., Villanueva, G., and Novak, R. (2009). Strong release of methane on mars in northern summer 2003. Science.

Murad, E. and Williams, I. P. (2002). Meteors in the Earth's Atmosphere: Meteoroids and Cosmic Dust and Their Interactions with the Earth's Upper Atmosphere. Cambridge University Press.

Nachbar, M., Duft, D., and Mangan, T. (2016). Laboratory measurements of heterogeneous CO2 ice nucleation on nanoparticles under conditions relevant to the martian mesosphere. Journal of Geophysical Research.

Nesvorný, D., Jenniskens, P., Levison, H., Bottke, W., Vokrouhlický, D., and Gounelle, M. (2010). Cometary origin of the zodiacal cloud and carbonaceous micrometeorites. implications for hot debris disks. Astrophysical J, 713(2):816.

Nesvorný, D., Vokrouhlický, D., Morbidelli, A., and Bottke, W. (2009). Asteroidal source of l chondrite meteorites. Icarus, 200(2):698–701.

Nesvorný, D., Vokrouhlický, D., Pokorný, P., and Janches, D. (2011). Dynamics of dust particles released from oort cloud comets and their contribution to radar meteors. Astrophysical J, 743(1):37.

Oort, J. H. et al. (1950). The structure of the cloud of comets surrounding the solar system and a hypothesis concerning its origin. Bulletin of the Astronomical Institutes of the Netherlands, 11:91.

Owen, T., Biemann, K., Rushneck, D., Biller, J., Howarth, D., and Lafleur, A. (1977). The composition of the atmosphere at the surface of mars. J Geophys Res, 82(28):4635–4639.

Pabari, J. and Bhalodi, P. (2017). Estimation of micrometeorites and satellite dust flux surrounding mars in the light of MAVEN results. Icarus.

Panale, F. P. and Salvail, J. R. (1984). An idealized short-period comet model: Surface insolation, h2o flux, dust flux, and mantle evolution. Icarus, 60(3):476–511.

Pandya, B. and Haider, S. (2012). Meteor impact perturbation in the lower ionosphere of mars: MGS observations. Planet Space Sci, 63:105–109.

Pandya, B. and Haider, S. (2014). Numerical simulation of the effects of meteoroid ablation and solar EUV/Xray radiation in the dayside ionosphere of mars: MGS/MEX observations. Journal of Geophysical Research: Space Physics, pages 9228–9245.

Pätzold, M., Häusler, B., Bird, M., Tellmann, S., Mattei, R., Asmar, S., Dehant, V., Eidel, W., Imamura, T., Simpson, R., and Tyler, G. (2007). The structure of venus' middle atmosphere and ionosphere. Nature, 450(7170):657–660.

Pätzold, M., Tellmann, S., and Häusler, B. (2009). A sporadic layer in the venus lower ionosphere of meteoric origin. Geophysical Research Letters.

Pätzold, M., Tellmann, S., Häusler, B., Hinson, D., Schaa, R., and Tyler, G. (2005). A sporadic third layer in the ionosphere of mars. Science, 310(5749):837–839.

Pesnell, W. and Grebowsky, J. (2000). Meteoric magnesium ions in the martian atmosphere. J Geophys Res Planets 1991 2012, 105(E1):1695–1707.

Peter, K., Pätzold, M., Gregorio, M., Witasse, O., F, G., Withers, P., Bird, M. K., Häusler, B., Hinson, D. P., Tellmann, S., and Tyler, L. G. (2014). The dayside ionospheres of mars and venus: Comparing a one-dimensional photochemical model with MaRS (Mars express) and VeRa (Venus express) observations. Icarus, 233:66–82.

Pham, L. and Karatekin, Ö. (2016). Scenarios of atmospheric mass evolution on mars influenced by asteroid and comet impacts since the late noachian. Planet Space Sci, 125:1–11.

Pham, L., Karatekin, Ö., and Dehant, V. (2009). Effects of meteorite impacts on the atmospheric evolution of mars. Astrobiology, 9(1):45–54.

Plane, J. (2004). A time-resolved model of the mesospheric na layer: constraints on the meteor input function. Atmos Chem Phys, 4(3):627–638.

Plane, J., Feng, W., and Dawkins, E. (2015). The mesosphere and metals: Chemistry and changes. Chemical reviews.

Plane, J., Gardner, C., Yu, J., She, C., Garcia, R., and Pumphrey, H. (1999). Mesospheric na layer at 40 n: Modeling and observations. J Geophys Res Atmospheres 1984 2012, 104(D3):3773–3788.

Plane, J., Murray, B., Chu, X., and Gardner, C. (2004). Removal of meteoric iron on polar mesospheric clouds. Sci New York N Y, 304(5669):426–8.

Plane, J. M. (2012). Cosmic dust in the earth's atmosphere. Chem Soc Rev, 41(19):6507–18.

Plane, J. M. and Whalley, C. L. (2012). A new model for magnesium chemistry in the upper atmosphere. J Phys Chem, 116(24):6240–52.

Press, W. H. (2007). Numerical recipes 3rd edition: The art of scientific computing. Cambridge university press.

Ralchenko, Y., Jou, F. C., Kelleher, D. E., Kramida, A., Musgrove, A., Reader, J., Wiese, W. L., and Olsen, K. J. (2005). Nist atomic spectra database (version 3.0). http://physics.nist. gov/asd3.

Rao, V. N., P, M., Jayaraman, A., and Rao, S. (2016). Some new aspects of the transient ionization layer of comet siding spring origin in the martian upper atmosphere. J Geophys Res Space Phys, 121(4):3592–3602.

Restano, M., Plaut, J., and Campbell (2015). Effects of the passage of comet c/2013 a1 (Siding spring) observed by the shallow radar (SHARAD) on mars reconnaissance orbiter. Geophysical Research Letters, 42(12):4663–4669.

Risberg, P. (1955). The spectrum of singly-ionized magnesium, mg-ii. Arkiv for Fysik, 9(5):483–494.

Rodriguez, J. A. P., Fairén, A. G., Tanaka, K. L., Zarroca, M., Linares, R., Platz, T., Komatsu, G., Miyamoto, H., Kargel, J. S., Yan, J., et al. (2016). Tsunami waves extensively resurfaced the shorelines of an early martian ocean. Scientific reports, 6:25106.

Roos-Serote, M., Atreya, S., Webster, C., and Mahaffy, P. (2016). Cometary origin of atmospheric methane variations on mars unlikely. Journal of Geophysical Research: Planets, 121(10):2108–2119.

Rottman, G., Woods, T., and George, V. (2014). Solar Radiation and Climate Experiment (sorce). Springer.

Rottman, G. J., Woods, T. N., and William, M. (2006). SORCE solar UV irradiance results. Adv Space Res-series, 37(2):201–208.

Rubin, M., Tenishev, V. M., Combi, M. R., Hansen, K. C., Gombosi, T. I., Altwegg, K., and Balsiger, H. (2011). Monte carlo modeling of neutral gas and dust in the coma of comet 1P/Halley. Icarus, 213(2):655–677.

Russo, N., Mumma, M., MA, D., and K, M. (2000). Water production and release in comet c/1995 o1 Hale–Bopp. Icarus.

Sagan, C. and Druyan, A. (1997). Comet. Random House Digital, Inc.

Sakai, S., Andersson, L., Cravens, T. E., Mitchell, D. L., Mazelle, C., Rahmati, A., Fowler, C. M., Bougher, S. W., Thiemann, E. M., Eparvier, F. G., Fontenla, J. M., Mahaffy, P. R., Connerney, J. E., and Jakosky, B. M. (2016). Electron energetics in the martian dayside ionosphere: Model comparisons with MAVEN data. J Geophys Res Space Phys, 121(7):7049–7066.

Salese, F., Di Achille, G., Neesemann, A., Ori, G. G., and Hauber, E. (2016). Hydrological and sedimentary analyses of well-preserved paleofluvial-paleolacustrine systems at moa valles, mars. Journal of Geophysical Research: Planets, 121(2):194–232.

Sandel, B. and Broadfoot, A. (1986). Statistical performance of the intensified charged coupled device. Appl Optics, 25(22):4135–4140.

Scharringhausen, M., Aikin, A., Burrows, J., and Sinnhuber, M. (2007a). First space-borne measurements of the altitude distribution of mesospheric magnesium species. Atmospheric Chemistry and Physics Discussions, 7(2):4597–4656.

Scharringhausen, M., Aikin, A., Burrows, J., and Sinnhuber, M. (2008). Global column density retrievals of mesospheric and thermospheric mg i and mg II from SCIAMACHY limb and nadir radiance data. J Geophys Res Atmospheres 1984 2012, 113(D13).

Scharringhausen, M., Winkler, H., Burrows, J. P., Sinnhuber, M., and Aikin, A. C. (2007b). Investigation of mesospheric and thermospheric emission signals from sciamachy limb and nadir measurements.

Schneider, N., Deighan, J., Jain, S., Stiepen, A., Stewart, A., Larson, D., Mitchell, D., Mazelle, C., Lee, C., Lillis, R., Evans, J., Brain, D., Stevens, M., W, M., Chaffin, M., Crismani, M., Holsclaw, G., Lefevre, F., Lo, D., Clarke, J., Montmessin, F., and Jakosky, B. (2015a). Discovery of diffuse aurora on mars. Sci New York N Y, 350(6261):aad0313.

Schneider, N., Deighan, J., Stewart, A., W., M., Jain, S., Chaffin, M., Stiepen, A., Crismani, M., Plane, J., J., C., Evans, J., Stevens, M., Yelle, R., Clarke, J., Holsclaw, G., Montmessin, F., and Jakosky, B. (2015b). MAVEN IUVS observations of the aftermath of the comet siding spring meteor shower on mars. Geophys Res Lett, 42(12):4755–4761.

Schuerger, A., Moores, J., Clausen, C., Barlow, N., and Britt, D. (2012). Methane from UVirradiated carbonaceous chondrites under simulated martian conditions. J Geophys Res Planets 1991 2012, 117(E8).

Selsis, F., Lemmon, M. T., Vaubaillon, J., and Bell, J. F. (2005). Extraterrestrial meteors: A martian meteor and its parent comet. Nature, 435(7042):581–581.

Sheel, V. and Haider, S. (2016). Longterm variability of dust optical depths on mars during MY24–MY32 and their impact on subtropical lower ionosphere: Climatology, modeling, and observations. J Geophys Res Space Phys, 121(8):8038–8054.

Silliman, B. and Kingsley, J. L. (1869). An account of the meteor which burst over weston in connecticut, in december, 1807, and of the falling of stones on that occasion. American Journal of Science, 1(139):1–8.

Smith, F. and Smith, C. (1972). Numerical evaluation of chapman's grazing incidence integral ch (X, ). J Geophys Res, 77(19):3592–3597.

Smith, M. (2002). The annual cycle of water vapor on mars as observed by the thermal emission spectrometer. J Geophys Res Planets 1991 2012, 107(E11):25–1–25–19.

Smith, P., Heise, C., and Esmond, J. (1995). Atomic spectral line database from cd-rom 23 of rl kurucz (smithsonian astrophysical observatory, cambridge, 1995).

Snow, M., Reberac, A., Quémerais, E., Clarke, J., McClintock, W., and Woods, T. (2013). A new catalog of ultraviolet stellar spectra for calibration. In Cross-Calibration of Far UV Spectra of Solar System Objects and the Heliosphere, pages 191–226. Springer.

Soret, L., Gérard, J., Libert, L., Shematovich, V. I., Bisikalo, D. V., Stiepen, A., and Bertaux, J. (2016). SPICAM observations and modeling of mars aurorae. Icarus, 264:398–406.

Spiga, A., F, G., M.Á., L., and Forget, F. (2012). Gravity waves, cold pockets and CO2 clouds in the martian mesosphere. Geophys Res Lett, 39(2):n/a–n/a.

Stevens, M. H., Evans, J., Schneider, N. M., Stewart, A. I. F., Deighan, J., Jain, S. K., Crismani, M., Stiepen, A., Chaffin, M. S., Mcclintock, W. E., et al. (2015). New observations of molecular nitrogen in the martian upper atmosphere by iuvs on maven. Geophysical Research Letters, 42(21):9050–9056.

Stevens, M. H., Gustin, J., Ajello, J. M., Evans, J. S., Meier, R., Kochenash, A. J., Stephan, A. W., Stewart, A. I. F., Esposito, L. W., McClintock, W. E., et al. (2011). The production of titan's ultraviolet nitrogen airglow. Journal of Geophysical Research: Space Physics, 116(A5).

Stevens, M. H., Siskind, D. E., Evans, J. S., Jain, S. K., Schneider, N. M., Deighan, J., Stewart, A. I. F., Crismani, M., Stiepen, A., Chaffin, M. S., et al. (2017). Martian mesospheric cloud observations by iuvs on maven: Thermal tides coupled to the upper atmosphere. Geophysical Research Letters.

Stevenson, R., Bauer, J., Cutri, R., Mainzer, A., and Masci, F. (2015). NEOWISE observations of comet C/2013 A1 (Siding Spring) as it approaches Mars. The Astrophysical Journal Letters, 798(2):L31.

Stokes, G., Yeomans, D., Bottke, W., Chesley, S., Evans, J., Gold, R., Harris, A., Jewitt, D., Kelso, T., McMillan, R., et al. (2003). Report of the near-earth object science definition team: a study to determine the feasibility of extending the search for near-earth objects to smaller limiting diameters. NASAOSS-Solar System Exploration Division.

Tenishev, V., Combi, M., and Davidsson, B. (2008). A global kinetic model for cometary comae: The evolution of the coma of the rosetta target comet Churyumov-Gerasimenko throughout the mission. The Astrophysical Journal, 685(1):659.

Thomas, E., Horányi, M., Janches, D., Munsat, T., Simolka, J., and Sternovsky, Z. (2016). Measurements of the ionization coefficient of simulated iron micrometeoroids. Geophys Res Lett, 43(8):3645–3652.

Treiman, A. and Treiman, J. (2000). Cometary dust streams at mars: Preliminary predictions from meteor streams at earth and from periodic comets. J Geophys Res Planets 1991 2012, 105(E10):24571–24581.

Tricarico, P. (2015). Highvelocity cometary dust enters the atmosphere of mars. Geophys Res Lett, 42(12):4752–4754.

Tricarico, P., Samarasinha, N., Sykes, M., Li, J., Farnham, T., Kelley, M., Farnocchia, D., Stevenson, R., Bauer, J., and Lock, R. (2014). Delivery of dust grains from comet c/2013 a1 (Siding spring) to mars. The Astrophysical Journal Letters.

Vaubaillon, J., Maquet, L., and Soja, R. (2014). Meteor hurricane at mars on 2014 october 19 from comet c/2013 a1. Monthly Notices of the Royal Astronomical Society, 439(4):3294–3299.

Vogt, M. F., Withers, P., Fallows, K., Andersson, L., Girazian, Z., Mahaffy, P. R., Benna, M., Elrod, M. K., Connerney, J. E., Espley, J. R., Eparvier, F. G., and Jakosky, B. M. (2016). MAVEN observations of dayside peak electron densities in the ionosphere of mars. J Geophys Res Space Phys.

Vondrak, T., Plane, J., Broadley, S., and Janches, D. (2008). A chemical model of meteoric ablation. Atmospheric Chemistry and Physics Discussions, 8(23):7015–7031.

Wang, Y.-C., Luhmann, J. G., Rahmati, A., Leblanc, F., Johnson, R. E., Cravens, T. E., and Ip, W.-H. (2016). Cometary sputtering of the martian atmosphere during the siding spring encounter. Icarus, 272:301–308.

Webster, C., Mahaffy, P., Atreya, S., Flesch, G., Farley, K., and Team, S. (2013). Low upper limit to methane abundance on mars. Science, 342(6156):355–357.

Webster, C. R., Mahaffy, P. R., Atreya, S. K., Flesch, G. J., Mischna, M. A., Meslin, P.-Y., Farley, K. A., Conrad, P. G., Christensen, L. E., Pavlov, A. A., et al. (2015). Mars methane detection and variability at gale crater. Science, 347(6220):415–417.

Weissman, P. R. (1983). The mass of the oort cloud. Astronomy and Astrophysics, 118:90–94.

Wetherill, G. (1967). Collisions in the asteroid belt. J Geophys Res, 72(9):2429–2444.

Whalley, C. and Plane, J. (2010). Meteoric ion layers in the martian atmosphere. Faraday Discuss, 147(0):349–368.

Whipple, F. L. (1950). A comet model. i. the acceleration of comet encke. The Astrophysical Journal, 111:375–394.

Wiegert, P., Vaubaillon, J., and Margaret, C. (2009). A dynamical model of the sporadic meteoroid complex. Icarus, 201(1):295–310.

William, J. and Murad, E. (2002). Models of meteoric metals in the atmosphere. Meteors in the Earth's Atmosphere: Meteoroids and Cosmic Dust and Their Interactions with the Earth's Upper Atmosphere, page 265.

Witasse, O., Nouvel, J., Lebreton, J., and Kofman, W. (2001). HF radio wave attenuation due to a meteoric layer in the atmosphere of mars. Geophys Res Lett, 28(15):3039–3042.

Withers, P. (2009). A review of observed variability in the dayside ionosphere of mars. Adv Space Res-series, 44(3):277–307.

Withers, P. (2014). Predictions of the effects of mars's encounter with comet c/2013 a1 (Siding spring) upon metal species in its ionosphere. Geophys Res Lett, 41(19):6635–6643.

Withers, P., Christou, A., and Vaubaillon, J. (2013). Meteoric ion layers in the ionospheres of venus and mars: Early observations and consideration of the role of meteor showers. Adv Space Res-series, 52(7):1207–1216.

Withers, P., Fallows, K., Girazian, Z., Matta, M., Häusler, B., Hinson, D., Tyler, L., Morgan, D., Pätzold, M., Peter, K., et al. (2012). A clear view of the multifaceted dayside ionosphere of mars. Geophysical Research Letters, 39(18).

Withers, P., Matta, M., Lester, M., Andrews, D., Edberg, N., Nilsson, H., Opgenoorth, H., Curry, S., Lillis, R., Dubinin, E., et al. (2016). The morphology of the topside ionosphere of mars under different solar wind conditions: Results of a multi-instrument observing campaign by mars express in 2010. Planetary and Space Science, 120:24–34.

Withers, P., Mendillo, M., Hinson, D., and Cahoy, K. (2008). Physical characteristics and occurrence rates of meteoric plasma layers detected in the martian ionosphere by the mars global surveyor radio science experiment. Journal of Geophysical Research, 113(A12).

Wong, A., Atreya, S., and Encrenaz, T. (2003). Chemical markers of possible hot spots on mars. J Geophys Res Planets 1991 2012, 108(E4).

Wordsworth, R. and Pierrehumbert, R. (2014). Abiotic oxygen-dominated atmospheres on terrestrial habitable zone planets. The Astrophysical Journal Letters.

Ye, Q. and Hui, M. (2014). An early look of comet C/2013 A1 (siding spring): Breathtaker or nightmare? The Astrophysical Journal, 787(2):115.

Yelle, R., Mahieux, A., Morrison, S., Vuitton, V., and Hörst, S. (2014). Perturbation of the mars atmosphere by the near-collision with comet c/2013 a1 (Siding spring). Icarus, 237:202–210.

Youngmin, J. and Malhotra, R. (2015). The current impact flux on mars and its seasonal variation. Icarus, 262:140–153.

Zurek, R., Tolson, R., Baird, D., Johnson, M., and Bougher, S. (2015). Application of MAVEN accelerometer and attitude control data to mars atmospheric characterization. Space Sci Rev, 195(1-4):303–317.